System-oriented Analysis of the Dynamic Behaviour of Direct Methanol Fuel Cells

Systemorientierte Analyse der
Dynamik der Direktmethanol-Brennstoffzelle

Dissertation
zur Erlangung des akademischen Grades

Doktoringenieurin
(Dr.-Ing.)

von Dipl.-Ing. Ulrike Krewer
geb. am 21. April 1976 in Bitburg

genehmigt durch die Fakultät für Verfahrens- und Systemtechnik
der Otto-von-Guericke-Universität Magdeburg

Gutachter: Prof. Dr.-Ing. Kai Sundmacher
Prof. Dr. Mihai Christov

Promotionskolloquium am 25.11.2005

Preface

This dissertation thesis presents the major results of my research work performed between 2001 and 2005 at the Max Planck Institute (MPI) for Dynamics of Complex Technical Systems in Magdeburg, Germany.

I would like to thank Prof. Dr.-Ing. habil. Kai Sundmacher for giving me the opportunity to carry out this research at the Max Planck Institute. I am also particularly grateful to him for showing me his systematic approach of analysing and modelling physical and chemical systems.
My thanks also goes to Prof. Dr. Mihai Christov from the University of Chemical Technology and Metallurgy, Sofia, Bulgaria, for giving me in-sight into the complex chemical and electrochemical processes occurring on electrode surfaces, as well as for the always interesting cultural exchange.

During the four years of research at the Max Planck Institute, I had assistance from the following students:
Dipl.-Ing. Dimas Fernandez Menendez, M.Sc. Ashish Kamat, Christian Borchert, M. Sc. Lakshmi Dhevi-Baskar, Dipl.-Ing. Dejan Naydenov. It was a pleasure to work with them.

I would like to thank Christian Fuchs who in the last months of this thesis unremittingly assembled and conducted experiments with me on the 100 cm^2 DMFCs. My gratitude also goes to Detlef Franz and Reiner Könning of the mechanical and electrical workshop, respectively, for their commitment and help, as well as to Gerry Truschkewitz from the IT group who developed the basic video processing procedure.

Furthermore, I would like to thank Dr.-Ing. Thorsten Schultz, who developed the miniplant and set up the fuel cell laboratory with me, Dipl.-Ing. Torsten Schroeder for his assistance on CAD, Dipl.-Ing. Matthias Pfafferodt for the contribution of some CFD simulations, and Dr.-Ing. Tanja Vidakovic for discussions about methanol oxidation and experimental impedance spectra. I also appreciate to all other colleagues for a lot of interesting and helpful discussions, and for the brilliant atmosphere they established at the institute.

My thankfulness goes to my partner and my family.

Magdeburg, 30.09.2005

Contents

List of Symbols

Latin symbols

A	system matrix
a_i	ratio of volume flow rate entering CSTR in series i per volumetric flow rate leaving the previous distributor CSTR (parallel channel and rhomboidal design flow field)
a_{ij}	ratio of volumetric flow rate entering CSTR ij per volumetric flow rate leaving the previous CSTR $(i-1)j$ (spot design flow field)
A_s	geometric electrode area, m^2
b_1, b_2	coefficients for the Laplace transformed methanol flux
B	input matrix
c_{CH_3OH}	methanol concentration, mol/m^3
$c_{Pt}, (c_{Ru})$	surface concentration of Pt (of Ru), mol/m^2
$c_{max,Pt}$	number of COx adsorption sites on Pt, = 0.11 mol CO $/m^2$
$c^{A,ij}_{CH_3OH}$	methanol concentration inside the CSTR ij, (anode spot design flow field model), mol/m^3
$c^{A,sensor}_{CH_3OH}$	methanol concentration at UV-Vis sensor, mol/m^3
$c^{pipe,in}$, $(c^{pipe,out})$	concentration entering (leaving) the pipe, mol/m^3
$c^{ref}_{CH_3OH}$	reference methanol concentration, = 1000 mol/m^3
$c^{M}_{H^+}$	proton concentration in membrane pores, = 1200 mol/m^3 [68]
C	output matrix
C^{AC}	anode double layer capacitance, C/m^2
$C^{AC}_{CH_3OH}$	methanol concentration in Laplace domain
C^{CC}	cathode double layer capacitance, = 907 C/m^2 (own CV measurements)
d^{AC}	thickness of anode catalyst layer, = 35×10^{-6} m [57]
d^{AD}	thickness of anode diffusion layer, = 1.7×10^{-4} m [57]
d^{M}	thickness of (fully hydrated) Nafion^{TM} 105 membrane, = 10^{-4} m [57]
D	direct transmission matrix

D_{ew}	diffusion coefficient of eosin in water at room temperature, = 5.34×10^{-10} m^2/s (calc. see text)
$D_{\mathrm{CH_3OH}}$	diffusion coefficient of methanol in water at 333 K, = 3.187×10^{-9} m^2/s, (calc. acc. [54], p.600)
$D^M_{\mathrm{CH_3OH}}$	diffusion coefficient of methanol in membrane at 333 K, = 4.7×10^{-10} m^2/s (own measurements)
$D^M_{H^+}$	diffusion coefficient of protons in membrane, = 4.5×10^{-9} m^2/s [12]
E	anode potential, V
f	frequency, Hz
F	Faraday constant, = 96485 C/mol
$F(t), F(\theta)$	cumulative residence time [-]
$F^{A,in}$	volumetric flow rate entering the anode compartment, m^3/s
$F^{A,COLi}, F^{A,DISi}$	anode volume flow rate leaving collector or distributor CSTR i, m^3/s
F^{PFTRi}	volumetric flow rate entering PFTR i
F_1,F_2	transcendental parts of the membrane transfer function
$F_{1,rat}$,$F_{2,rat}$	rational forms of F_1 and F_2
$g_{\mathrm{CO}}, (g_{\mathrm{OH}})$	inhomogeneity/interaction factor for Frumkin/Temkin adsorption on Pt, (on Ru)
G	transfer function
h	counter
i	counter
i_{cell}	cell current density, A/m^2
i_{max}	maximum initial cell current density for overshooting behaviour, A/m^2
I	current variable in Laplace domain
$Im(Z)$	imaginary part of Z
j	imaginary unit
j	counter
k	constant in transfer function
$k_{i,0}$	anode reaction rate constant for reaction $i \in \{1, 2, -2, 3\}$
k_i^{eff}	effective anode reaction rate function for reaction $i \in \{1, 2, -2, 3\}$
k^{AD}	effective mass transport coefficient in anode diffusion layer, = $D_{\mathrm{CH_3OH}}(\epsilon^{AD})^{1.5}/d^{AD}$, m/s
k_ϕ	electrokinetic permeability of membrane, = 1.13×10^{-19} m^2 [12]
$k_{\phi 2}$	electro-osmotic parameter, = 1.33×10^{-3} m^3/C (see text)
l_{tube}	length of anode compartment inlet or outlet pipe, m
m	number of time-relevant singularities
n	number of poles and zeros

$n_{\mathrm{CH_3OH}}$	flux density of methanol, mol/m^2/s
$N_{\mathrm{CH_3OH}}$	variable of methanol flow in Laplace domain
P_i	pole i of a transfer function
Pe_{ss}	Peclet number for membrane, $k_{\phi 2} d^M i_{cell} / D^M_{\mathrm{CH_3OH}}$
Pe_{ax}	axial Peclet number in anode pipes, $v \cdot l_{tube} / D_{ew}$
Pe_{rad}	radial Peclet number in anode pipes, $v \cdot 2r_{tube} / D_{ew}$
r	radial variable for anode pipes, m
$r_{Ai}, (r_{Ai0})$	reaction rate (constant) for anode reaction step i
$r_C, (r_{C0})$	cathodic reaction rate (constant), mol/m^2/s
r_{tube}	radius of anode compartment inlet or outlet pipe, m
res	residue
R	universal gas constant, = 8.314 J/mol/K
R_{el}	Ohmic resistance of the membrane, $= d^M / \kappa^M$, Ω m^2
Re	Reynolds number
$Re(Z)$	Real part of Z
s	Laplace variable
t	time, s
T	cell temperature, = 333 K
$u, (U)$	input variable (in Laplace domain)
U_0^θ	standard cell voltage, 1.213 V (thermodynamic calc.)
U_{cell}	cell voltage, V
v	mean velocity in outlet or inlet tube, $F^{A,in} / (\pi r^2_{tube})$
v_i	velocity in outlet or inlet tube PFTR ring i
V^A	volume of a CSTR in the active region of the anode compartment, m^3
V^{AC}	volume of anode catalyst layer, $= A_s \cdot d^{AC}$, m^3
V^{DIS}, V^{COL}	volume of a CSTR in the distributor (collector area) of the anode compartment, m^3
V^{PFTRi}	volume of PFTR i, m^3
w^{AC}	anode (and cathode) catalyst loading, = 5 mg/cm^2
$x, (X)$	state variable (in Laplace domain)
$y, (Y)$	output variable (in Laplace domain)
z	spatial coordinate in membrane, m
Z_i	zero i of a transfer function
Z	electrochemical impedance, Ω

Greek symbols

α_{Ai}	charge transfer coefficient for anodic reaction i
α_C	charge transfer coefficient for cathodic reaction, = 0.5
$\beta_{\mathrm{CO}}, (\beta_{\mathrm{OH}})$	symmetry parameter for Frumkin/Temkin adsorption on Pt (Ru), =0.5
ϵ^{AC}	porosity of anode catalyst layer, = 0.81 [57]
ϵ^{AD}	porosity of anode diffusion layer, = 0.71 [57]
ϕ	electrostatic potential, V
κ^M	ionic conductivity of membrane, = 0.0873 1/Ω/m (calc. acc. [66])
μ	pore fluid viscosity in membrane, = 4.823 kg/m/s (calc. acc. [54], p.441,445)
θ_{CO}	surface coverage of Pt with $\mathrm{CO_{ads}}$
θ_{OH}	surface coverage of Ru with $\mathrm{OH_{ads}}$
$\theta^{ref}_{\mathrm{CO}x}$	reference COx surface coverage of active sites of Pt catalyst, = 0.5
$\theta_{\mathrm{CO}x}$	COx surface coverage of active sites of Pt catalyst
θ_{CO}	CO surface coverage of active sites of Pt catalyst
θ_{OH}	OH surface coverage of active sites of Ru catalyst
ρ	radius in complex plane
τ	mean residence time, s

Subscripts

A	anode
AC	anode catalyst layer
ACO	anode $\mathrm{CO_{ads}}$ surface coverage on Pt
AE	anode potential
AOH	anode $\mathrm{OH_{ads}}$ surface coverage on Ru
AT	anode CO_x surface coverage on Pt
C	cathode
$\mathrm{CH_3OH}$	methanol
$\mathrm{CO}x$	adsorbed intermediates occurring during methanol oxidation, e.g. CO, COH, CHO
i	counter
M	membrane
num	numerically evaluated
rel	relative
ss	at steady state conditions prior to current step
tot	total

Superscripts

A	anode compartment
A, in	entering the anode compartment
AC	anode catalyst layer
AD	anode diffusion layer
CC	cathode catalyst layer
COL	collector of anode flow field
$CSTR$	CSTR in active area
DIS	distributor of anode flow field
ij	counter for CSTRs and modules: i=row, j=column
M	membrane
$M, A/(M, C)$	boundary membrane-anode /(membrane-cathode)
$\ominus$	reference state

Abbreviations

CAD	computer aided design software
CFC	cyclone flow cell
CFD	computational fluid dynamics
CSTR	continuous stirred tank reactor
DMFC	Direct Methanol Fuel Cell
EIS	Electrochemical Impedance Spectroscopy
l.h.s.	left hand side
MEA	membrane electrode assembly
OCV	open circuit voltage
ODE	ordinary differential equations
pcd-DMFC	DMFC with anodic parallel channel design flow field
PDE	partial differential equations
PEM	polymer electrolyte membrane
PFTR	plug flow tubular reactor
rd-DMFC	DMFC with anodic rhomboidal design flow field
r.d.s.	rate determining step
r.h.s.	right hand side
RTD	residence time distribution
sd-DMFC	DMFC with anodic spot design flow field
SHE	standard hydrogen electrode
VCS	reaction mechanism presented in [71] named after the authors T. Vidakovic, M. Christov and K. Sundmacher

Kurzzusammenfassung

Die vorliegende Arbeit analysiert experimentell und modelltheoretisch das dynamische Betriebsverhalten der Direktmethanol-Brennstoffzelle (DMFC). Fokus ist hierbei der Einfluss einer Änderung der Zellstromstärke auf die Zellspannung. In einem ersten Schritt wurde das Verhalten der DMFC auf Stromsprünge systematisch experimentell untersucht. Die Anwendung der linearen Systemanalyse führte zu einem Kriterium, das Mindestbedingungen für die Reproduktion des gemessenen dynamischen Spannungsverhaltens setzt. Modelle unterschiedlicher Komplexität demonstrierten den Einfluss verschiedener physikalisch-chemischer Vorgänge auf das dynamische Verhalten der DMFC und führten zu einer Kategorisierung bzgl. ihres Einflusses auf die Dynamik der Zellspannung.
Als bestimmende Einflussgröße zeigte sich die Kinetik der anodischen Methanoloxidation. Deren Dynamik wurde experimentell und theoretisch mittels elektrochemischer Impedanzspektroskopie charakterisiert. Eine Modelldiskriminierung ermöglichte die Identifizierung einer Kinetik, die quantitativ sowohl die anodische Methanoloxidation als auch, nach Integrierung in ein DMFC-Modell, die dynamische Zellspannung bei Stromsprüngen reproduzieren kann.
Aufgrund höherer Systemwirkungsgrade wird die DMFC bei niedrigen Volumenströmen gefahren. Diese bewirken eine designspezifische Konzentrationsverteilung von Methanol über die Anodenverteilerstruktur. In dieser Arbeit wurden beispielhaft drei verschiedene Verteilerstrukturen bzgl. ihrer hydrodynamischen Eigenschaften untersucht und mit Netzwerken idealer Reaktoren modelliert. DMFC-Modelle mit diesen Netzwerken sowie experimentelle Ergebnisse zeigten einen über ein weites Konzentrationsspektrum vernachlässigbaren Einfluss der örtlichen Konzentrationsverteilung auf die Dynamik der DMFC. Weitere experimentelle und modelltheoretische Untersuchungen konnten den Einfluss verschiedener Systemparameter auf die Dynamik der DMFC charakterisieren. Die Experimente wiesen jedoch zusätzlich einen signifikanten Einfluss von gasförmigem Kohlendioxid auf, der durch die Modelle nicht wiedergegeben werden kann.
Die vorgestellten Modelle sind stark reduzierte Modelle, die für den mittleren Leistungsbereich von DMFCs gelten. Sie weisen sehr kurze Rechenzeiten auf und stellen daher eine mögliche Basis für die Entwicklung von Regelungsstrategien dar.

Chapter 1

Introduction

1.1 Fuel Cells: Past, Present and Future Perspective

Fuel cells have been known for more than 150 years. Their working principle was discovered by Sir William Grove in 1839. He connected two different gases on the one hand electronically via a metal, and on the other hand ionically via an electrolyte. The occurring reactions produced a flux of electrons from one gas compartment to the other - hence, electricity. In further studies, various electrochemical systems like H_2/O_2 and H_2/Cl_2 as well as different electrolytes were investigated, but the efficiency of fuel cells could not be increased to a level of technical usability. Just 27 years later, Werner von Siemens discovered the dynamo-electric principle, with which he was able to convert rotational energy into electrical energy. This process posed a more efficient way of generating electric energy than fuel cells, and therfore fuel cells took a back seat within the following decades.
Approximately a century later, the combination of the dynamo-electric and combustion engine principle had become omnipresent, producing the power needed in everyday life. The technique proved to be simple, and, in contrast to fuel cells, worked even with basic materials like steel. Nonetheless, its heavy weight, mechanical wear due to moving parts, and a low (theoretical) efficiency still pose important drawbacks. While weight and moving parts make its usage for space and mobile technology unattractive, low efficiencies have been motivating the search for alternative, more energy efficient power generation technologies for everyday life, which do not need three energy conversion steps to transform chemical energy into electrical energy:

chemical energy → thermal energy → mechanical energy → electric energy

Each of these steps, especially the second one, which generates a high percentage of unusable thermal energy (Carnot efficiency), decreases significantly the theo-

retically achievable system efficiency. The three drawbacks mentioned above are non-existent in fuel cells: they can be constructed light weight, without moving parts, and convert chemical energy directly into electric energy with much higher theoretical efficiencies. These features have made fuel cells attractive again, and combined with advancements in application and development of new materials (e.g. gas diffusion electrodes, solid electrolytes), this leads to increasingly promising results. Some of the first applications were in spacecrafts, where the advantages of fuel cell technology were system requirements: In the Gemini earth-orbit space program, a polymer electrolyte membrane fuel cell was used. A solid electrolyte, the polymer electrolyte membrane, separated the reactants hydrogen and oxygen. Due to long term stability problems, it was replaced in the Apollo spacecraft with 75% KOH as electrolyte - an alkaline fuel cell.
In the following decades, further advancement in materials and system engineering increased efficiencies of fuel cells, and since the 1990s, the usage of fuel cells for mobile, stationary and portable applications has been announced and increasingly researched. The motivation was not the application of fuel cells as energy source for expensive specialty applications like spacecrafts, but rather the global problems of predicted future energy shortage and of global warming (Kyoto protocol [1]) - hence, the introduction of more energy efficient technologies for generating electricity. As for mobile and stationary applications, it was thought that due to the fuel cells' higher efficiency, it would be relatively easy to enter the market and dominate more than a lucrative niche held by the combustion engine beforehand. While substantial improvements in fuel cell development have been achieved since the time of Grove and of the Gemini spacecraft, the combustion engine sector has also seen efficient refinements like combined heat and power plants or recently hybrid vehicles. Furthermore, a new technology brings different system requirements which have to fit in system environments shaped by the established technology. For such reasons, substituting existing technology with fuel cells has been difficult and all predicted dates of market entrance have thus been repeatedly postponed. This is especially true for mobile applications like cars, where manufacturers withdrew their expectations of a breakthrough within the next years.

Fuel cells for stationary as well as mobile applications offer the advantage of higher energy efficiency, but up to now, they have not shown direct advantages for users, except for energy generation in isolated locations. The situation changes when fuel cells are used for portable applications. Here, batteries dominate the market. They are either rechargeable (secondary batteries) or one-way (primary batteries). In most energy-intensive electronic consumer goods, rechargeable batteries with lithium or lead as reactants are applied. They are expensive with respect to

[1] United Nations Framework Convention on Climate Change, http://unfccc.int/resource/docs/convkp/kpeng.html

the amount of energy stored, they are heavy and permit only few working hours before recharge or replacement. In contrast to such closed systems, fuel cells show significant advantages. They occupy a similar volume, but enable longer working hours. In addition, their storage tank can be refilled during operation. Example applications are mobile phones, and laptops (prototypes presented by Toshiba, Samsung, and other major electronic companies), remote energy supply systems for street works (SFC), and even military equipment for mobile soldiers (Giner Electrochemical Systems).

Most types of fuel cells are not suitable for portable applications due to high operating temperatures (solid oxide fuel cells, molten carbonate fuel cells, phosphoric acid fuel cells) or high reactant purity requirements (alkaline fuel cells). Furthermore, portable fuel cells should be small, produce power in the low Watt range ($\ll 1000$ W) and should start-up fast. So far, only fuel cells using a polymer electrolyte membrane can fulfill these requirements.
This fuel cell type can be used with different fuels, e.g. gaseous hydrogen, hydrazene, methanol, and methylether. Of these, hydrogen and methanol are more promising and show a reasonable application potential. Although, in contrast to methanol, the chemical conversion of hydrogen shows higher system efficiencies and is neutral with respect to CO_2 production, storage problems for hydrogen (low storage densities, high weight of storages) are a major drawback. A potential combination of methanol storage and on-board reforming to hydrogen solves this problem. Nonetheless, in portable and dynamic applications, such on-board conversion of a liquid fuel into hydrogen is difficult due to the coupling of the reforming step with fuel cell operation. In addition, reformers significantly increase the weight as well as the volume of such systems.
The alternative is the direct use of methanol as reactant for fuel cells. These so called direct methanol fuel cells (DMFC) are used for most portable fuel cell system prototypes presented by companies. In contrast to hydrogen, methanol not only has the advantage of easier storage and higher energy density due to its liquid state; also, leakage problems play a minor role due to the higher viscosity of liquids. The realisation of a storage tank exchange or refill with liquids is technically easier and saver than with gases. Besides these advantages, DMFCs show lower performances due to kinetic and material problems. These current problems as well as the working principle of DMFCs are discussed in the following section.

1.2 Working Principle

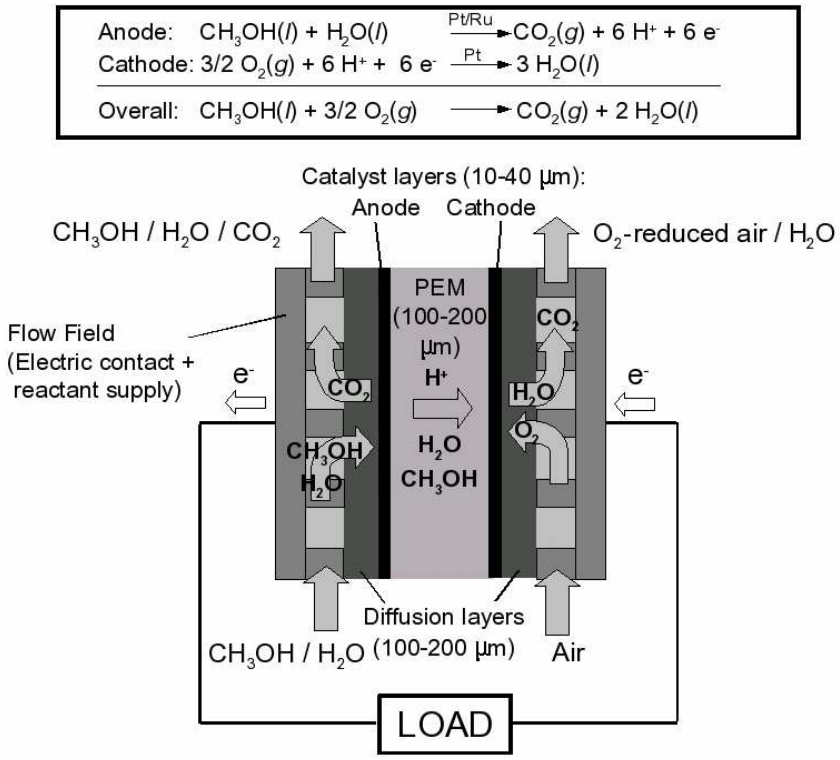

Figure 1.1: Working principle of the direct methanol fuel cell (DMFC)

DMFCs consist of a membrane-electrode assembly (MEA), in which conversion of chemical energy into electric energy as well as proton transport takes place, and of further elements for the distribution and the transport of electrons, reactants and products. This is illustrated in Fig. 1.1. The membrane-electrode assembly features

- an anode, where methanol is oxidised with water to carbon dioxide, protons and electrons (see chemical equation in Fig. 1.1),
- an electrically isolating, but proton conducting membrane (PEM)
- a cathode, where protons react with oxygen and electrons to water (see chemical equation in Fig. 1.1).

The electron transfer from anode to cathode is realised with an external wire which leads the electron flux via an electric load, hence powering it. On the anode and the cathode side, the reactants are transported to the membrane electrode assembly via flow fields. These are optimised to yield a homogeneous reactant

concentration distribution over the electrode area (see also chapter 4), subsequently also referred to as active area. The anode feed flow usually consists of a 0.5 - 3 molar methanol/water solution with a temperature range of 290 - 400 K. The cathode feed flow is either pure oxygen, or - more common and more technically relevant - air at ambient temperature. Direct contact between the convective flow inside a flow field and the respective electrode would abrade the usually small catalyst particles (diameter $\approx$ 5-10 nm), damaging the electrode. To prevent this, porous diffusion layers are sandwiched in between anode flow field and anode, and between cathode flow field and cathode, respectively. The diffusion layers also enable transport of reactants to the parts of the active area which otherwise would be excluded from reactants due to direct contact between electrode and flow field material.
While the protons are transported through the proton conducting membrane, the electron transfer between electrode area and external wires is realised via the electroconductive diffusion layers, flow fields, and current collector plates. Due to negligible electric resistance, the flow fields show the same potential as the respective electrodes, and are therefore called monopolar plates.

Despite the advantages of DMFCs, they show a significant drawback: Lower efficiencies than for hydrogen fuel cells. Main causes are the slow anodic methanol oxidation and the methanol transport from the anode to the cathode, the so called methanol crossover.
In contrast to the fast oxidation of hydrogen, the total oxidation of methanol to carbon dioxide is slow and can only proceed via a set of complex reaction steps. At least one of these steps involves a strongly adsorbed intermediate which slows down the total reaction rate (details see chapter 3). Up to now the most active catalyst is Pt/Ru, which makes it the most frequently used catalyst. Pt/Ru may be either a combination of Pt and Ru particles, or an alloy of both.
The second cause for the lower efficiency of DMFCs is the permeability of the membrane to methanol: Methanol is transported through the membrane to the cathode. At the cathode catalyst, usually Pt, it reacts to carbon dioxide, electrons and protons. The parallel occurrence of electrooxidation (methanol oxidation) and electroreduction (oxygen reduction) at the cathode induces a mixed cathode potential, which is lower than the pure oxygen reduction potential. As a result, the overall cell voltage and the DMFC efficiency is lower.

1.3 Motivation and Scope of this Work

In the last decade, extensive research has been carried out to improve the steady-state DMFC performance. However, the processes occurring inside a DMFC and their interaction, especially at dynamic operation, are barely understood. As mentioned in section 1.1, the dynamic behaviour of DMFCs is of relevance for portable equipment (system start-up, system shut-down and switching between different load states). There have been only a few research works in this field.
The objective of this work is to systematically analyse DMFC responses to dynamic changes in cell current density. Special emphasis has been placed on modelling and understanding the physical and chemical processes and their interaction, which dominate at dynamic operation.

This thesis is structured into four main parts:

- Analysis of the phenomena governing the dynamic behaviour of DMFCs (chapter 2)
- Characterisation of the dynamic behaviour of methanol oxidation (chapter 3)
- Hydrodynamic characterisation of anode flow fields (chapter 4)
- Final analysis of the dynamic DMFC behaviour including flow field influences (chapter 5)

Chapter 2 presents an in-depth analysis of the principle phenomena occurring inside DMFCs at dynamic operation. Applying current steps on the DMFC, the cell voltage shows overshooting, i.e. its transitory value exceeds its steady state value. This phenomenon is shown to be the main characteristic of the cell voltage response to current steps. A general overshoot criterion, based on linear system theory, is presented. Its application to DMFC models of different complexity, i.e. to models covering different physico-chemical phenomena, enables a qualitative prediction of cell voltage overshoots. The impact of the single processes, especially the dominance of the methanol oxidation reaction mechanism, on the transient cell voltage response is highlighted.
Chapter 3 presents the identification of a lumped reaction kinetic description which is able to qualitatively and quantitatively describe the dynamic and steady-state behaviour of the anodic methanol oxidation. The implementation of this reaction kinetics into the DMFC model presented in chapter 2 yields a quantitative prediction of the experimentally observed dynamic DMFC behaviour. Various reaction kinetic descriptions were formulated and discriminated using linear system analysis and validation on experimentally recorded electrochemical impedance spectra.

For low to medium volumetric flow rates, the distribution of methanol over the active area should influence the steady-state and dynamic performance of DMFCs. In chapter 4, three flow field designs were hydrodynamically characterised by residence time and concentration distribution measurements. Reduced models consisting of ideal reactor networks are shown to suitably describe the hydrodynamic behaviour of the flow fields.
Chapter 5 presents an in-depth analysis of the dynamic behaviour of DMFCs and the influence of methanol concentration and current density on the cell voltage response. The flow field designs of chapter 4 are experimentally analysed with regard to their influence on the DMFC performance. For modelling these experiments, the hydrodynamic models of chapter 4 are combined with the DMFC model containing the identified anode reaction kinetics (chapter 3). The results highlight the strong influence of the processes at the anode catalyst layer on the overall DMFC behaviour.

Chapter 2

Phenomena Governing the Dynamic DMFC Behaviour

2.1 Introduction

Investigating the dynamics of fuel cells has been a minor topic in fuel cell research for many years. Most of the research is focussed on improving the steady-state behaviour, long-term stability and costs. As motivated in the introduction, characterising and understanding the dynamic behaviour of the DMFC is of particular interest: Possible applications are mainly in the portable devices sector where load dynamics are essential. For analysing and understanding the processes inside the DMFC at dynamic behaviour, physico-chemical models and reliable experiments for model validation are required.
A variety of models for different fuel cell types exists in the literature, however, most of them are steady state models. Dynamic models have been published e.g. by Heidebrecht et al. [31] (MCFC), Ceraolo et al. [13] (PEMFC), Sundmacher et al. [68] (DMFC), and Yerramalla et al. [77] (PEMFC).
Only few groups investigated the dynamics of the DMFC. Besides empirical dynamic DMFC models, e.g. [67], the dynamic behaviour of DMFCs to concentration changes [56, 57, 68, 78] was investigated. Zhou et al. [78] were among the first to apply system theoretical approaches on fuel cell models, and in particular on a DMFC model. They showed that the non-minimal-phase behaviour, which was observed in a concentration step experiment, can be predicted via analysis of the transfer function of a respective linearised model. Linear system analysis has many advantages: Analytical analysis of models can be conducted which may yield a thorough understanding of the influence of the underlying physico-chemical phenomena. Furthermore, transfer functions can be used as a basis for controller design.

Analysis of experimental DMFC responses to dynamic changes of the cell current has been conducted in [4, 5, 39, 67]. In the two latter publications, the authors performed various cell current steps and waited for a few seconds until performing the next step. They also conducted gradual cell loading and unloading from or to the open circuit voltage (OCV), i.e. the voltage obtained when the electric circuit is open (no-load condition). In addition, they combined cell current steps and gradual loading and unloading to driving cycles. Such measurements proved useful for empirical one-step-ahead prediction models of DMFC stacks [67]. Nonetheless, these experiments are not optimal for the analysis of processes occurring inside the fuel cell. As an example, the observation time after a current step is mostly only 30 s. This time-span is sufficient for the above mentioned one-step-ahead models, but it is not sufficient for reaching a steady state for all dynamic variables.

This chapter and chapter 4 present a systematic approach towards recording and analysing the DMFC voltage responses to load steps between various steady states. While this chapter gives an analysis of the nature of the detected cell voltage response at constant methanol concentration in the anode compartment, chapter 5 gives an in-depth analysis of the underlying phenomena and shows the influence of methanol concentration distribution inside flow fields on the dynamic response.
In this chapter, the operating conditions are chosen so that a constant methanol concentration along the whole active area is expected in the anode compartment. First, a polarisation curve is recorded, and the characteristic operating regimes (e.g. pseudo-Ohmic regime) are identified (section 2.2.3). This is followed by various current steps between the regimes. A subsequent analysis shows the characteristic influence of the operating regimes on the cell response.
Dynamic DMFC models are presented in section 2.3 where cell voltage responses are analysed using linear system analysis. The development of a general overshoot criterion assists in predicting model parameter conditions for reproducing the experimentally observed overshooting behaviour. Additionally, the influence of electrochemical reactions, methanol crossover and double layer charging are investigated.
The presented models hold for analysis of an operating regime in which mass transport influences are minimised: low anode compartment residence time (i.e. negligible methanol concentration distribution), low current densities (i.e. negligible CO_2 bubble influence). This allows an in-depth analysis of the processes occuring inside the MEA.

2.2 Experiments

2.2.1 Applied DMFC Design and Materials

The experiments were carried out using a single DMFC fed with air and liquid methanol/water solutions [57]. The identical anode and cathode monopolar plates are made from graphite material (thickness 7 mm, material code FU4369) supplied by Schunk Kohlenstofftechnik (Germany). The necessary flow field structures for the reactant distribution over the MEA surface are millcut into the plates. They consist of parallel channels of 2 mm width and 2 mm depth, with 1 mm wide ribs between them. A distributor and collector channel connect the parallel channels to the inlet and outlet ports, respectively. The media (air and methanol/water solution) are supplied in one corner of the rectangular flow field and leave at the opposite corner. The flow field itself has the outer dimensions 65 x 40 mm, identical to the catalyst layer on the MEAs, which leads to an active area of A_s=26 cm^2.
As diffusion layer PTFE-coated TORAY carbon paper (TGP-H-060) is used, with a PTFE loading between 20 and 25 mass-% with respect to the uncoated material. Finally, the membrane electrode assemblies (MEA) are prepared from NAFION^{TM} N-105 membrane foil, onto which the catalyst layers are applied using an airbrush technique developed by ZSW Ulm (Germany) [24]. The anode catalyst layer features a catalyst loading of 5 mg/cm^2 (unsupported) platinum ruthenium black (Alfa Aesar Johnson Matthey HiSPEC^{TM} 6000) and a NAFION^{TM} content of 15 mass-% relative to the metal loading (i.e. 0.75 mg/cm^2). The cathode catalyst layer has the same metal loading, but as catalyst (unsupported) pure platinum black is used (Alfa Aesar Johnson Matthey HiSPEC^{TM} 1000) and the NAFION^{TM} content is 10 mass-% relative to the metal loading (i.e. 0.5 mg/cm^2).
The DMFC is completed by gold-plated current collectors and stainless steel plates for bracing the whole sandwich structure. A torque of 5 N m is exerted on the screws, which hold together the steel back plates. After assembly, each DMFC is conditioned and evaluated by operation with pure humidified hydrogen and air for three times 8 hours, before it is operated on methanol solutions.

2.2.2 DMFC Miniplant

For full-scale testing of DMFCs, a miniplant was designed by Schultz [57], which is uses a process control system (PC-S7/WinCC by Siemens) to enable automatic testing procedures, with a special focus on dynamic operation. Fig. 2.1 shows a simplified flowsheet of the miniplant.

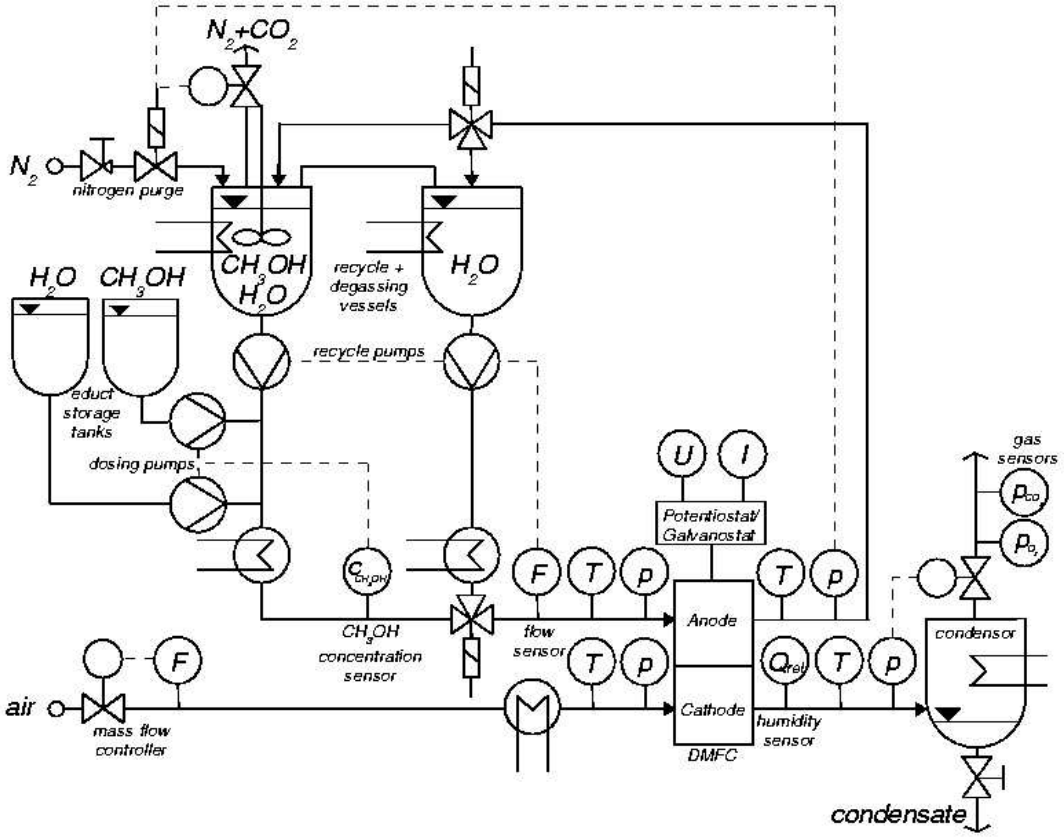

Figure 2.1: Simplified flow scheme of DMFC miniplant with all important sensors and actuators.

The DMFC cathode is supplied with dry air (dew point $\approx$ 271 K) at flow rates between 0.4 and 5.0 m^3/h normal (mass flow controller F101, type Mass6020 by Buerkert AG, Germany) at cathode outlet pressures of ambient up to 0.5 MPa. The air is pre-heated in a plate heat exchanger (W101), air temperatures and pressures are measured at the cathode inlet and outlet. At the cathode outlet, also the relative humidity of the air is measured (Q202, type HygroClip IE by rotronic AG, Switzerland). Finally the cathode exhaust air enters a condensor, where it is dried to reach a dew point below 263 K (condensate is collected). The dry air is sent into a fume hood, while its oxygen and carbon dioxide contents are measured. The oxygen sensor (Q204) is a paramagnetic sensor (PAROX 1000 H by MBE AG, Switzerland), while carbon dioxide is measured using an IR-sensor (Q203, type OEM-NDIR EGC-5% by Pewatron AG, Switzerland).

On the DMFC anode side, a liquid recycle loop is installed. It consists of two alternative cycles, one for methanol/water solution and one for pure water. Both branches of the anode cycle feature vessels for pressure equilibration and carbon

dioxide removal (B1 and B2), gear pumps (P401 and P402) and heat exchangers (W403 and W406). Flow rates between 10^{-6} and 5×10^{-3} m^3/min can be achieved. Automatic valves (V403/V404 and V408/V409) enable a flexible and practically immediate change between methanol/water solution and pure water anode feed without causing significant disturbances in liquid flow rate and pressure. The flow rate is measured by a Coriolis-type sensor (F401, type MASS 2100 DI6 by Danfoss, Denmark). Like on the cathode side, the medium temperature and pressure are measured at the cell inlet and outlet. The methanol concentration of the anode inlet medium is measured online using an ultrasound sensor (Q401, type LiquiSonic30 by SensoTech GmbH, Germany), based on the influence of methanol concentration on the speed of sound in methanol/water solutions. This sensor is used in a methanol concentration controller, which uses two dosing pumps for pure methanol (P351) and pure water (P301) (mzr-2905 by HNP Mikrosysteme, Germany) as actuators. Methanol concentrations between zero and 1.5 mol/l can be detected and controlled. The flow rates of the dosing pumps can be controlled in the range from 0.2 up to 18 ml/min. To adjust the anode pressure and also to strip off carbon dioxide, the recycle vessels are equipped with a nitrogen purge/blanket. The anode pressure can be controlled in the range between ambient and 0.5 MPa absolute. The liquid inlet temperature (which is also the DMFC temperature due to the applied high flow rates) can be controlled in the range between 253 K and 423 K. The DMFC is electrically connected to a potentiostat (HP60-50 by Wenking GmbH, Germany), which enables operation of fuel cells from below 1 W up to 1 kW at a maximum of 50 A. Galvanostatic as well as potentiostatic operation is possible, with the option to automatically run user-defined load scenarios.
The array of sensors around the DMFC enables full online material balancing of all key components (oxygen, methanol, water, carbon dioxide). The tolerances of the sensor values are listed and discussed in detail in [57].

2.2.3 Experimental Results

First, a steady state polarisation curve was recorded with the following operating conditions:

- Anode
  feed temperature: 333 K (equals whole DMFC temperature)
  methanol feed concentration: 1 mol/l
  flow rate: 0.5 $\times 10^{-3}$ m^3/min
  pressure: 0.17 MPa

- Cathode
  feed temperature: 293 K
  feed composition: dry air (dew point approx. 271 K)

flow rate: 0.5 m^3/h normal
pressure: 0.17 MPa

As can be seen in Fig. 2.2, the open circuit voltage (OCV) lies around 0.6 V, and the limiting current density is approximately 2000 A/m^2. The fairly low OCV can be attributed to the crossover of methanol as well as to the deviation of the anodic open circuit potential from the standard reversible potential of methanol oxidation (see discussion of Fig. 2.3). It is in accordance with literature data (0.65 V in [68], 0.55-0.7 V in [66]).
At temperatures up to 333 K, it is known that methanol chemisorption only occurs on Pt and water adsorption on Ru, respectively. This mechanism changes when going to higher temperatures. Then, methanol is also oxidised on Ru (see [20]). In addition, methanol oxidation accelerates with higher temperatures. Since the aim of this thesis is the development and investigation of dynamic DMFC models, defined conditions and reaction mechanisms for modeling are mandatory for obtaining reasonable results. Hence, an operating temperature of 333 K was chosen. The relatively low performance of the presented DMFC mainly results from this moderate operating temperature.

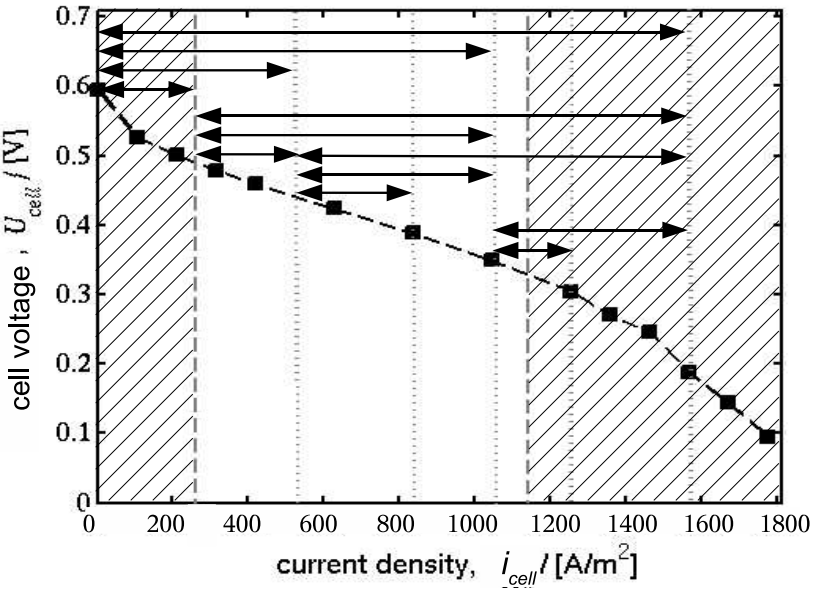

Figure 2.2: Recorded polarisation curve with illustration of conducted current steps (arrows) and the activation-dominated regime (hatched area, left), pseudo-Ohmic regime (middle) and transport-controlled regime (hatched area, right).

In the polarisation curve (Fig. 2.2), the activation-controlled and mass-transport controlled regimes are marked by hatching. In between, without hatching, is the

pseudo-Ohmic regime. When investigating cell responses to current steps, the initial current as well as the final current should strongly influence the voltage response. Hence, a series of current steps between the different regimes were performed. These steps are visualised by arrows in Fig. 2.2. In Figs. 2.3-2.5, voltage responses to the different current steps are presented. Each of the current densities was maintained for 10 minutes before being set again to the previous current density level. Hence, the processes in the DMFC are allowed for reaching a steady state before the next current change is applied (in-depth evaluation given in section 5.2.1). Voltage responses of systems which are not in a steady state prior to the current step do not have defined conditions, and interpretation and modelling would be difficult.

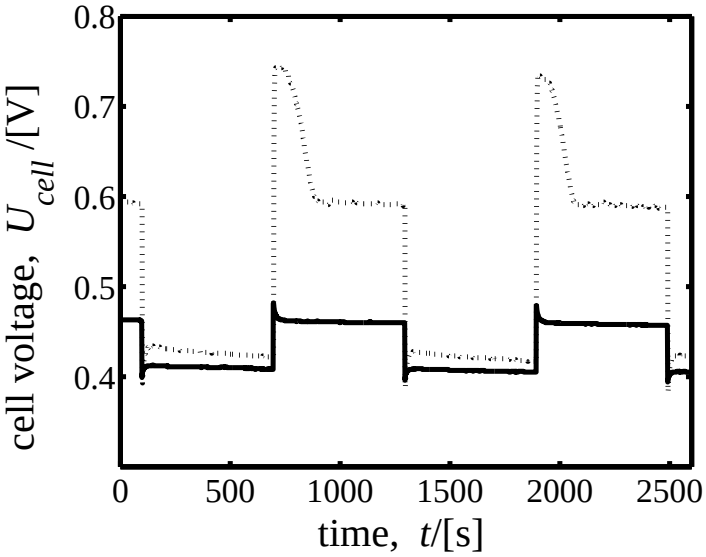

Figure 2.3: Cell voltage as a function of time for current steps from the lower pseudo-Ohmic regime: Current steps between 0 and 520 A/m^2 (dotted), steps between 260 and 520 A/m^2 (solid).

Fig. 2.3 displays voltage responses to current steps below 520 A/m^2. The solid line shows cell voltage responses to current density steps between 520 A/m^2 and 260 A/m^2. The voltage response is quite symmetrical, showing instantaneous relative overshoots of approximately 40% whenever the current is switched between the levels, i.e. the absolute value of the voltage change directly after the current step exceeds the absolute steady state voltage difference by 40%. The steady state is reached after a certain relaxation time. In contrast to this, voltage responses to current density steps between 0 A/m^2, i.e. OCV, and 520 A/m^2 are non-symmetrical. The voltage response at OCV, i.e. when the current is switched off, shows an overshoot of approximately 80% and a relaxation time of up to 250 seconds, in comparison to roughly 30 seconds in the formerly discussed current

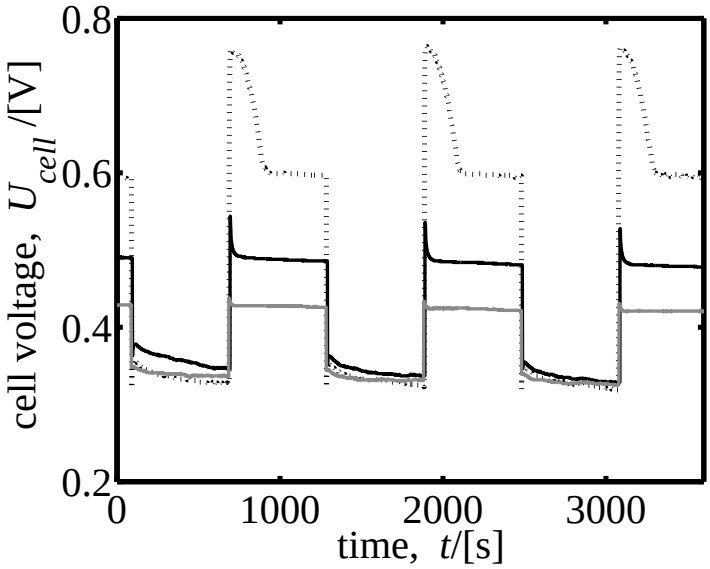

Figure 2.4: Cell voltage as a function of time for current steps from the upper pseudo-Ohmic regime: Current steps between 0 and 1050 A/m^2 (dotted), steps between 260 and 1050 A/m^2 (black), steps between 520 and 1050 A/m^2 (grey).

steps. Additionally, the shape of the OCV voltage response shows S-shape rather than exponential behaviour as in the former step. At a final current density of 260 A/m^2 the activation-controlled regime is reached (see Fig. 2.2) and the forward reaction, i.e. the oxidation of methanol, takes place. The situation changes at OCV. There, the overall anode and cathode reactions are inhibited immediately, and a steady state different from that at closed circuit establishes. The respective processes at the anode are complex and have been barely investigated. Since at open circuit the sum of all anode reaction currents equals zero, the following scenario may take place: Several molecules, e.g. unstable methanol intermediates or ruthenium oxides, are further oxidised, while in parallel some reversible oxidation reactions, e.g. water chemisorption (see chapter 3), may be reversed. Thus, a change in the anode reactions that govern the potential could explain the difference between the open circuit voltage response and the cell voltage response at closed circuit. Due to these reactions, the anodic open circuit potential at steady state should also deviate from the thermodynamic, i.e. reversible, methanol oxidation potential. Interplays of reaction steps at open circuit potential as the one proposed above have been investigated for cathode processes [14]. There, the authors presented an in-depth analysis of the interaction between oxygen and organic substances.

Similar effects as the ones discussed in Fig. 2.3 can be observed for steps at higher current density levels, see Figs. 2.4 and 2.5. Steps to OCV result in higher

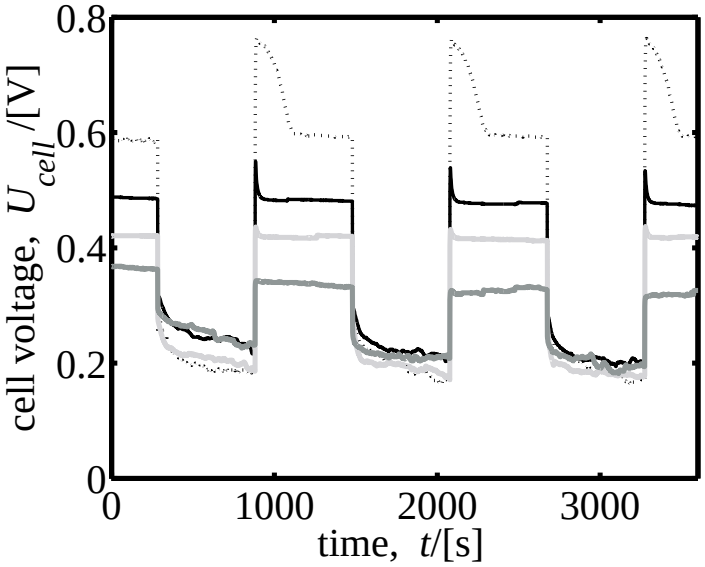

Figure 2.5: Cell voltage as a function of time for current steps from the mass-transport controlled regime: Current steps between 0 and 1570 A/m^2 (dotted), steps between 260 and 1570 A/m^2 (black, solid), steps between 520 and 1570 A/m^2 (light grey), steps between 1050 and 1570 A/m^2 (dark grey).

overshooting and longer relaxation times. Voltage responses to a current step-up to high current densities show small fluctuations, in contrast to Fig. 2.3. Furthermore, the voltage is overshooting and decays subsequently to new quasi-steady state levels, which may be as low as the overshoot voltages obtained directly after the current step. Decay and fluctuation should be assigned to mass transport effects. While the upper current density in Fig. 2.4 is 1050 A/m^2, which is close to the mass transport dominated regime, the upper current density in Fig. 2.5 is well within this region. This difference leads to the following: The voltage response to the current step-up in Fig. 2.4 is decaying to a steady state cell voltage near the overshoot cell voltage due to mass transport limitation effects, whereas Fig. 2.5 shows intense fluctuations of the voltage signal, attributed to the onset of intense CO_2 bubble formation. Furthermore, it can be observed that the system takes in the order of minutes to reach a new steady state, if at all in the given time interval. Apart from these effects, when stepping down to lower currents, Fig. 2.4 as well as Fig. 2.5 show smooth voltage responses with exponential shapes after the overshoots. This behaviour is comparable to the current density steps from 520 A/m^2 to 260 A/m^2 in Fig. 2.3.

Fig. 2.6 plots the absolute overshoots of cell voltage responses vs. the initial and final cell current density for the conducted current steps. Only stable voltage signals are evaluated. As can be seen, increasing final cell current density correlates with decreasing absolute overshoot. An already mentioned reason for this kind

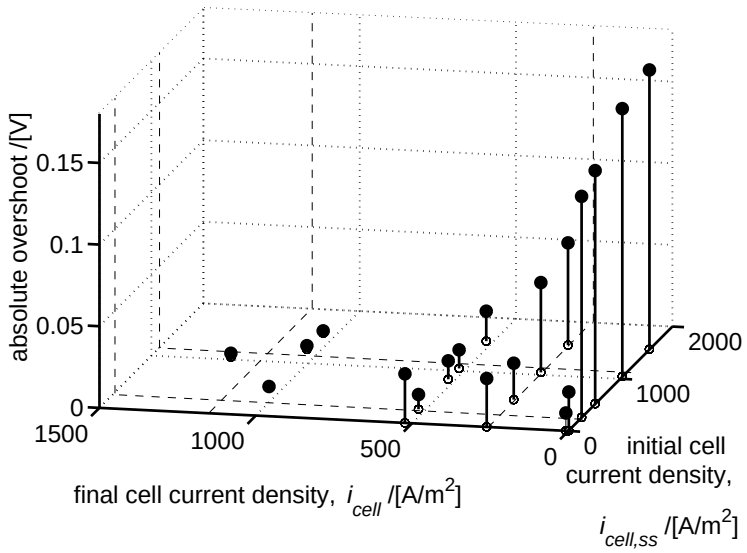

Figure 2.6: Voltage response to cell current steps: Absolute overshoot vs. initial and final cell current density (only stable voltage signals were evaluated, dashed lines separate the regimes in the polarisation curve, compare with Fig. 2.2)

of behaviour is the decay of the cell voltage to a lower steady state voltage after an overshoot, which can be attributed to mass transport phenomena.
Furthermore, except for current density steps from 0 A/m^2 to higher current densities, higher initial cell current densities result in higher overshoots (for constant final cell current density). This leads to the following effect: The final steady state cell voltage is mostly independent from the initial cell current density. Hence, the cell voltage, the methanol concentration on anode and cathode side, and the methanol crossover should reach the same steady state after a current step to the same final cell current density. In contrast to this, the initial conditions vary strongly. Directly after the current step, the cell voltage is strongly influenced by the initial steady state and methanol crossover. Methanol crossover will be lower with increasing initial cell current density. This may cause lower cathode overpotentials, and as a result a higher cell voltage, when switching to the same final cell current density from higher initial cell current densities.
Since the methanol crossover is proportional to the cathode side CO_2 production, there is a dependence of the cathodic CO_2 concentration on the current density. Schultz et al. [57, 58] have shown this effect in steady state measurements and simulations. Due to online detection of CO_2 at the cathode outlet (after the condensor, see Fig. 2.1), the experimental setup enables dynamic recording of the CO_2 concentration.
Fig. 2.7 presents the CO_2 content in the cathode exhaust air as a function of time for current steps between 260 and 1050 A/m^2. Although the response can not

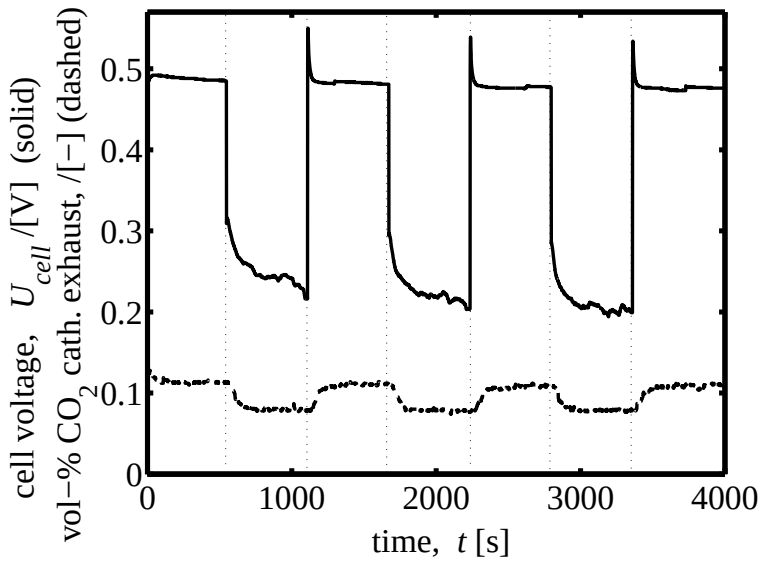

Figure 2.7: Cell voltage (solid) and CO_2 content in cathode exhaust air (dashed) as a function of time for current steps between 260 and 1050 A/m^2

be quantitatively interpreted due to the residence time influence of the fixtures (pipes, condensor), Fig. 2.7 shows qualitatively the response of methanol crossover to the current steps: After a delay time of $\sim$ 30 seconds, the CO_2 concentration gradually moves to a higher steady state when stepping down to 260 A/m^2, or to a lower steady state when stepping up to 1050 A/m^2. The results are explained as follows: A higher current density causes higher anodic methanol conversion. This lowers the methanol concentration in the anode catalyst layer, and as a result the diffusive methanol crossover and the cathodic CO_2 production are reduced. The opposite holds for a decrease in current density.

2.3 System Theoretical Analysis

2.3.1 Set of Governing Equations

To describe and analyse the behaviour of the DMFC with respect to dynamic changes in current density, a non-linear mathematical model was developed accounting for the following phenomena (see Fig. 2.8):

- Diffusive mass transport through the anode diffusion layer
- Electrochemical oxidation of methanol in the anode catalyst layer
- Formation of an adsorbed intermediate COx during electrochemical methanol oxidation

- Electrochemical reduction of oxygen in the cathode catalyst layer
- Methanol crossover, i.e. undesired transfer of methanol through the PEM by diffusion and electroosmosis
- Undesired electrochemical oxidation of methanol at the cathode catalyst layer

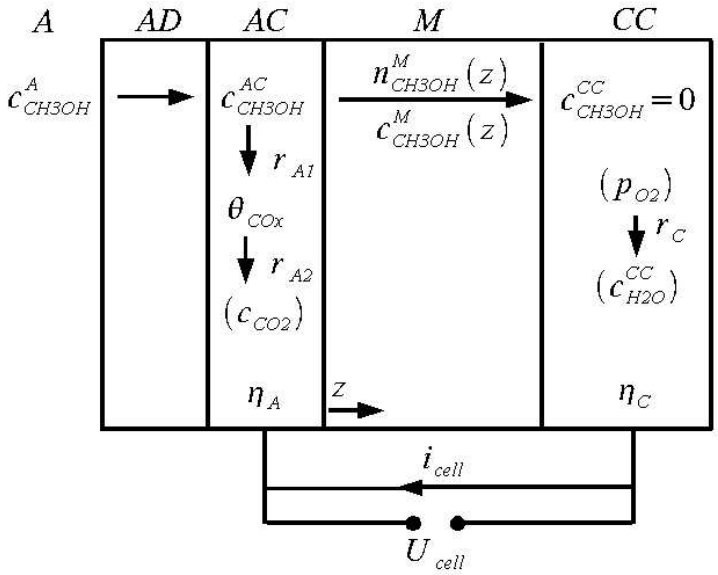

Figure 2.8: Illustration of the DMFC model including reactants and physicochemical phenomena. A: anode compartment; AD: anode diffusion layer; AC: anode catalyst layer; M: membrane; CC: cathode catalyst layer.

The following model assumptions were made:

- Residence time in the anode compartment is very low, so that the compartment effectively is a differential reactor. Therefore, the concentration in the compartment is assumed to be equal to the inlet concentration.
- Ohmic drops in current collectors and electric connections are negligible.
- The fuel cell is operated isothermally.
- Oxygen is fed in excess, i.e. oxygen conversion in the cathode compartment is negligible, and therefore no oxygen mass balance is required.
- Oxygen and carbon dioxide do not diffuse into the PEM.
- Water concentration in the anode compartment is assumed to be constant (excess component in a liquid mixture).

- Mass transport resistances in the catalyst layers are negligible due to the fact that these are thin (35 μm) in comparison to the diffusion layer (170 μm) and the PEM (100 μm).
- Mass transport in the diffusion layers is a quasi-steady state.
- On the anode side, a pure liquid phase mixture is assumed, i.e. gas-phase formation by release of carbon dioxide bubbles is not taken into account. Problems with bubble formation only get visible when working and modelling in or near the transport-controlled regime of the polarisation curve, which is not done here.
- Methanol which is transported to the cathode is assumed to instantaneously react with oxygen at the cathode, i.e. its concentration in the cathode catalyst layer is zero.
- Experiments were carried out with zero pressure difference between anode and cathode compartment, hence no pressure-driven transport through the membrane takes place.
- In the modelled scenarios, all electrochemical reactions are far from equilibrium. Hence, Tafel type rate expressions can be applied.
- Due to the postulated instantaneous dissolution of carbon dioxide after production and due to the applied Tafel kinetics, no carbon dioxide balance is formulated.
- A two step reaction mechanism is used to describe the electrochemical oxidation of methanol at the platinum-ruthenium catalyst. The mechanism is a lumped approach and accounts for the oxidation of a Pt-adsorbed intermediate COx (e.g. CO):

$$\mathrm{CH_3OH + Pt} \rightarrow \mathrm{Pt - COx + 4H^+ + 4}e^- \tag{2.1}$$

$$\mathrm{Pt - COx + H_2O} \overset{\mathrm{Ru}}{\rightarrow} \mathrm{CO_2 + 2H^+ + 2}e^- \mathrm{+ Pt} \tag{2.2}$$

There is intense discussion about the real methanol oxidation mechanism and the intermediates involved, see section 3.1. Focus of this chapter is not on determining or validating a specific reaction mechanism. Instead the fact is used that methanol oxidation is known to occur via a carbon intermediate which is adsorbed on active Pt surface sites and which tends to block the sites. As this intermediate may be CO, COH, CHO or other postulated and measured species, the lumped intermediate COx is introduced. While the first reaction step is the reaction of methanol to the intermediate, the second reaction is the oxidation of this intermediate and a parallel reaction, which is the adsorption of water on Ru.

This adsorption step on Ru is known to be fast compared to the slow methanol oxidation [25], and therefore it is assumed to be in equilibrium. A dynamic influence of water chemisorption on the cell voltage response is not accounted for in this chapter (in-depth investigation given in chapter 3).
As can be seen from the assumptions, the model is limited to an operating regime of very high anode flow rates and to the activation controlled and pseudo-Ohmic regions of the polarisation curve. Under these conditions, an analysis of the dynamic processes occuring inside the MEA can be conducted with minimal influence of mass transport.
Based on the assumptions given above, balance equations for methanol concentration in the catalyst layer (eq. 2.3), COx surface coverage (eq. 2.4), methanol concentration in the membrane (eq. 2.6), anode overpotential (eq. 2.5) and cathode overpotential (eq. 2.7), as well as reaction rates (eqs. 2.8 - 2.10) were formulated:

$$\frac{dc^{AC}_{\mathrm{CH_3OH}}}{dt} = \frac{k^{AD}A_S}{V^{AC}}(c^{A}_{\mathrm{CH_3OH}} - c^{AC}_{\mathrm{CH_3OH}}) - \frac{A_S}{V^{AC}}n^{M,A}_{\mathrm{CH_3OH}} - \frac{A_S}{V^{AC}}r_{A1} \tag{2.3}$$

$$\frac{d\theta_{\mathrm{CO}x}}{dt} = \frac{1}{c_{max,Pt}}(r_{A1} - r_{A2}) \tag{2.4}$$

$$\frac{d\eta_A}{dt} = \frac{1}{C^{AC}}i_{cell} + \frac{1}{C^{AC}}(-4Fr_{A1} - 2Fr_{A2}) \tag{2.5}$$

$$\frac{\partial c^{M}_{\mathrm{CH_3OH}}}{\partial t} = -\frac{\partial n^{M}_{\mathrm{CH_3OH}}}{\partial z} \tag{2.6}$$

$$\frac{d\eta_C}{dt} = -\frac{1}{C^{CC}}i_{cell} - \frac{1}{C^{CC}}\ 6Fr_C - \frac{1}{C^{CC}}\ 6Fn^{M,C}_{\mathrm{CH_3OH}} \tag{2.7}$$

$$r_{A1} = r_{A10}\frac{c^{AC}_{\mathrm{CH_3OH}}}{c^{ref}_{\mathrm{CH_3OH}}}\frac{1-\theta_{\mathrm{CO}x}}{1-\theta^{ref}_{\mathrm{CO}x}}exp\left[\frac{\alpha_{A1}F}{RT}\eta_A\right] \tag{2.8}$$

$$r_{A2} = r_{A20}\frac{\theta_{\mathrm{CO}x}}{\theta^{ref}_{\mathrm{CO}x}}exp\left[\frac{\alpha_{A2}F}{RT}\eta_A\right] \tag{2.9}$$

$$r_C = -r_{C0}\ exp\left[\frac{-(1-\alpha_C)F}{RT}\eta_C\right] \tag{2.10}$$

$$n^{M}_{\mathrm{CH_3OH}} = -D^{M}_{\mathrm{CH_3OH}}\frac{\partial c^{M}_{\mathrm{CH_3OH}}}{\partial z} + c^{M}_{\mathrm{CH_3OH}}k_{\phi 2}i_{cell} \tag{2.11}$$

$$U_{cell} = U^{\theta}_0 - \eta_A + \eta_C - \frac{d^M}{\kappa^M}i_{cell} \tag{2.12}$$

Transport of methanol through the membrane is described by eq. 2.11, consisting of a Fickian diffusion term (first term on r.h.s.), and an electroosmotic term (second term) with the lumped electroosmotic parameter $k_{\phi 2}$. The latter is derived by using the isobaric convective flow velocity equation given by Schloegl [55]:

$$n^{M}_{\mathrm{CH_3OH},convective} = -c^{M}_{\mathrm{CH_3OH}}\frac{k_\phi}{\mu}c^{M}_{H^+}F\frac{d\phi}{dz} \tag{2.13}$$

Here, k_ϕ is the electrokinetic permeability of the membrane calculated according [12], μ the pore fluid viscosity in the membrane calculated according [54], and $c^M_{H^+}$ the proton concentration in the membrane pores [68]. Analogous to Sundmacher et al. in [68], the electrostatic potential gradient $d\phi/dz$ can be formulated in terms of the cell current density i_{cell}, using the Nernst-Planck equation for proton transport:

$$\frac{d\phi}{dz} = -\frac{i_{cell}}{c^M_{H^+}F^2(D^M_{H^+}/RT + c^M_{H^+}k_\phi/\mu)} \tag{2.14}$$

which is inserted into eq. 2.13. From this, a lumped electroosmotic parameter $k_{\phi 2}$ is obtained:

$$k_{\phi 2} = \frac{k_\phi}{\mu F(D^M_{H^+}/RT + c^M_{H^+}k_\phi/\mu)} \tag{2.15}$$

The overall cell voltage U_{cell}, eq. 2.12, is a function of the standard open-circuit cell voltage U^θ_0, the overpotentials at anode and cathode, η_A and η_C, respectively, and the Ohmic loss in the PEM, $R_{el} = d^M/\kappa^M$. The overpotentials are defined with respect to the standard electrode potentials.

2.3.2 Linear System Analysis and Overshooting

The approach chosen here is a combination of standard methods used in process dynamics [11] and control engineering [50]. The procedure is as follows:
After linearisation at the initial steady state, the given set of balance equations (eqs. 2.3-2.7) can be cast into the following standardised state space form:

$$\frac{d\mathbf{x}}{dt} = A\mathbf{x}(t) + Bu(t) \tag{2.16}$$

$$y(t) = C\mathbf{x}(t) + Du(t) \tag{2.17}$$

where A, B, C and D are the system matrix, input matrix, output matrix and direct transmission matrix, respectively.
The input variable $u(t)$ is the deflection of the current density from its initial steady state value,

$$u(t) = i_{cell}(t) - i_{cell,ss}, \tag{2.18}$$

and the output variable $y(t)$ is the deviation of the cell voltage from its initial steady state value,

$$y(t) = U_{cell}(t) - U_{cell,ss}. \tag{2.19}$$

The index ss always refers to the steady state prior to the current step. $\mathbf{x}(t)$ is the vector of state variables, that is the deviation of the system variables from their initial steady state values:

$$\mathbf{x}(t) = \begin{pmatrix} c^{AC}_{\mathrm{CH_3OH}}(t) - c^{AC}_{\mathrm{CH_3OH},ss} \\ \theta_{\mathrm{COx}}(t) - \theta_{\mathrm{COx},ss} \\ \eta_A(t) - \eta_{A,ss} \\ c^{M}_{\mathrm{CH_3OH}}(t,x) - c^{AC}_{\mathrm{CH_3OH},ss}(x) \\ \eta_A(t) - \eta_{A,ss} \end{pmatrix} \tag{2.20}$$

Laplace transformation ($t \rightarrow s; y(t) \rightarrow Y(s); u(t) \rightarrow U(s); \mathbf{x}(t) \rightarrow \mathbf{X}(s)$) of this equation set yields the transfer function $G(s)$, which is the ratio of output to input variable:

$$G(s) = Y(s)/U(s) = B(sI - A)^{-1}C + D \tag{2.21}$$

$Y(s)$ is the Laplace transformed output variable, and $U(s)$ is the Laplace transformed input variable. Instead of calculating the global transfer function using all equations at once, the system can be decomposed into single modules which are interconnected as shown in the block diagram in Fig. 2.9. This decomposition is done with regard to the different functional layers of the DMFC: Anode catalyst layer (G_A), cathode catalyst layer (G_C) and membrane (G_M). Subsequently, the anode catalyst layer is decomposed into the different state variables: Methanol concentration (G_{AC}), COx surface coverage (G_{AT}) and anode catalyst charge (G_{AE}). This method of decomposition has the advantage that the mathematical description of the single modules can be taken from a transfer function library. Besides the descriptions derived from eqs. 2.3 - 2.12, this library contains various alternative mathematical descriptions for each state variable. The appropriate description has to be chosen according to the model variant. Four different model variants are investigated in the following sections. An overview is given in Fig. 2.9 (r.h.s.).

The experimental input $u(t)$ shows a step in cell current density, which in the Laplace domain gives $U(s) = \Delta u/s$, where Δu is the step size $\Delta u = i_{cell,t>0} - i_{cell,ss}$.
Based on the observation that the experimental voltage typically overshoots directly after the current step, a criterion in the Laplace domain for overshooting is formulated: The transfer function $G(s)$ is written in the pole-zero form,

$$G(s) = k\frac{\prod_{i=1}^{n}(s - Z_i)}{\prod_{i=1}^{n}(s - P_i)} \tag{2.22}$$

where Z_i are the zeros or roots of the numerator polynomial and P_i are the poles, i.e. the roots of the denominator polynomial. The number of poles and zeros is the

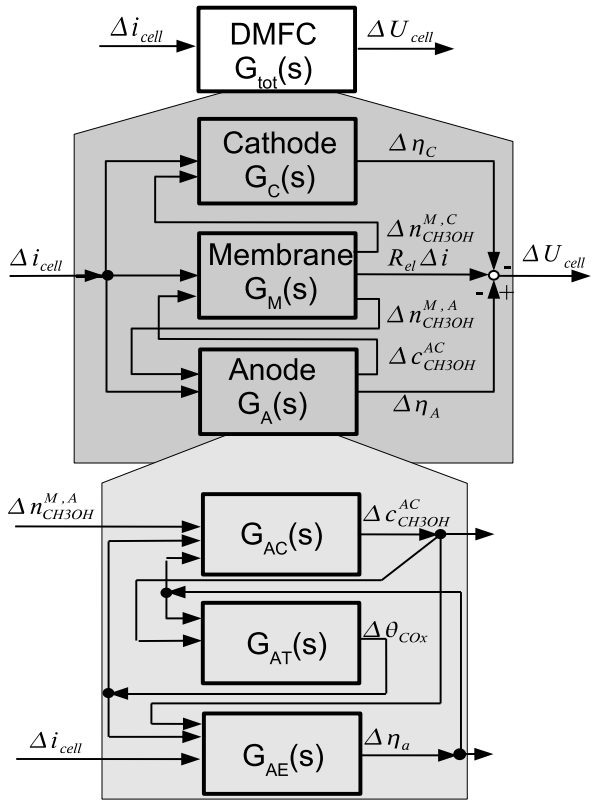

	Model variant			
	1x	2x	2x+m	4x
G_{tot}	$G_{tot}(s)$	$G_{tot}(s)$	$G_{tot}(s)$	$G_{tot}(s)$
G_C	G_C	G_C	G_C	$G_C(s)$
G_M	G_M	G_M	$G_M(s)$	G_M
G_A	$G_A(s)$	$G_A(s)$	$G_A(s)$	$G_A(s)$
G_{AC}	$G_{AC}(s)$	$G_{AC}(s)$	$G_{AC}(s)$	$G_{AC}(s)$
G_{AT}	-	$G_{AT}(s)$	$G_{AT}(s)$	$G_{AT}(s)$
G_{AE}	G_{AE}	G_{AE}	G_{AE}	$G_{AE}(s)$

Figure 2.9: Representation of the DMFC as a transfer function block diagram (l.h.s.) and an overview of the presented model variants (r.h.s.). Constant transfer functions are obtained whenever a quasi-steady state is assumed for the respective variable.

same, as soon as $D \neq 0$. As illustrated in Fig. 2.10, in case of overshooting, the system response has its maximum absolute value at $t \to 0^+$, i.e. $\lim_{t\to 0} |y(t)|$, and decreases for $t \to \infty$ towards a new steady state with a smaller absolute value, i.e. $\lim_{t\to\infty} |y(t)|$. Final value theorem and initial value theorem then result in:

$$\lim_{t\to 0} y(t) = \lim_{s\to\infty} Y(s)s = \lim_{s\to\infty} G(s)\Delta u = k\Delta u \tag{2.23}$$

$$\lim_{t\to\infty} y(t) = \lim_{s\to 0} Y(s)s = \lim_{s\to 0} G(s)\Delta u = k\Delta u \frac{\prod_{i=1}^{n}(-Z_i)}{\prod_{i=1}^{n}(-P_i)} \tag{2.24}$$

Finally, the condition

$$\lim_{t\to 0} |y(t)| > \lim_{t\to\infty} |y(t)| \tag{2.25}$$

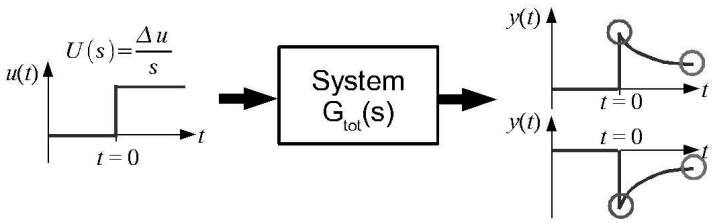

Figure 2.10: Illustration of overshooting system behaviour.

yields the overshoot criterion:

$$|\prod_{i=1}^{n} P_i| > |\prod_{i=1}^{n} Z_i| \tag{2.26}$$

The following sections investigate the four model variants being listed in Fig. 2.9.

2.3.3 Reaction-model with One State Variable (1x-model)

The given set of balance equations, (eqs. 2.3-2.7), represents different dynamic processes which interact with each other. To study and understand the model and the influences of the various phenomena, a study of the individual dynamic processes is helpful. A minimum dynamic model with one state variable, denoted in the following as 1x-model, is derived from eqs. 2.3-2.12. The most influential state variable is the methanol concentration in the catalyst layer: It is changing during a current step, influencing anode and cathode overpotential, as well as the methanol profile within the membrane. For the 1x-model the following assumptions are made:

- The balance equations for charge, eq. 2.5 and 2.7, and methanol inside the membrane, eq. 2.6, are in a quasi-steady state.
- The balance equation for methanol inside the anode catalyst layer, eq. 2.3, is the only dynamic equation.
- The methanol oxidation is assumed to take place without the reaction intermediate COx, therefore the rate expression r_{A1} has to be modified to match the overall reaction

$$CH_3OH + H_2O \rightarrow CO_2 + 6H^+ + 6e^- \tag{2.27}$$

This yields

$$r_{A1} = r_{A10} \frac{c^{AC}_{CH_3OH}}{c^{ref}_{CH_3OH}} \exp\left[\frac{\alpha_{A1} F}{RT} \eta_A\right] \tag{2.28}$$

Accordingly, the number of exchanged electrons in eq. 2.5 has to be changed from 4 to 6, and eq. 2.4 is dismissed.
Also, the description of mass transport through the membrane is simplified. The most simple mass transport model is a Fickian diffusion approach without any electroosmotic drag. Eq. 2.11 therefore reduces to:

$$n^{M}_{\mathrm{CH_3OH}} = \frac{D^{M}_{\mathrm{CH_3OH}}}{d^{M}} c^{AC}_{\mathrm{CH_3OH}} \tag{2.29}$$

This means, that a linear concentration profile in the membrane is assumed, and thus the flux density of methanol is constant all over the membrane:

$$n^{M,A}_{\mathrm{CH_3OH}} = n^{M,C}_{\mathrm{CH_3OH}} = n^{M}_{\mathrm{CH_3OH}} \tag{2.30}$$

Fig. 2.9 (r.h.s.) gives an overview of the transfer functions for the 1x-model which constitute the total transfer function. The singe transfer functions, $G_{AC}(s)$, G_{AE}, G_M and G_C, are presented in Appendix B.1.1.

Applying the overshoot criterion, eq. 2.26, on the derived model equations results in the following overshoot criterion:

$$i_{cell,ss} < i_{max} = \frac{6F D^{M}_{\mathrm{CH_3OH}} k^{AD} c^{AC}_{\mathrm{CH_3OH},ss} (\alpha_{A1} + \alpha_C - 1)}{d^{M}(k^{AD}(1-\alpha_C) + D^{M}_{\mathrm{CH_3OH}}/d^{M} \cdot \alpha_{A1})} \tag{2.31}$$

Obviously, there is a maximum initial steady state current density i_{max}, above which in any case no overshooting, and below which always overshooting will occur. It should be emphasized that with such a simple model of only one state variable, the voltage response can already show overshoots depending on the parameters. In case that both charge transfer coefficients, α_{A1} and α_C, are 0.5, i_{max} is 0, and no overshoots can occur. Fig. 2.11 (l.h.s.) shows the experimental cell voltage response for a current density step from 520 A/m^2 to 260 A/m^2 . In order to simulate this, all known parameters (values see Appendix B.2) are inserted in the model and the charge transfer coefficients α_{A1} and α_C are set to 0.5 (standard value). Parameters unknown are the anode and cathode reaction rate constants, r_{A10} and r_{C0}, respectively. They are estimated according to the following criteria. First, the cathodic reaction should be much faster than the anodic reaction. Second, the experimentally observed polarisation curve (Fig. 2.2) has to be fitted. Accordingly, the cathode reaction rate constant is chosen to be two orders of magnitude higher than the anode reaction rate constant, and the reaction parameters are adjusted to fit the experimental polarisation curve.
Fig. 2.11 (r.h.s., dotted line) shows the simulated voltage response (reaction parameters are given ibidem). With this set of parameters, no overshooting can occur according to eq. 2.31. The voltage response for charge transfer coefficients > 0.5 is shown in Fig. 2.11 (r.h.s., solid line). As expected for the given parameter

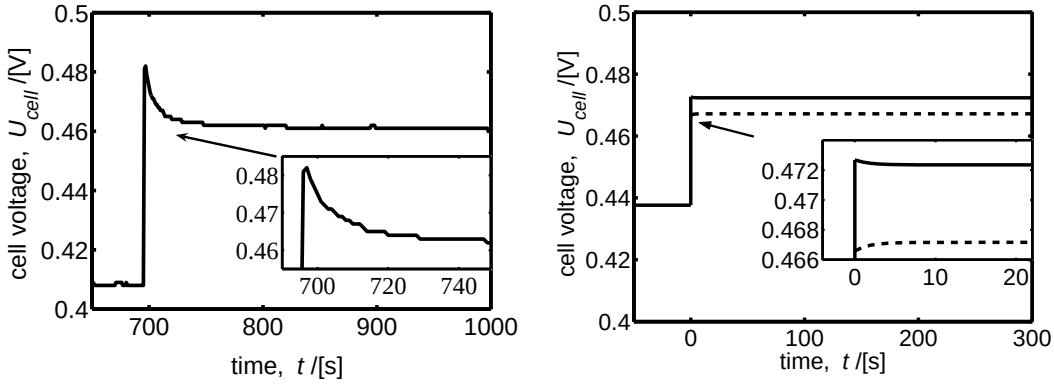

Figure 2.11: Experimental voltage response (l.h.s.) and voltage response of the 1x-model (r.h.s.) to a current step from 520 A/m^2 to 260 A/m^2: Overshoot response with $\alpha_{A1} = \alpha_C = 0.6$, $r_{A10} = 10^{-7}$ mol/m^2/s (solid), non-overshoot response with $\alpha_{A1} = \alpha_C = 0.5$, $r_{A10} = 1.4 \times 10^{-7}$ mol/m^2/s (dotted).

set, the voltage response shows overshooting ($i_{cell,ss} < i_{max}$). Qualitatively, the model's voltage response is similar to the experimental voltage response. Both have a maximum at $t = 0$ s and decrease slowly to the new steady state. Nonetheless, quantitative comparison shows significant differences. The model's absolute overshoot and the relaxation time are much smaller than the experimental values. The absolute overshoot, i.e. the difference between maximum voltage and new steady state voltage, is 20 mV in the experiment and approximately 10 times smaller in simulation. This may originate from the selected set of reaction parameters. The more important deviation is the relaxation time: While in the experiment it takes approximately 30 s to reach a new steady state, the steady state is reached within 5 s in the model. This suggests that the chosen storage capacity within the model is insufficient. As the only storage in the model is the anode catalyst layer volume which is given by the cell geometry and the layers' morphology, further additional storages should contribute to the experimentally observed phenomenon.

2.3.4 Reaction-adsorption Model with Two State Variables (2x-model)

As the 1x-model can not describe the experimental observations appropriately, the model is extended by introducing a second state variable $\theta_{\mathrm{CO}x}$, hence another storage. As explained in section 2.3.1, it is known that the electrochemical methanol oxidation follows a multi-step mechanism including at least one adsorption step, e.g. like in eqs. 2.1 and 2.2. The mass balance of the intermediate step is given in eq. 2.4, with the reaction rates r_{A1} and r_{A2} as in eqs. 2.8 and 2.9. The

description of mass transfer through the membrane is identical to the one in the 1x-model. The new model will be referred to as 2x-model due to its two state variables.
As in the 1x-model, the equation system is transformed into the Laplace domain. G_C and G_M are identical to the ones in the 1x-model. Due to the new state variable θ_{COx}, the transfer functions for the anode $G_{AC}(s)$, $G_{AT}(s)$ and G_{AE} change as given in Appendix B.1.2. The anode charge transfer coefficients are assumed to be identical ($\alpha_A = \alpha_{A1} = \alpha_{A2}$).

The overshoot criterion can be derived analogously to the 1x-model. All previous parameters are used, except for the reaction rate constants r_{A10} and r_{A20}. The cathode reaction rate constant of the 1x-model, including the assumption of a faster cathodic reaction, is adopted. The criterion for overshoot yields an implicit equation with three parameters: r_{A10}, r_{A20} and the initial steady state current density $i_{cell,ss}$. Since this equation is lengthy, it is not presented here. Furthermore, it can not be solved explicitly, but can be plotted as a plane in $\mathbb{R}^3$ with an algebraic mathematics program like Maple, as shown in Fig. 2.12 (top), where $i_{cell,ss}$ is plotted vs. the two reaction constants. The plane separates the overshoot region (l.h.s.) from the non-overshoot region (r.h.s.). It can be seen that the plane shows a slope. At each cell current density, there is a ratio of r_{A10} vs. r_{A20} above which overshooting occurs. Increasing this ratio results in a rise in the limiting cell current density. Hence, similar as in the 1x-model, for a set of reaction rate constants a maximum current density exists, above which no overshoot can occur.
Such behaviour was not observed in the experiments (see Fig. 2.5), steps from high initial cell current densities still produce overshoots. Mass transport limitation, which in the models is only accounted for in a simplified form, leads to a lower limiting current density in the experiments. This current density may be lower than the model's maximum current density for overshooting, $i_{cell,max}$, i.e. according to the model overshoot will always occur. Furthermore, the cell current steps conducted at higher current densities are far from being linear system deflections (see section 2.3.6), for which the model holds exclusively.

Fig. 2.12 (bottom) shows the separation line for the experimental initial current density of 520 A/m^2. Here, sets of parameters in the lower right region will result in overshooting behaviour. Due to the experimentally observed overshooting, the anode reaction parameters should be within the overshooting regime of Fig. 2.12 (bottom). The anode reaction parameters are fitted to the experimental polarisation curve, and the dynamic answer to the current density step from 520 A/m^2 to 260 A/m^2 is simulated. The result is shown in Fig. 2.13 (parameters are given ibidem or in Appendix B.2). While the absolute overshoot is still ten times lower than the experimental one, the relaxation time, approximately 30 seconds, is close

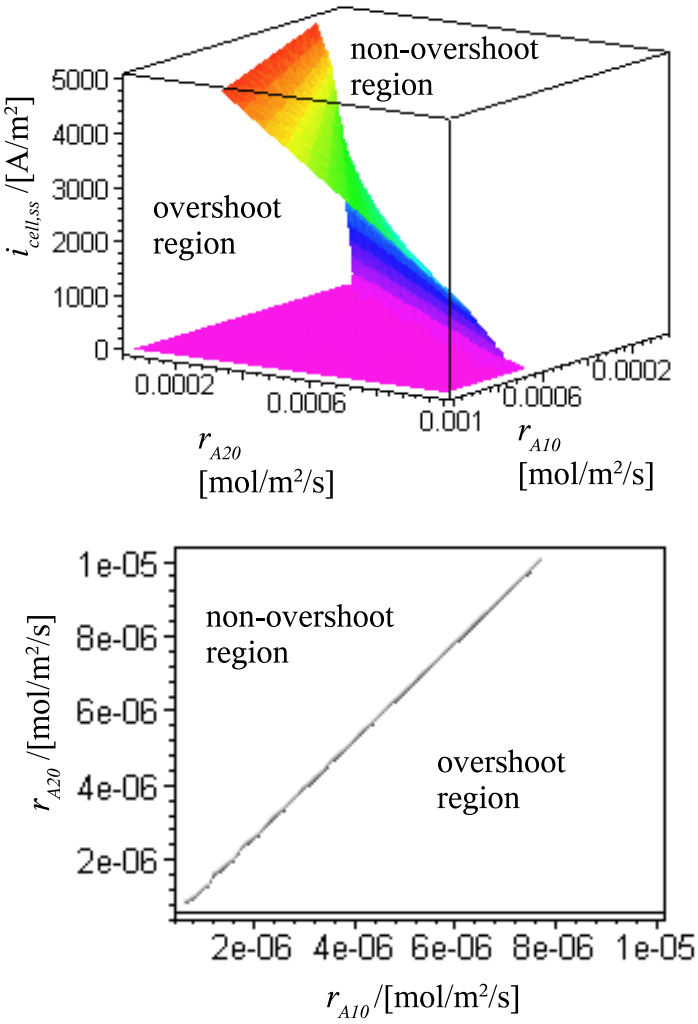

Figure 2.12: Analytically calculated separation plane/line between overshooting and non-overshooting region: Anode reaction constants vs. initial current density (top), anode reaction constants at initial current density $i_{cell,ss} = 520$ A/m^2 (bottom).

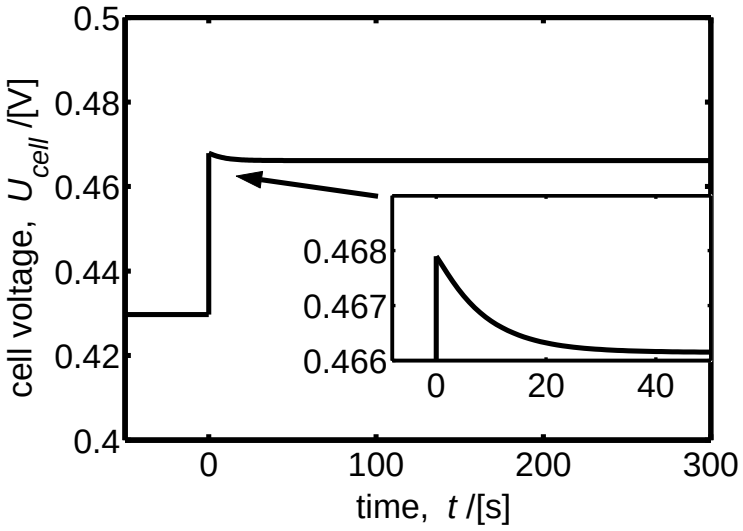

Figure 2.13: Voltage response of the 2x-model to a current step from 520 A/m^2 to 260 A/m^2 with $r_{A10} = 10^{-6}$ mol/m^2/s, $r_{A20} = 5 \times 10^{-8}$ mol/m^2/s.

to the experimental relaxation time, indicating more realistic modelling results. Therefore, a significant step towards a good fit to the experiments is achieved by the 2x-model.

Fig. 2.14 shows the result of the simulation of the numerically evaluated non-linear 2x-model (see section 2.3.6). It shows the transient response of $\theta_{\mathrm{CO}x}$, $c^{AC}_{\mathrm{CH_3OH}}$, η_A and η_C. As can be seen, the anode overpotential η_A is quite insensitive to changing concentrations of methanol and to changing COx surface coverages in the anode catalyst layer for time $t > 0$, while the cathode overpotential η_C shows a significant overshoot which is the reason for the overall cell voltage overshooting. The insensitivity of the anode overpotential to changes in methanol concentration at these low cell current densities has also been observed in steady state experiments (half-cell measurements on a real fuel cell MEA [71], also [10]). In Fig. 2.14, it can be seen that as soon as the methanol concentration in the anode catalyst layer reaches a steady state, the methanol flux through the membrane reaches a steady state, and with this also the cathode overpotential.
This theoretical result supports the interpretation of the experimental observations at the end of section 2.2.3 and Fig. 2.6.

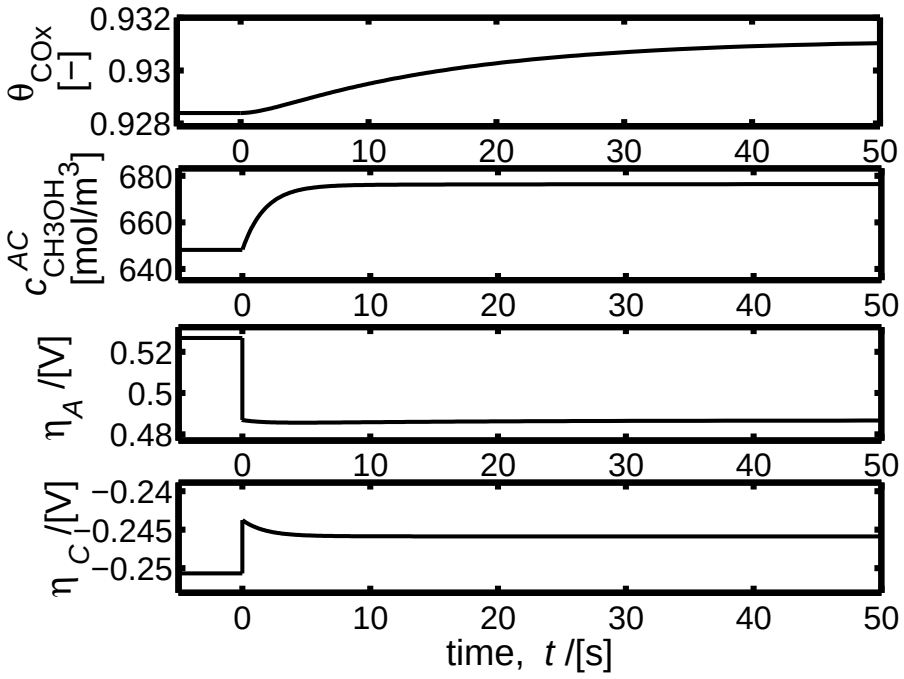

Figure 2.14: Concentration and overpotential responses of the non-linear 2x-model to a current step from 520 A/m^2 to 260 A/m^2. From top to bottom: COx-coverage, methanol concentration in the anode catalyst layer, anode overpotential, cathode overpotential.

2.3.5 Reaction-adsorption Model with Two State Variables and a Distributed Membrane (2x+m-model)

The 1x-model and the 2x-model are focussed on the anode reaction mechanism and its influence on the dynamic behaviour of the DMFC. The membrane dynamics is neglected there by assuming a steady-state linear concentration profile of methanol in the membrane. But recent studies by Schultz [57] indicate that the concentration profile of methanol in the membrane is not necessarily linear, and that the membrane is a significant storage for methanol. To investigate the influence of the dynamics of the membrane on the cell voltage response, the 2x-model is extended by a further state variable, which is the local concentration of methanol in the membrane. This model is denoted as 2x+m-model. Compared to the setup of the previous transfer function elements (G_C, $G_{AC}(s)$, $G_{AT}(s)$ and G_{AE} of the 2x-model hold for this model, too), the formulation of the dynamic membrane transfer function element $G_M(s)$ is more complex, since mass transport through the membrane is governed by a partial differential equation, see eqs. 2.6 and 2.11. The procedure is as follows: As can be seen in Fig. 2.9, the

input into the membrane module

$$U_M(s) = \begin{pmatrix} I(s) \\ C^{AC}_{CH_3OH}(s) \end{pmatrix} \tag{2.32}$$

and output out of the membrane module

$$Y_M(s) = \begin{pmatrix} N^{M,C}_{CH_3OH}(s) \\ d^M/\kappa^M \cdot I(s) \\ N^{M,A}_{CH_3OH}(s) \end{pmatrix}, \tag{2.33}$$

are coupled by a 3x2 transfer function matrix $G_M(s)$:

$$Y_M(s) = G_M(s) \cdot U_M(s) \tag{2.34}$$

with

$$G_M(s) = \begin{pmatrix} G_{M11}(s), & G_{M12}(s) \\ d^M/\kappa^M, & 0 \\ G_{M31}(s), & G_{M32}(s) \end{pmatrix} \tag{2.35}$$

$G_{M11}(s), G_{M12}(s), G_{M31}(s)$ and $G_{M32}(s)$ are functions of s. They are determined from eq. 2.6, which is linearised at the steady state operating point.
Concerning the boundary conditions, the following assumptions are made:

- Methanol concentration in the membrane at the spatial coordinate z=0, where the membrane is in contact with the anode catalyst layer, is identical to the concentration in the anode catalyst layer, i.e.

$$c^M_{CH_3OH}(z = 0) = c^{AC}_{CH_3OH}, \tag{2.36}$$

- Methanol concentration in the membrane at $z = d^M$, where the membrane is in contact with the cathode catalyst layer, is assumed to be zero due to the total electrooxidation of methanol, i.e.

$$c^M_{CH_3OH}(z = d^M) = c^{CC}_{CH_3OH} = 0. \tag{2.37}$$

Then, the following linearised partial differential equation results:

$$\begin{aligned} \frac{\partial x}{\partial t} &= D^M_{CH_3OH}\frac{\partial^2 x}{\partial z^2} - k_{\phi 2} i_{cell,ss}\,\frac{\partial x}{\partial z} + \\ &\quad + \frac{{k_{\phi 2}}^2\; c^{AC}_{CH_3OH,ss}\; i_{cell,ss}}{D^M_{CH_3OH}}\;\frac{e^{Pe_{ss}(z/d^M-1)}}{1-e^{-Pe_{ss}}}(i_{cell} - i_{cell,ss}) \end{aligned} \tag{2.38}$$

where the Peclet number

$$Pe_{ss} = \frac{k_{\phi 2}\ d^M\ i_{cell,ss}}{D^M_{\mathrm{CH_3OH}}} \tag{2.39}$$

and $x = (c^M_{\mathrm{CH_3OH}} - c^M_{\mathrm{CH_3OH},ss})$. The initial condition is

$$x(t=0,z) = 0, \tag{2.40}$$

and the boundary conditions are:

$$x(t,z=0) = c^{AC}_{\mathrm{CH_3OH}} - c^{AC}_{\mathrm{CH_3OH},ss}, \quad x(t,z=d^M) = 0 \tag{2.41}$$

Laplace transformation yields the following ordinary differential equation:

$$\begin{aligned} D^M_{\mathrm{CH_3OH}} X''(s,z) \quad &- \quad k_{\phi 2}\ i_{cell,ss}\ X'(s,z) - sX(s,z) = \\ &- \quad \frac{{k_{\phi 2}}^2\ c^{AC}_{\mathrm{CH_3OH},ss}\ i_{cell,ss}}{D^M_{\mathrm{CH_3OH}}}\ \frac{e^{Pe_{ss}(z/d^M-1)}}{1-e^{-Pe_{ss}}}\ I(s) \end{aligned} \tag{2.42}$$

with $X(s,z=0) = C^{AC}_{\mathrm{CH_3OH}}(s), \quad X(s,z=d^M) = 0$.
After solving this equation analytically and inserting the result $X(s,z)$ into the Laplace transform of the linearised eq. 2.11:

$$N(s,z) = -D^M_{\mathrm{CH_3OH}}\ X'(s,z) + k_{\phi 2}\ i_{cell,ss}\ X(s,z) + k_{\phi 2}\ c_{\mathrm{CH_3OH},ss}(z)\ I(s), \tag{2.43}$$

a Laplace transform of the methanol mass flow is obtained, which can be cast into the following form:

$$N(s,z) = b_1(s,z)\ X(s,z) + b_2(s,z)\ I(s), \tag{2.44}$$

b_1 and b_2 are complex functions of s and z (see Appendix B.1.3).
The transfer function elements demanded in eq. 2.35 are obtained from eq. 2.44 at the coordinates $z = 0$ and $z = d^M$:

$$\begin{aligned} G_{M11}(s) = \quad & \frac{{k_{\phi 2}}^2\ c^{AC}_{\mathrm{CH_3OH},ss}\ i_{cell,ss}}{2\ d^M}\ \frac{e^{-Pe_{ss}/2}}{1-e^{-Pe_{ss}}}\frac{1}{s} \\ & \cdot \left[-Pe_{ss}\ e^{Pe_{ss}/2} - 2\ F_1(s) + 2\ e^{Pe_{ss}/2}\ F_2(s)\right] \end{aligned} \tag{2.45}$$

$$G_{M12}(s) = \quad \frac{D^M_{\mathrm{CH_3OH}}}{d^M}\ e^{Pe_{ss}/2}\ F_1(s) \tag{2.46}$$

$$\begin{aligned} G_{M31}(s) = \quad & k_{\phi 2}\ c^{AC}_{\mathrm{CH_3OH},ss} - \frac{{k_{\phi 2}}^2\ c^{AC}_{\mathrm{CH_3OH},ss}\ i_{cell,ss}}{2\ d^M}\ \frac{e^{-Pe_{ss}}}{1-e^{-Pe_{ss}}}\ \frac{1}{s} \\ & \cdot \left[Pe_{ss} - 2e^{Pe_{ss}/2}\ F_1(s) + 2\ F_2(s)\right] \end{aligned} \tag{2.47}$$

$$G_{M32}(s) = \quad -\frac{D^M_{\mathrm{CH_3OH}}\ Pe_{ss}}{2\ d^M} + k_{\phi 2}\ i_{cell,ss} + \frac{D^M_{\mathrm{CH_3OH}}}{d^M}\ F_2(s) \tag{2.48}$$

with

$$F_1(s) = \frac{\sqrt{(\frac{Pe_{ss}}{2})^2 + \frac{(d^M)^2}{D^M_{\mathrm{CH_3OH}}}s}}{\sinh\sqrt{(\frac{Pe_{ss}}{2})^2 + \frac{(d^M)^2}{D^M_{\mathrm{CH_3OH}}}s}} \tag{2.49}$$

$$F_2(s) = \frac{\sqrt{(\frac{Pe_{ss}}{2})^2 + \frac{(d^M)^2}{D^M_{\mathrm{CH_3OH}}}s}}{\tanh\sqrt{(\frac{Pe_{ss}}{2})^2 + \frac{(d^M)^2}{D^M_{\mathrm{CH_3OH}}}s}} \tag{2.50}$$

These transfer functions are transcendental functions, and thus using them in this form would not result in a rational transfer function for the fuel cell (eq. 2.22). Hence, neither can this function be used for controlling purposes nor can an overshoot analysis be carried out according to eq. 2.26. There exist several methods to approximate transcendental transfer functions by rational functions, see e.g. [75]. A reliable analytical solution is obtained via a combination of the residue theorem and the Laplace transformation. Step one is the transformation of the inverse Laplace transformation integral into a contour integral with a semicircle of radius $\rho \to \infty$:

$$y(t) = \frac{1}{2\pi\mathrm{j}}\int_{c-\mathrm{j}\infty}^{c+\mathrm{j}\infty} Y(s)e^{st}ds = \frac{1}{2\pi\mathrm{j}}\oint_{\rho\to\infty} Y(s)e^{st}ds \tag{2.51}$$

If all singularities of Y(s) are inside this region and if

$$\lim_{s\to\infty} Y(s) = 0, \tag{2.52}$$

according to the residue theorem, the system answer in the time domain $y(t)$ can be calculated by the sum of the contour integrals around each singularity P_i:

$$y(t) = \frac{1}{2\pi\mathrm{j}}\oint_{\rho\to\infty} Y(s)e^{st}ds = \sum_{i=1}^{\infty} res_i \tag{2.53}$$

with

$$res_i = \frac{1}{2\pi\mathrm{j}}\oint_{\rho\to 0, at P_i} Y(s)e^{st}ds \tag{2.54}$$

Integration of this equation yields:

$$res_i = \lim_{s\to P_i}(s - P_i)Y(s)e^{st} = const\ e^{P_i\cdot t} \tag{2.55}$$

Since the Laplace transform of $e^{P_i \cdot t}$ is $\frac{1}{s-P_i}$, $y(t)$ can be transformed into the Laplace domain, resulting in the following rational form of the transfer function:

$$Y_{rat}(s) = \sum_{i=1}^{\infty} \left[\lim_{s \to P_i} (s - P_i) Y(s) \right] \frac{1}{s - P_i} \tag{2.56}$$

For functions with an infinite number of singularities, the higher terms represent faster dynamic modes ($\leq$ milliseconds) and more negative singularities P_i. These become irrelevant for the contemplated order of magnitude of experimental relaxation times (seconds - minutes). Since the transfer function should have the same stationary gain as $Y(s)$, i.e. $Y(0)$ according to the final value theorem, the sum in equation 2.56 is convergent for $s = 0$. Therefore, a good approximation can be achieved by truncating the series after the time-relevant m terms, i.e. time-relevant m singularities, and correcting for the stationary gain:

$$Y(s) \approx Y_{rat}(s) - Y_{rat}(0) + Y(0) \tag{2.57}$$

This rationalising procedure is applied to the transcendental parts F_1 (eq. 2.49) and F_2 (eq. 2.50) of the transfer functions, $G_{M11}(s)$ to $G_{M32}(s)$:

$$F_1(s) \rightarrow \quad F_{1,rat} = \sum_{i=1}^{m} \left[\lim_{s \to P_i} (-1)^{k+1} \frac{(\frac{Pe_{ss}}{2})^2 + k^2\pi^2}{\frac{(d^M)^2}{D^{AC}_{CH_3OH}}} \right] \frac{1}{s - P_i} \tag{2.58}$$

$$F_2(s) \rightarrow \quad F_{2,rat} = \sum_{i=1}^{m} \left[\lim_{s \to P_i} -\frac{(\frac{Pe_{ss}}{2})^2 + k^2\pi^2}{\frac{(d^M)^2}{D^{AC}_{CH_3OH}}} \right] \frac{1}{s - P_i} \tag{2.59}$$

$F_2(s)$ does not fulfill the condition in eq. 2.52, but $F_{2,rat}$ is still an adequate fit to the original function, as can be shown.
The new transfer functions are inserted into the block diagram (Fig. 2.9), and the cell voltage response to the experimental current step is simulated. The reaction parameters are identical to those of the 2x-model, as well as most of the other parameters (values see Appendix B.2). The results are displayed in Fig. 2.15 in comparison to the voltage response of the 2x-model. As can be seen, the relaxation time is identical to that of the 2x-model. Observed differences are a two seconds delay time until the maximum voltage is reached (discussion see next paragraph), and a lower steady state of the 2x+m-model. The absolute overshoot is slightly larger than for the 2x-model, but it is still small compared to the experimental voltage response, whose overshoot is 10 times larger. Hence, for the given parameter set and with regard to the experiment, the results of the 2x-model and the 2x+m-model are qualitatively equal.
Observing concentration and overpotential changes of the numerically evaluated nonlinear 2x+m-model in Fig. 2.16 (see section 2.3.6), the same effect as in the

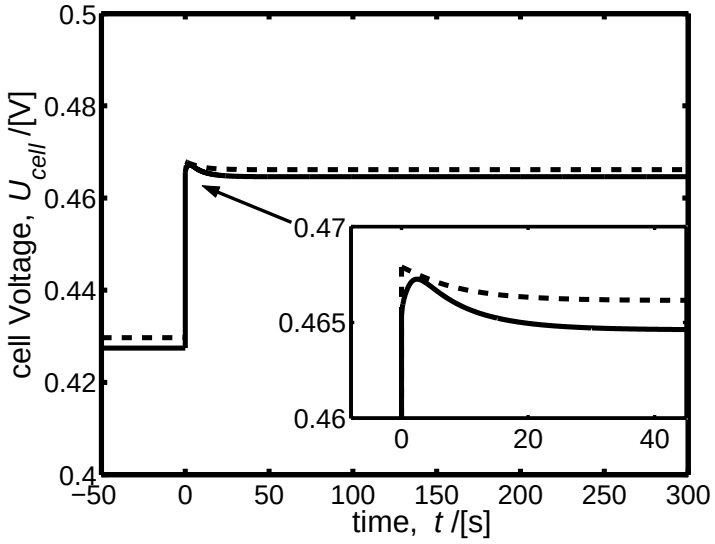

Figure 2.15: Comparison of voltage responses of the 2x+m-model (solid) and the 2x-model (dashed) to a current step from 520 A/m^2 to 260 A/m^2 with $r_{A10} = 10^{-6}$ mol/m^2/s, $r_{A20} = 5 \times 10^{-8}$ mol/m^2/s.

2x-model is observed: Methanol concentration dominates the dynamics of the cathode overpotential, and thus the cell voltage. Even after 50 seconds, the COx coverage is not in equilibrium.
The dynamic behaviour of the flux at the interface membrane/cathode shows the effect of the introduced osmotic drag term: Methanol flux instantaneously decreases at $t = 0$ due to the reduced current density, i.e. due to lower osmotic drag, while subsequently the anodic methanol concentration increases, causing a rise in the flux. This non-minimal phase behaviour leads to an overshooting of the cathode overpotential response and, as a consequence, the above presented overall cell voltage response (see Fig. 2.15) also overshoots. Just like in the 2x-model, the anode overpotential is quite insensitive to changes in the methanol feed concentration and surface coverage.

2.3.6 Discussion on Validity of the Transfer Function Models

The last two subsections presented dynamic responses of the 2x-model and the 2x+m-model. The responses were obtained by linearising the rigorous model equations around the steady state and simulating the voltage transient to a current step, using Laplace transformation. As can be seen from the results, the linearised models can describe the observed experimental behaviour qualitatively, but not quantitatively.

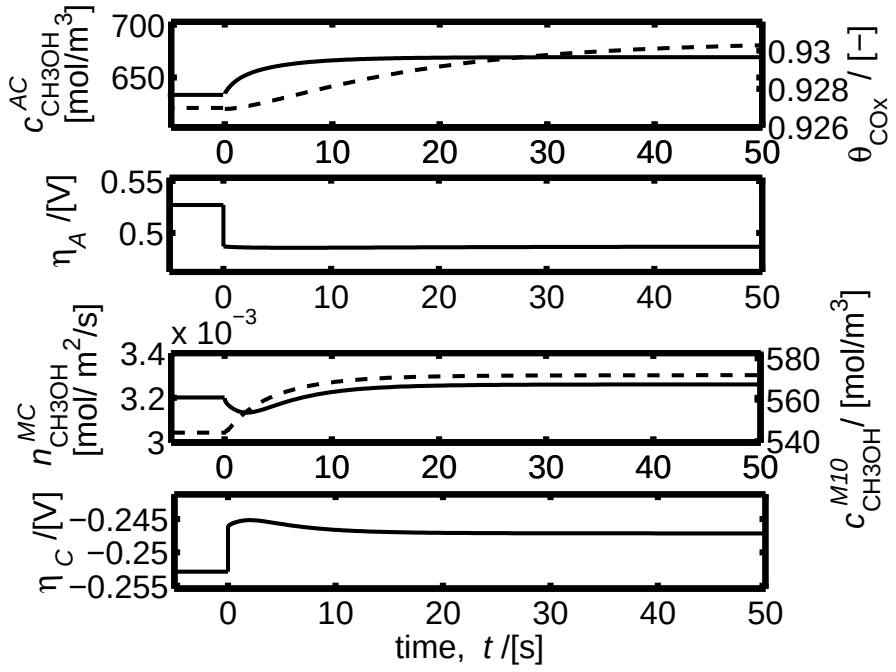

Figure 2.16: Concentrations and overpotential responses of the nonlinear 2x+m-model to a current step from 520 A/m^2 to 260 A/m^2. From top to bottom: Methanol concentration and surface coverage in the anode catalyst layer, anode overpotential, methanol flux at the interface membrane/cathode catalyst layer and methanol concentration in the membrane (tenth discretisation element of 50 elements in total), cathode overpotential.

Between the current densities of 520 A/m^2 and 260 A/m^2, the experimental polarisation curve is approximately linear (see Fig. 2.2). Therefore, the simulation with linearised models seems justified. This will be shown in the following for the two models.

For comparison with the linearised transfer function models, the nonlinear system answers of the 2x-model and the 2x+m-model have been simulated by numerical solving the respective set of nonlinear differential equations (see also Fig. 2.14 and 2.16). Both, the nonlinear and linear system answers are presented in Fig. 2.17 (top) for comparison. As can be seen for both, the 2x-model and the 2x+m-model, voltage responses of the linearised and nonlinear systems have the same shape except that the nonlinear answers are shifted to higher voltages. This shift is due to the deviation of the polarisation curve from the tangent of the polarisation curve at the initial current density. A quantitative analysis of the deviation is given in Fig. 2.17 (bottom), where the relative errors of the linear models vs. the nonlinear models are plotted. It can be seen for the 2x-model that the relative error in the steady state is quite small (2.4%). Even less, approximately 0.02%,

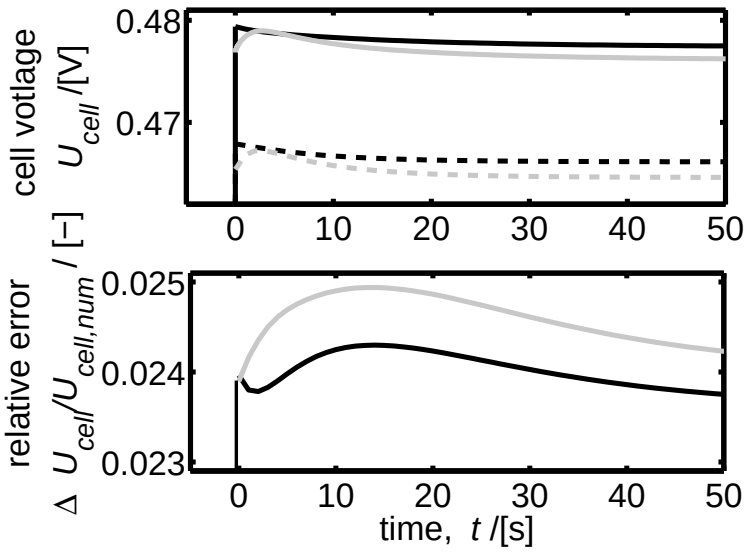

Figure 2.17: Comparison of linear models with non-linear models. Top: Voltage response of non-linear models (2x: solid black; 2x+m: solid grey) and transfer function models (2x: dashed black; 2x+m: dashed grey). Bottom: Relative error of linear compared to non-linear responses of the 2x-model (black) and the 2x+m-model (grey).

is the change of this error vs. time. Therefore, it can be concluded that the linearised 2x-model is equivalent to the nonlinear 2x-model for the given current step. This may change with increasing current step size where the deviation from the polarisation curve will increase. The relative error of the linearised 2x+m-model is only slightly higher ($\approx 2.4\%$), and the variance of the error is in the same order as for the 2x-model. Also for the 2x+m-model, it therefore can be concluded that it is equivalent to its non-linear counterpart.

2.3.7 Reaction-adsorption-charge Model with Four State Variables (4x-model)

In all models presented in the previous sections, it was assumed that the time constants of the charge balances are much smaller than the time constants of the mass balances, which means that the charge balances are in equilibrium instantaneously, i.e. in a quasi-steady state. This assumption seems justified, since in the experiments the Ohmic part of the voltage change ($R^M \cdot \Delta i_{cell} = 3$ mV) is only a small part of the total steady-state voltage change (= 52 mV) for the standard current density step, i.e. from 520 A/m^2 to 260 A/m^2.
Nonetheless, if the given set of equations (eqs. 2.3-2.12) and parameters (see Appendix B.2) are reliable, a model including the dynamics of the charge balances

should deviate only marginally from the 2x-model. In the following, it will be shown how the system dynamics changes when the dynamics of the charge balances is not neglected. In addition to the two state variables $c^{AC}_{\mathrm{CH_3OH}}$ and $\theta_{\mathrm{CO}x}$ of the 2x-model, the state variables η_A and η_C, are described by dynamic balances (charge balances, eqs. 2.5 and 2.7). The model now consists of four state variables. It is subsequently denoted as 4x-model. The total transfer function is modified by exchanging the transfer function elements G_{AE} and G_C of the 2x-model (see block diagram, Fig. 2.9). The new functions, $G_{AE}(s)$ and $G_C(s)$, are given in Appendix B.1.4.

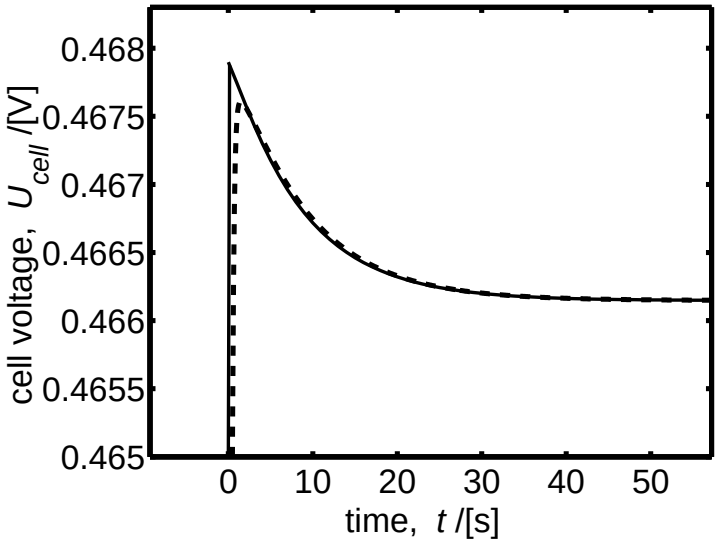

Figure 2.18: Voltage response of the 2x-model (solid) and 4x-model (dashed) to a current step from 520 A/m^2 to 260 A/m^2 with $r_{A10} = 10^{-6}$ mol/m^2/s, $r_{A20} = 5 \times 10^{-8}$ mol/m^2/s.

Using the same set of parameters as in the 2x-model, the dynamic voltage response is simulated for the current density step from 520 A/m^2 to 260 A/m^2. The voltage responses of the 2x-model and 4x-model are shown in Fig. 2.18. As can be seen, the time for reaching the new steady state is the same in both models. Five seconds after the current step both answers are identical. But, as expected, there is a slight discrepancy in the domain of the small time constants, i.e. in the first five seconds. In the 4x-model, the voltage can not step-up immediately to the new level at $t \to 0^+$, as it is found for the 2x-model, since the double layers first have to be charged. This charge takes place within three seconds, after which the voltage reaches its maximum. Compared to the initial large voltage changes due to the current step, in the subsequent time only small voltage changes due to concentration changes are observed, and the voltage decreases slowly. As a result,

comparing the absolute overshoots of the 2x-model and 4x-model, the overshoot of the 4x-model is 15% smaller than that of the 2x-model. Nonetheless, one has to take into account that the voltage response will always show this characteristic smoothing of the overshoot within the first few seconds (time depends on double layer capacitances), but the 4x-model will not contribute other dynamic effects to the system. Finally, the previously postulated assumption that the 4x-model deviates only marginally from the 2x-model proved correct, the set of equations showed the predicted behaviour, and for the sake of model reduction, the models with quasi-steady state charge balances may be used for modelling further on.

2.4 Concluding Remarks on the Governing Phenomena

Experimental cell voltage responses to load step changes were investigated based on a transfer function approach. The models presented here hold for analysis of a specific operating regime (low anode compartment residence time (< 1 s), low current densities), in which dynamic processes occuring inside the MEA are minimally influenced by mass transport phenomena like CO_2 bubble generation and concentration distribution in anode compartment.
Applying cell current steps to the DMFC, the voltage response in most cases showed significant overshooting behaviour. The peak height strongly varied depending on the position of the investigated steady state of the DMFC at the polarisation curve, hence on the dominating physico-chemical phenomena in different operating regimes. Switching to OCV caused relative overshoots of 80%. Understanding such dynamic effects is not only essential for DMFC operation, but also for understanding the processes occurring inside the cell.
Linear system analysis was applied to a set of dynamic models with different complexity. A criterion for cell voltage overshooting was developed, with which parameter domains for overshooting were analytically determined. Although even a model with only one state variable (methanol concentration in the anode catalyst layer) is able to generate cell voltage overshooting, a much better qualitative accordance with the experiments was achieved when introducing a consecutive reaction mechanism and thus using two dynamic state variables: The methanol concentration and the surface coverage of a methanol oxidation intermediate in the anode catalyst layer. The implementation of additional dynamic state variables (methanol concentration in the membrane, cathode and anode overpotentials), for the given parameter set, led to only slightly different results. In all investigated model variants, the dominating physico-chemical phenomena causing the overshoot were the same: Transport of methanol through the membrane caused cathode overpotential overshooting while anode overpotential proved to be rather insensitive to methanol concentration changes. Methanol transport,

and as a result, cell voltage reaches a steady state as soon as the methanol and intermediate species balances reach a steady state.
Nonetheless, with the presented models the observed overshoot height can not be quantitatively reproduced, indicating that a yet unidentified phenomenon contributes to the experimentally observed dynamic cell behaviour. Comparing the cell voltage response of the 1x-model (Fig. 2.11, dotted line), which uses a 1-step methanol oxidation mechanism, with the 2x-model response (Fig. 2.13), where a 2-step methanol oxidation mechanism is implemented, illustrates that a change of the methanol oxidation kinetics can strongly affect the dynamic behaviour of DMFC models. As will be shown in chapter 3, a refined kinetic description, which additionally takes into account a water chemisorption step parallel to the methanol partial oxidation and intermediate oxidation steps, can contribute to quantitatively describe the observed dynamic behaviour.

Chapter 3

Dynamic Aspects of Methanol Oxidation

3.1 Introduction

The overall decomposition of methanol

$$CH_3OH + H_2O \rightarrow 6H^+ + 6e^- + CO_2, \tag{3.1}$$

can only proceed via various reaction steps. As already discussed, at least one of these steps involves a strongly adsorbed intermediate which determines the overall oxidation rate. A vast amount of research on methanol oxidation can be found in the literature [8, 9, 20, 33, 34, 37, 38, 40, 41, 45, 71, 72, 76]. Most of the research nowadays is conducted on binary Pt/Ru catalysts [20, 33, 41, 71], since they are the most active and stable catalysts for methanol oxidation. The addition of small amounts of other metals [26, 28, 46] showed no significant improvement of the catalyst activity. It is accepted that the enhancement of the reaction rate for methanol oxidation on PtRu catalyst compared to pure Pt catalyst is due to a bifunctional mechanism where Pt is responsible for methanol adsorption and dehydrogenation, and Ru for OH adsorption which commences at lower overpotentials than on platinum itself [35]. Moreover, an electronic effect between Pt and Ru decreases the strength of the bond between an adsorbed intermediate and the Pt surface. This increases the methanol oxidation rate on PtRu catalyst compared to pure Pt even for the same surface coverage of CO and OH [29].
As shown in chapter 2, knowledge of the reaction mechanism is relevant for understanding and optimising the DMFC behaviour. Simulations with a simple one-step reaction mechanism or a consecutive two-step reaction mechanism can not reproduce the behaviour quantitatively, but they show that the methanol oxidation mechanism on the anode has a strong influence on the dynamic behaviour. Furthermore, understanding the mechanism may help generating better

catalysts as well as developing control strategies to improve the power output, e.g. by periodically removing adsorbed species.

Most experimental investigations on the reaction mechanism of methanol oxidation are performed using non-technical electrodes, e.g. on monocrystals or smooth surfaces [9, 34, 37, 38, 40, 45, 72, 76]. They focus on the detection of adsorbed species or products. Using different analysis techniques (CV, FTIR, FTIR-DRS, DEMS, etc.), more than ten adsorbed methanol derivates were detected or postulated: $(CO)_{ads}$, $(COH)_{ads}$, $(CHO)_{ads}$, $(COOH)_{ads}$, $(OCH_3)_{ads}$, $(OCH_2)_{ads}$, $(OCH_3)_{ads}$, $(CHOH)_{ads}$, $(CH_2OH)_{ads}$, and $(CH_3OH)_{ads}$. Due to the deviation of the experimental conditions to real fuel cell conditions (electrode structure, temperature, additional chemicals, no diffusion layer, etc.), they are not all equally important for the reaction inside the DMFC. Summarising the main experimental findings in the literature, the following reaction pathways can be formulated:

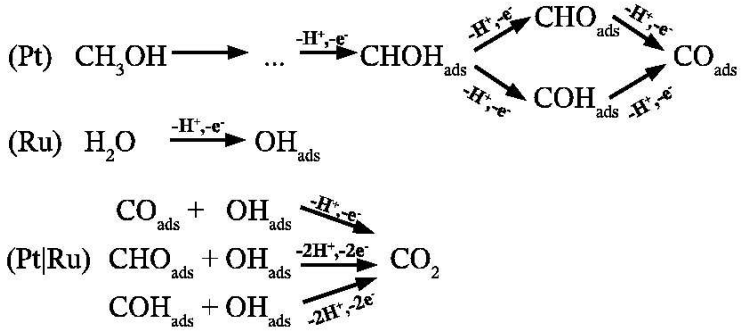

The aim of this chapter is to present the application of electrochemical impedance spectroscopy (EIS) as a dynamic method for identifying an adequate reaction kinetics. A lumped reaction mechanism based on the reaction scheme above is discussed (section 3.3.1). The reaction mechanism and four different kinetic formulations are based on [71]. All models can predict quantitatively the steady state experiments, but not the dynamic behaviour. Impedance spectra are modelled by using frequency domain transformed transfer functions that were derived from the governing system equations. In contrast to equivalent circuit models, these models do not contain empirical elements. An in-depth investigation of the parameter influence on the impedance spectra is presented, highlighting the complex interaction of the parameters on the EIS (section 3.3.3). Recorded electrochemical impedance spectra are used for identifying a quantitative reaction kinetic model (section 3.3.4). This kinetic description is able to qualitatively and quantitatively describe the steady state and dynamic behaviour of the methanol oxidation on Pt/Ru anode catalysts, as well as the dynamic voltage overshoots observed in the experiments (section 3.4).

3.2 Experiments

The experimental investigations and the corresponding experimental conditions presented in this section were taken from the work of Vidakovic [70].

3.2.1 Working Electrode and Experimental Setup

The experiments were conducted on a membrane electrode assembly (MEA) which consisted of an anode catalyst layer and a Nafion 105 membrane. The MEA was prepared as described in section 2.2.1, but using a cathode loading of 0 g/cm^2. In addition, the anode catalyst side of the membrane, i.e. the working electrode, was hot pressed at 403 K at a pressure of 10 MPa during 3 minutes onto the TORAY carbon paper. The total geometric area of the MEA covered by the catalyst layer was 12.56 cm^2, but only 2.14 cm^2 were exposed to the anode and cathode compartment.

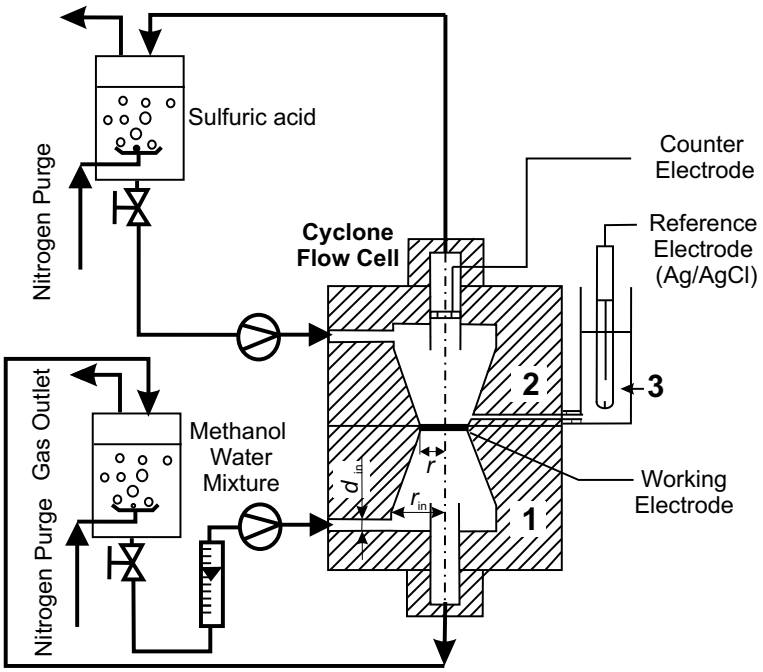

Figure 3.1: Schematic representation of the experimental setup: 1 - working electrode compartment, 2 - counter electrode compartment, 3 - reference electrode compartment.

The measurements were conducted in a special half cell setup [71] which resembles an idealised anode of a DMFC: It contains a MEA and shows minimal mass transport and cathode influence, as explained in the following.

• The setup is a cyclone flow cell, see Figure 3.1. Like in a fuel cell, a DMFC MEA separates the anode and cathode compartment. So the results can be directly used in complete DMFC models.
• The flow pattern inside the compartments is similar to the flow inside a cyclone, causing a homogeneous concentration distribution over the MEA.
• The setup enables measurements at a defined anode potential by using a reference electrode.

The cyclone flow cell consists of three compartments: Working electrode compartment (1), counter electrode compartment (2) and reference electrode compartment (3). As reference electrode, a saturated silver/silver chloride electrode (0.196 V vs. SHE) was used, but all potentials in this chapter are given vs. SHE. The working electrode compartment was supplied with an aqueous methanol solution (c_{CH_3OH}= 1 mol/l), while the counter electrode (2) and the reference electrode (3) compartments were supplied with an aqueous sulphuric acid solution ($c_{H_2SO_4}$= 1 mol/l). The reference electrode compartment was connected to the counter electrode compartment by a Luggin capillary. Due to the electric current in the liquid layer between the end of the Luggin capillary and the catalyst layer, the measured working electrode potential was corrected for corresponding Ohmic drop (see below). The electrolyte solutions were prepared from sulphuric acid (Merck, extra pure), methanol (Merck, extra pure) and ultrapure water (Millipore, 18 MΩ cm). Both working electrode compartment and counter electrode compartment supply containers were deaerated with nitrogen, and the deaerated solutions were circulated through the cell.
All electrochemical measurements were carried out with a Zahner impedance measurement unit (IM6e). Experiments were performed at a temperature of 333 K. The cell temperature was controlled by use of a Julabo F12 thermostat. For all electrochemical measurements, preconditioning of the membrane electrode assembly (MEA) was done by cyclic voltammetry in the potential range from 0 to 0.7 V at a sweep rate of 20 mV s^{-1}. Five cycles were enough to obtain a reproducible behaviour.

3.2.2 Electrochemical Impedance Measurements

After preconditioning the electrode, the potential was set to the desired point, and the current was recorded over time (30 min in methanol containing solution). Impedance measurements were performed afterwards at the same DC potential, over a frequency range between 2 kHz and 10 mHz. The amplitude of the sinusoidal signal was 5 mV (from base to peak). The measurements were corrected for Ohmic drop by subtracting the Ohmic resistance (impedance at high frequencies) from the real part of the impedance data. Electrochemical impedance spectra were recorded at the (Ohmic drop corrected) potentials 0.37 V, 0.41 V and 0.44 V at 333 K, using a 1 molar anodic methanol solution. These operating

conditions are identical to the conditions at dynamic operation of the DMFC, which allows the transfer of the kinetic results to DMFC models.
The frequency ranged from 2 kHz to 10 mHz. The recorded spectra are presented in Fig. 3.2 (concatenated symbols). The impedance plots all resemble depressed semicircles and feature a low frequency pseudo-inductive loop. EIS of depressed semicircle shape characterise surfaces with a high roughness [47]. Increasing the potential, the size of the overall EIS decreases which indicates that the charge transfer resistance for methanol oxidation becomes smaller. Pseudo-inductive behaviour in the low frequency region has been reported in the literature for methanol oxidation at smooth polycrystalline platinum [19], at carbon-supported Pt-nanoparticles [53] and at Pt/Ru fuel cell anodes [20]. Such pseudo-inductive patterns are known to be a typical feature of systems with adsorbed intermediates or with a transition between a passive and an active state [33].
The observed pseudo-inductive behaviour most probably can be attributed to a particular kinetic phenomenon characterising methanol oxidation. Hence, a good reproduction of the pseudo-inductive behaviour is compulsory for a realistic kinetic model.

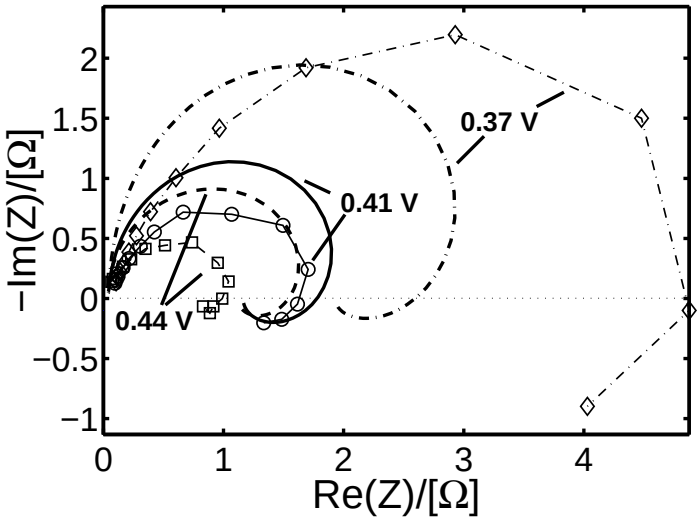

Figure 3.2: Experimental EIS (concatenated symbols) and simulated EIS (solid lines) of the VCS-Langmuir model with optimised parameters (values see Table 3.1) at three different electrode potentials.

3.3 Modelling the Electrochemical Impedance Spectra

3.3.1 Reaction Kinetic Descriptions

Based on the reaction pathways given above and on literature findings, the following mechanism for methanol oxidation was formulated [71]:

$$\text{(Pt)}\quad CH_3OH \xrightarrow{k_1} CH_3OH_{ads} \rightarrow ... \xrightarrow{-3H^+-3e^-} CO_{ads} + H^+ + e^- \tag{3.2}$$

$$\text{(Ru)}\quad H_2O \underset{k_{-2}}{\overset{k_2}{\rightleftharpoons}} OH_{ads} + H^+ + e^- \tag{3.3}$$

$$\text{(Pt/Ru)}\quad CO_{ads} + OH_{ads} \xrightarrow{k_3} CO_2 + H^+ + e^- \tag{3.4}$$

Vidakovic et al. [71] showed that the mass transport resistance from the anode compartment to the catalyst layer can be neglected when using the experimental setup of Fig. 3.1. The first mechanistic step relevant for modelling is therefore the partial oxidation of methanol, shown in eq. 3.2: Methanol physisorbs at Pt and is subsequently dehydrogenated to CO_{ads}. This process is supposed to occur only on the Pt adsorption sites. In a parallel reaction step (eq. 3.3), OH species are formed by dissociative adsorption of water on the Ru adsorption sites. The third reaction step (equation 3.4) represents the surface reaction between OH_{ads} and CO_{ads}, leading to CO_2 evolution.
To analyse the methanol oxidation kinetics, a set of non-linear mathematical models based on the above given reaction mechanism was developed accounting for the following phenomena:

- Irreversible electrochemical partial oxidation of methanol to the adsorbed intermediate CO_{ads}.
- Reversible electrochemical partial oxidation of water to the adsorbed intermediate OH_{ads}.
- Irreversible electrochemical or chemical reaction of adsorbed CO_{ads} and OH_{ads} to CO_2 (see below).

The following model assumptions were made:

- The methanol concentration in the anode catalyst layer is identical to the methanol feed concentration (minimised mass transport influences in the cyclone flow cell [71]).
- In the given temperature range, methanol adsorption occurs only on Pt.

- For the electrochemical partial oxidation of methanol (eq. 3.2), the first step (potential independent methanol physisorption) is considered to be the rate-determining step.
- In the given temperature range, water adsorption occurs only on Ru.
- Water concentration is constant since it is an excess component.
- A pure liquid phase mixture is assumed, i.e. gas-phase formation by release of carbon dioxide bubbles is not taken into account. Problems with bubble formation only get visible when working and modelling in or near the limiting current regime of the polarisation curve, which is not done here.
- The Ohmic drop can be neglected, since experiments were IR-corrected.

Based on the assumptions given above, balance equations for the surface coverage of the adsorbed intermediates CO_{ads} (eq. 3.5) and OH_{ads} (eq. 3.6), as well as for the anodic potential E (eq. 3.7) are formulated:

$$c_{\mathrm{Pt}} \cdot \frac{d\theta_{\mathrm{CO}}}{dt} = k_1^{eff}(\theta_{\mathrm{CO}}) \cdot c_{\mathrm{CH_3OH}} \cdot (1-\theta_{\mathrm{CO}}) - k_3^{eff}(E,\theta_{\mathrm{CO}}) \cdot \theta_{\mathrm{CO}} \cdot \theta_{\mathrm{OH}} \tag{3.5}$$

$$\begin{aligned} c_{\mathrm{Ru}} \cdot \frac{d\theta_{\mathrm{OH}}}{dt} &= k_2^{eff}(E,\theta_{\mathrm{OH}}) \cdot (1-\theta_{\mathrm{OH}}) - k_{-2}^{eff}(E,\theta_{\mathrm{OH}}) \cdot \theta_{\mathrm{OH}} \\ &\quad -k_3^{eff}(E,\theta_{\mathrm{CO}}) \cdot \theta_{\mathrm{CO}} \cdot \theta_{\mathrm{OH}} \end{aligned} \tag{3.6}$$

$$\begin{aligned} C^{AC} \cdot \frac{dE}{dt} &= i_{cell} - F[4 \cdot k_1^{eff}(\theta_{\mathrm{CO}}) \cdot c_{\mathrm{CH_3OH}} \cdot (1-\theta_{\mathrm{CO}}) + k_2^{eff}(E,\theta_{\mathrm{OH}}) \\ &\quad \cdot(1-\theta_{\mathrm{OH}}) - k_{-2}^{eff}(E,\theta_{\mathrm{OH}}) \cdot \theta_{\mathrm{OH}} + k_3^{eff}(E,\theta_{\mathrm{CO}}) \cdot \theta_{\mathrm{CO}} \cdot \theta_{\mathrm{OH}}] \end{aligned} \tag{3.7}$$

θ_{CO} and θ_{OH} are the fractional surface coverages of Pt with CO_{ads}, and Ru with OH_{ads}, respectively, and E is the anode potential (vs. SHE). $k_1^{eff}(\theta_{\mathrm{CO}})$, $k_2^{eff}(E,\theta_{\mathrm{OH}})$, $k_{-2}^{eff}(E,\theta_{\mathrm{OH}})$, and $k_3^{eff}(E,\theta_{\mathrm{CO}})$ are the effective reaction rate functions for reactions $i \in \{1,2,-2,3\}$. The rate functions contain different kinetic descriptions, which are defined later in this section. C^{AC}, c_{Pt} and c_{Ru} are the storage capacity for charge (i.e. the double layer capacitance), for CO (i.e. the Pt surface concentration), and for OH_{ads} (i.e. the Ru surface concentration), respectively. Setting the left side of the set of equations 3.5 - 3.7 to zero results in the steady state descriptions, in which the storage capacities have no influence. Formally, c_{Pt} and c_{Ru} influence the effective reaction rate functions $k_i^{eff}(E,\theta_{\mathrm{CO}},\theta_{\mathrm{OH}})$, but since these surface concentrations can not be separated from the reaction kinetic constants at steady state, they are incorporated in the reaction rate constants (see section 3.3.3).

In the literature, various dependences of the reaction rates on potential and surface coverage are given [2, 17, 34, 41, 48, 51, 68, 78]. In [71], five kinetic descriptions, assuming different adsorption mechanisms and potential dependences, are discussed and compared with regard to their influence on the polarisation curve. Based on these, here, four kinetic variants are presented which differ in the reaction rate functions $k_i^{eff}(E, \theta_{\mathrm{CO}}, \theta_{\mathrm{OH}})$.

The first distinction applies to the potential dependence of reaction step 3 (eq. 3.4): Vidakovic et al. [71] postulated a potential dependent surface reaction with

$$\mathrm{CO_{ads}} + \mathrm{OH_{ads}} \longrightarrow \mathrm{CO_2} + \mathrm{H^+} + \mathrm{e^-}, \tag{3.8}$$

while Kauranen et al. [41] assumed a consecutive reaction

$$\mathrm{CO_{ads}} + \mathrm{OH_{ads}} \xrightarrow{\text{r.d.s.}} \mathrm{COOH_{ads}} \longrightarrow \mathrm{CO_2} + \mathrm{H^+} + \mathrm{e^-}, \tag{3.9}$$

where the first reaction step, a chemical reaction, is the rate determining step. Reaction step 3 would be potential independent therefore. The potential dependent description will be referred to as VCS-model (author initials of [71]), and the potential independent description will be referred to as Kauranen.

In addition to the potential dependence, a second distinction is introduced with regard to the adsorption/desorption mechanism. It affects all three reaction rate functions. The most frequently used adsorption description, based on mechanistic considerations, is the Langmuir adsorption [2, 34, 48, 51, 68, 78]. Kauranen et al. [41] assume Frumkin/Temkin type adsorption for methanol on the Pt adsorption sites, but at the same time they use a Langmuir model for the adsorption of $\mathrm{OH_{ads}}$. Only in [17], Frumkin/Temkin type adsorption is assumed for all species. The assumption of Langmuir adsorption for $\mathrm{OH_{ads}}$ should yield a well-expressed peak in cyclic voltammograms in absence of methanol, which was not observed [71]. Hence, in case of introducing a Frumkin/Temkin type adsorption for $\mathrm{CO_{ads}}$, also Frumkin/Temkin type adsorption for $\mathrm{OH_{ads}}$ should be adopted. So, the second distinction is with regard to the adsorption/desorption mechanism, which is either a Langmuir-type adsorption or a Frumkin/Temkin type adsorption. The assumed adsorption mechanism then holds for all reaction steps.

Combining these two model distinctions (potential dependence of third reaction step, adsorption/desorption mechanisms) leads to four different kinetic variants: VCS-Langmuir, VCS-Frumkin/Temkin, Kauranen-Langmuir and Kauranen-Frumkin/Temkin.
Mathematically, the differences between the kinetic descriptions can be summarised in the reaction rate functions $k_1^{eff}(\theta_{\mathrm{CO}}), k_2^{eff}(E, \theta_{\mathrm{OH}}), k_{-2}^{eff}(E, \theta_{\mathrm{OH}})$ and

$k_3^{eff}(E, \theta_{\mathrm{CO}})$ for the reactions 1 to 3:

$$k_1^{eff}(\theta_{\mathrm{CO}}) = k_{1,0} \cdot \exp\left[-\beta_{\mathrm{CO}} g_{\mathrm{CO}}(\theta_{\mathrm{CO}} - 0.5)\right] \tag{3.10}$$

$$k_2^{eff}(E, \theta_{\mathrm{OH}}) = k_{2,0} \cdot \exp\left[\frac{\alpha_{a2} F}{RT} E\right] \cdot \exp\left[-\beta_{\mathrm{OH}} g_{\mathrm{OH}}(\theta_{\mathrm{OH}} - 0.5)\right] \tag{3.11}$$

$$k_{-2}^{eff}(E, \theta_{\mathrm{OH}}) = k_{-2,0} \cdot \exp\left[-\frac{(1-\alpha_{a2}) F}{RT} E\right] \cdot \exp\left[(1-\beta_{\mathrm{OH}}) g_{\mathrm{OH}}(\theta_{\mathrm{OH}} - 0.5)\right] \tag{3.12}$$

$$k_3^{eff}(E, \theta_{\mathrm{CO}}) = k_{3,0} \cdot \exp\left[\frac{\alpha_{a3} F}{RT} E\right] \cdot \exp\left[(1-\beta_{\mathrm{CO}}) g_{\mathrm{CO}}(\theta_{\mathrm{CO}} - 0.5)\right] \tag{3.13}$$

Here, $k_{i,0}$ is the reaction rate constant for reaction $i \in \{1, 2, -2, 3\}$, and α_{ai} is the charge transfer coefficient for reaction i. The assumption of the validity of the Kauranen kinetics yields a potential independent $k_3^{eff}(\theta_{\mathrm{CO}})$ with $\alpha_{a3} = 0$, whereas for the VCS kinetics $k_3^{eff}(E, \theta_{\mathrm{CO}})$ is potential dependent with $\alpha_{a3} = 0.5$. The distinction between dependence and independence of the adsorption/desorption energy on surface coverage yields for the first case (Frumkin/Temkin kinetics) an exponential term in all $k_i^{eff}(E, \theta_{\mathrm{CO}}, \theta_{\mathrm{OH}})$, consisting of the symmetry factor $\beta_i = 0.5$ (with $i \in \{\mathrm{CO_{ads}}, \mathrm{OH_{ads}}\}$), an inhomogeneity/interaction factor g_i, and the surface coverage. For the case that the adsorption energies are independent of surface coverage, i.e. for the Langmuir kinetics, the inhomogeneity factors are set to zero, i.e. $k_i^{eff} \neq f(\theta_{\mathrm{CO}}, \theta_{\mathrm{OH}})$.

Steady state measurements were presented in [71] for various methanol concentrations between 0.03 mol/l and 3 mol/l (at 333 K), as well as at various temperatures between room temperature and 333 K (at 1 mol/l). The experimental results were discussed and simulated in detail with kinetic models. All kinetic model variants were found to be able to describe satisfactorily the experimental results [71]. Since the steady state measurements and their concentration and temperature dependences have not been sufficient to discriminate between the kinetic descriptions, electrochemical impedance spectroscopy (EIS) is used here in addition. EIS has the further advantage of characterising a system in a dynamic state. It therefore yields important system information, which is necessary for modelling the dynamics of the DMFC adequately.

3.3.2 EIS Modelling Using Laplace Transformation

To simulate the recorded impedance spectra with the presented kinetic descriptions, the set of equations (eqs. 3.5-3.7, 3.10-3.13) is transformed into the frequency domain. In contrast to modelling EIS by means of equivalent circuits, in the approach applied here, the models have a direct physico-chemical relevance, since they do not contain empirical elements. For the SOFC, a similar approach

was chosen by the group of Gauckler [49], with the difference that the double layer charging influence was added as an equivalent circuit element.
The technique applied for modelling impedance spectra is mostly identical to the one applied in the dynamic analysis of the DMFC cell voltage responses (see section 2.3.2), since impedance spectroscopy represents a tool for linear system analysis: The input variable, either anode potential or cell current, is deflected only slightly from its quasi steady state. As in section 2.3.2, the input variable $u(t)$ is defined as the deflection of the current density from the steady state current density value, and the output variable $y(t)$ as the deviation of the anode potential from its steady state value. The vector of state variables $\mathbf{x}(t)$ is the deviation of the system variables from their steady state values.

$$u(t) = i_{cell}(t) - i_{cell,ss} \tag{3.14}$$

$$y(t) = E(t) - E_{ss} \tag{3.15}$$

$$\mathbf{x}(t) = \begin{pmatrix} \theta_{\mathrm{CO}}(t) - \theta_{\mathrm{CO},ss} \\ \theta_{\mathrm{OH}}(t) - \theta_{\mathrm{OH},ss} \\ E(t) - E_{ss} \end{pmatrix}. \tag{3.16}$$

The set of balance equations is cast into the state space form and thereby, the transfer function of the system can be derived. As done and motivated in section 2.3.2, the system is decomposed into single modules which are interconnected as shown in the block diagram in Fig. 3.3. The decomposition is done with regard to the different state variables: anodic CO_{ads} surface coverage (G_{ACO}), anodic OH_{ads} surface coverage (G_{AOH}) and anode potential (G_{AE}).
The different modules are added to the transfer function library introduced in section 2.3, so that they can also be integrated in dynamic DMFC models later on.
For EIS modelling, a further transformation from the Laplace domain to the frequency domain is done: The transfer function $G(s)$ is transferred into the frequency domain to yield the electrochemical impedance $Z(f)$ by exchanging the Laplace variable s with $\mathrm{j} \cdot 2\pi f$, where j is the imaginary unit and f is the frequency [50]. The resulting intensive impedance in units of $\Omega\mathrm{m}^2$ is divided by the cross sectional electrode area A_s to yield the extensive electrochemical impedance in Ω:

$$Z(f) = \frac{G(s = \mathrm{j} \cdot 2\pi f)}{A_s} \tag{3.17}$$

3.3.3 Qualitative Parameter Studies

In the following section, a qualitative parameter study is performed: The influence of model parameters on the impedance spectra is analysed, as well as the occurance of pseudo-inductive behaviour.

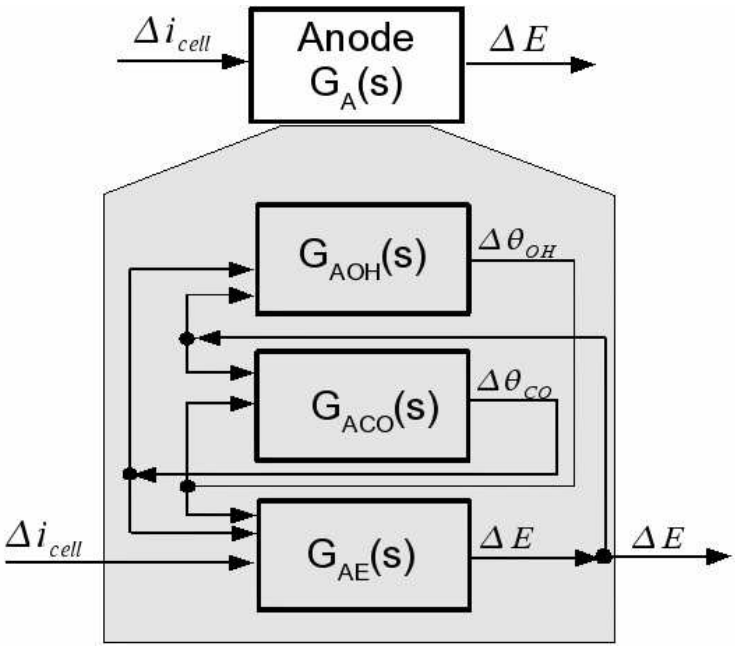

Figure 3.3: Representation of the anode catalyst layer as a transfer function block diagram.

The parameter sensitivity is studied for all four kinetic models. Since the dependence of the impedance spectra on the model parameters is similar in all models, the VCS-Langmuir model results are presented when investigating parameters that are relevant for all models, and the VCS-Frumkin/Temkin model is used for the study of the influence of the interaction factors g_{CO} and g_{OH}.

Reference Spectrum of the VCS-Langmuir model

First, a reference spectrum of the VCS-Langmuir kinetics with estimated parameters is generated. Based on these values, parameter variations are performed. The anode potential is set to 0.41 V, which is identical to the anode potential of one of the experimental EIS.
The following parameters have to be determined: $k_{i,0}$ ($i \in \{1, 2, -2, 3\}$), c_{Pt}, c_{Ru} and C^{AC}. The reference reaction rate constants $k^{\ominus}_{i,0}$ are chosen, so that reactions 1 and 3 have similar reaction rates, and reactions 2 and -2 are 100 times faster than reactions 1 and 3, i.e.: $k_1^{eff} \cdot c^{AC}_{\mathrm{CH_3OH}} = k_3^{eff}(E)$ and $k_2^{eff}(E = 0.41V) = k_{-2}^{eff}(E = 0.41V) = 100 \cdot k_3^{eff}(E = 0.41V)$.
This leads to the following parameter values: $k^{\ominus}_{1,0} = 1.37 \times 10^{-6}$ m s^{-1}, $k^{\ominus}_{2,0} = 110 \times 10^{-6}$ mol m^{-2} s^{-1}, $k^{\ominus}_{-2,0}$=171 mol m^{-2} s^{-1}, $k^{\ominus}_{3,0} = 1.1 \times 10^{-6}$ mol m^{-2} s^{-1}. The double layer capacitance $C^{AC,\ominus}$ ($\approx$ 1827 F m^{-2}) has been estimated experimentally from CV measurements (current vs. sweep rate plot, the difference

between anodic and cathodic currents at constant potential (0.3 V) is used to eliminate errors due to a faradaic reaction [23]).
Pt and Ru surface concentrations have been roughly estimated as $c^{\ominus}_{\mathrm{Pt}} = c^{\ominus}_{\mathrm{Ru}} = 0.0145$ mol m^{-2} from BET surface area measurements published in [16].

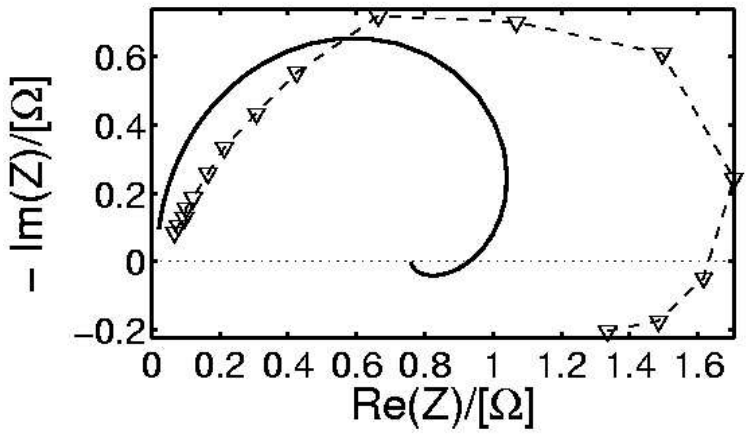

Figure 3.4: Reference EIS based on the VCS-Langmuir model (solid line) and experimental EIS (concatenated symbols). Anode potential: 0.41 V. Reaction rate constants are selected so that reaction rates of step 1 and step 3 are equally fast, and reaction 2 is in quasi equilibrium (values see text).

In Fig. 3.4, the reference spectrum (solid line), as well as the experimental spectrum (concatenated symbols) are presented. Although the size of the simulated spectrum is smaller than the experimental one, the simulated spectrum has a shape similar to the experimental one and it also shows pseudo-inductive behaviour. I.e., the given reaction kinetic model with parallel and consecutive reaction steps is able to generate a dynamic behaviour qualitatively similar to the experimental behaviour. The depressed shape of the EIS observed at medium and high frequencies can not be reproduced by the model, since this is due to the non-ideality of the electrode, as already discussed in the experimental section.

Variation of Reaction Rate Constants

A variation of the reaction rate constants $k_{1,0}$, $k_{2,0}$, $k_{-2,0}$ and $k_{3,0}$ shows the influence of a shifting influence of the reaction steps on the EIS. Fig. 3.5 shows the variation of $k_{1,0}$ from 0.25 times the original value to 10 times the original value. Deviation of $k_{1,0}$ from its original value $k^{\ominus}_{1,0}$, where reaction 1 and reaction 3 are equally influencing the overall reaction rate, should lead to the rate determination by either reaction 1 or reaction 3: Decreasing $k_{1,0}$ decreases the rate of step 1, and increases its influence on the overall reaction rate. On the other

hand, increasing $k_{1,0}$ decreases its influence, and reaction 3 becomes the rate determining step (r.d.s). This is reflected by the spectra: The overall impedance is inversely proportional to $k_{1,0}$. In addition, the pseudo-inductive behaviour depends strongly on $k_{1,0}$. Decreasing as well as increasing $k_{1,0}$ leads to a vanishing of the pseudo-inductive behaviour. Hence, there is only a small interval of parameter values in which this phenomenon occurs. According to these findings, a single rate determining step (either step 1 or step 3) most probably inhibits pseudo-inductive behaviour, and can therefore not be assumed.

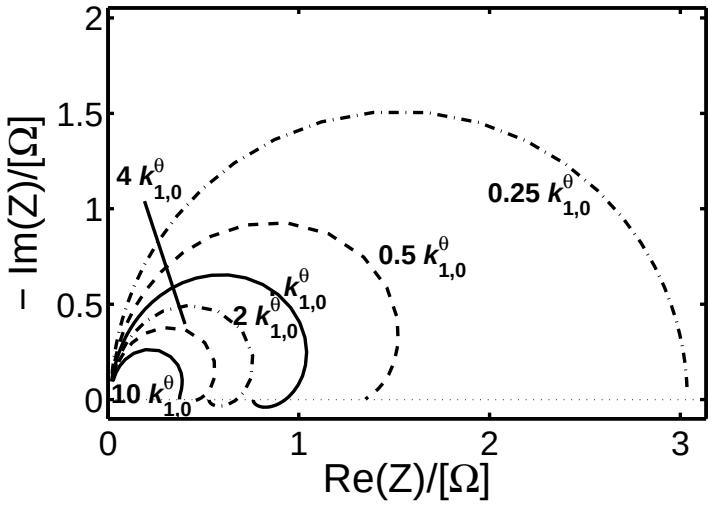

Figure 3.5: EIS of the VCS-Langmuir model: Reaction rate constant $k_{1,0}$ varied from the reference value $k_{1,0}^{\ominus}$.

Variation of $k_{3,0}$ supports this hypothesis. The respective EIS are shown in Fig. 3.6. Decreasing $k_{3,0}$ leads to a larger overall impedance and to a loss of the pseudo-inductive behaviour, since now only reaction 3 is determining the overall reaction resistance (reaction 3 is r.d.s.). On the other hand, an increase of $k_{3,0}$ leads to a lower impedance and also to a loss of the pseudo-inductive behaviour, i.e. at high $k_{3,0}$ reaction 1 is the rate determining step. Hence, only at roughly equal reaction rates of the two subsequent steps the phenomenon of pseudo-inductance occurs. This finding is in accordance with the result in [71] that there is no single rate determining step in methanol oxidation at medium potentials.

In contrast to reaction 1 and reaction 3, reaction 2 is supposed to be in quasi equilibrium. The variation of $k_{2,0}$ is shown in Fig. 3.7. A change in $k_{2,0}$ changes the equilibrium constant, i.e. the ratio $(k_{2,0}/k_{-2,0})$, producing more or less OH_{ads},

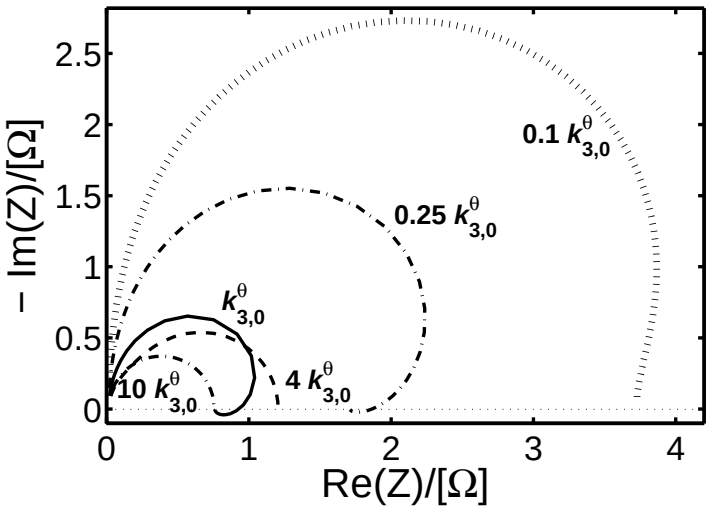

Figure 3.6: EIS of the VCS-Langmuir model: Reaction rate constant $k_{3,0}$ varied from the reference value $k^{\ominus}_{3,0}$.

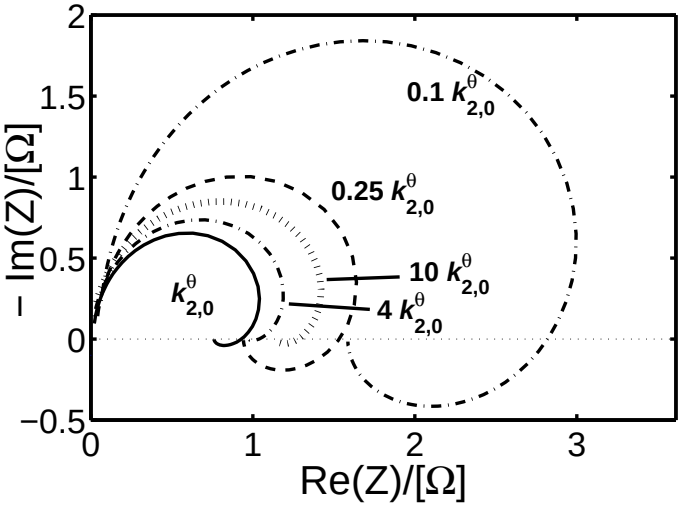

Figure 3.7: EIS of the VCS-Langmuir model with reaction rate constant $k_{2,0}$ varied from the reference value $k^{\ominus}_{2,0}$.

which in turn influences reaction 3. As can be seen, varying $k_{2,0}$ influences the pseudo-inductive behaviour: Its size changes, but it does not vanish. This indicates that the pseudo-inductive behaviour is caused by the subsequent reactions 1 and 3, and it is only connected indirectly to reaction 2 (via OH_{ads}). This is also in accordance with the variation of $k_{1,0}$ and $k_{3,0}$: As long as reaction 1 and reaction 3 have similar rates, the model produces a pseudo-inductive behaviour.

Finally, Fig. 3.8 shows the effect of the variation of $k_{-2,0}$. The spectra at $n \cdot k_{-2,0}$ (with $n \in \{0.25, 0.1, 4, 10\}$) deviate only slightly from the EIS at $1/n \cdot k_{2,0}$. This supports the assumption that a change in $k_{2,0}$ or $k_{-2,0}$ mainly influences the EIS via the equilibrium constant $k_{2,0}/k_{-2,0}$.

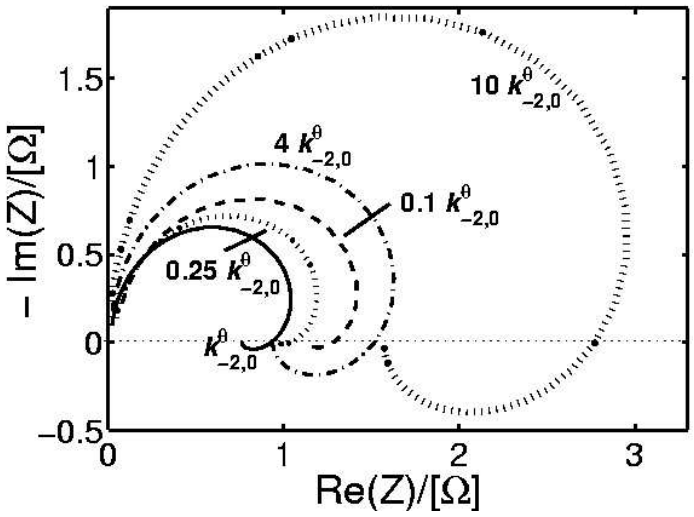

Figure 3.8: EIS of the VCS-Langmuir model with reaction rate constant $k_{-2,0}$ varied from the reference value $k^{\ominus}_{-2,0}$.

Variation of Storage Capacities

While the reaction rate constants strongly influence the steady state and dynamic behaviour, the storage parameters C^{AC}, c_{Pt} and c_{Ru} determine the time constants of the mass and charge balances, eq. 3.5-3.7. They are not influencing the steady state, but solely the dynamic behaviour, i.e. the EIS.
A variation of the double layer capacitance C^{AC} is shown in Fig. 3.9. Besides shifting the impedance to different frequencies (only visible in Bode plots), the shape of the EIS changes significantly. For high values of C^{AC}, the shape of the EIS is determined by the charge balance, since the mass balances reach the quasi-steady state faster than the charge balance. Therefore, the influence of the mass

balances on the EIS is diminished, and no pseudo-inductance is visible. On the other hand, decreasing C^{AC} leads to a pure interaction of the mass balance eqs. 3.5 and 3.6, since the charge balance is in a quasi-steady state. This is also indicated by the more pronounced pseudo-inductive behaviour. One can conclude, that using the reference parameter values, all three balances are influencing the EIS.

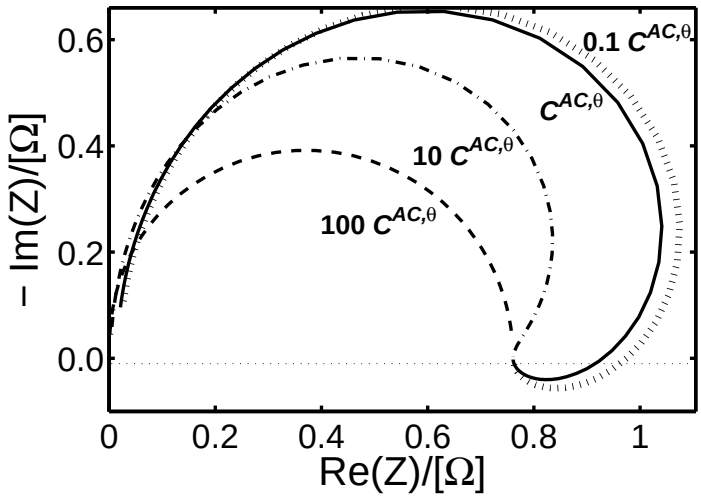

Figure 3.9: EIS of the VCS-Langmuir model: Electrochemical double layer capacitance C^{AC} varied from the reference value $C^{AC,\ominus}$.

Interpretation of a variation of the surface concentrations of Pt and Ru, c_{Pt} and c_{Ru} respectively, is more complex. Formally, the surface concentrations directly influence the reaction rate functions (eqs. 3.10-3.13), thus also the steady state behaviour. But, as mentioned in chapter 3.3.1, since it is not possible to separate the original reaction rate constants from the surface concentrations in steady state measurements, the reaction rate constants used here are the product of the underlying original reaction rate constants and surface concentrations, e.g. $k_{1,0} = \mathrm{const} = k_{1,orig} \cdot c_{\mathrm{Pt}}$. Changing c_{Pt} or c_{Ru} therefore implies an externally invisible change in the internal composition of the reaction rate constants, which neither has an influence on the EIS nor on the steady state. But, the given model formulation enables the definition of purely dynamic variables to study their influence on the EIS.
Results of a variation of c_{Pt} are shown in Fig. 3.10. An increase in Pt surface concentration leads to a much larger pseudo-inductive behaviour. This increase in c_{Pt} lowers the time constant of the $\mathrm{CO_{ads}}$ balance equation, eq. 3.5, which directly increases the dominant influence of reaction 1 and reaction 3 on the EIS.

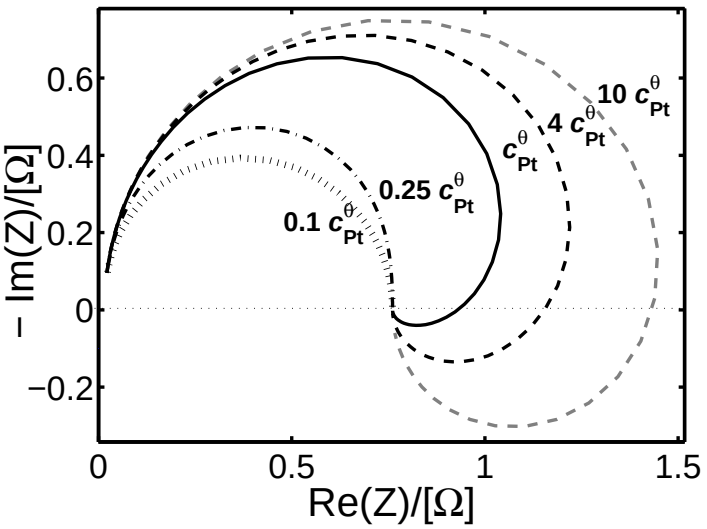

Figure 3.10: EIS of the VCS-Langmuir model: Platinum surface concentration c_{Pt} varied from the reference value $c_{\mathrm{Pt}}^{\ominus}$.

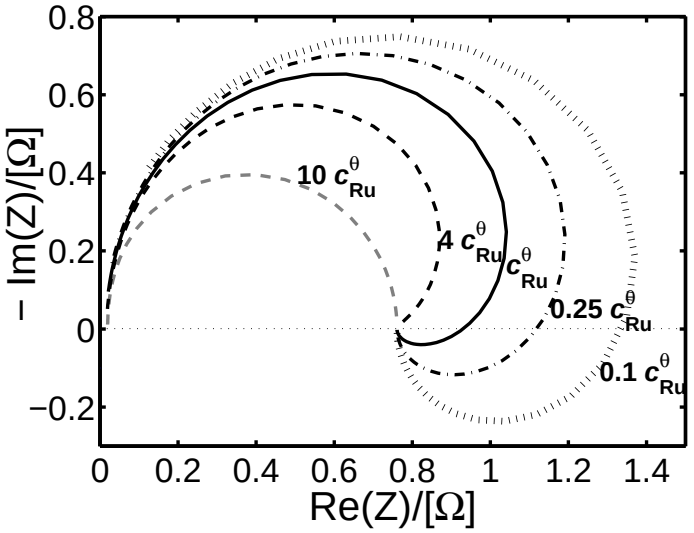

Figure 3.11: EIS of the VCS-Langmuir model: Ruthenium surface concentration c_{Ru} varied from the reference value $c_{\mathrm{Ru}}^{\ominus}$.

The opposite holds for a decrease in c_{Pt}, where reaction 2 will influence the EIS more strongly, and the pseudo-inductive behaviour disappears.
This conclusion is supported by Fig. 3.11, where variations of the Ru surface concentration are presented. Increasing c_{Ru} has the same effect as decreasing c_{Pt}, namely a diminished pseudo-inductive behaviour, while a decrease in c_{Ru} leads to a larger pseudo-inductive behaviour.

Since all storage constants influence the impedance spectra, and since the exact parameter values are not known, all of them are included in the quantitative fitting procedure, which is presented later.

Variation of the Inhomogeneity/Interaction Factors

Two of the four kinetic models contain a Frumkin/Temkin adsorption/desorption mechanism. The influence of this mechanism in comparison to the Langmuir adsorption/desorption is investigated in the following. The influence of the inhomogeneity/interaction factors g_{CO} and g_{OH} on the impedance spectra is shown in Fig. 3.12. It can be observed that an increase in g_{CO} inhibits the pseudo-inductive behaviour, while an increase in g_{OH} only increases the overall impedance. The variation of g_{CO} has a direct impact on the first and the third reaction step due to the exponential dependence of $k_1^{eff}(\theta_{\mathrm{CO}})$ and $k_3^{eff}(E, \theta_{\mathrm{CO}})$ on g_{CO}: In case of an increase of $k_1^{eff}(\theta_{\mathrm{CO}})$, $k_3^{eff}(E, \theta_{\mathrm{CO}})$ decreases, and vice versa. Hence, the inhomogeneity factor g_{CO} determines whether step 1 or 3 is the r.d.s.. The influence of g_{OH} is less pronounced, since this factor only influences the EIS via the surface coverage of OH, as do $k_{2,0}$ and $k_{-2,0}$.

Variation of Potential

A change of the potential strongly influences the effective reaction rate functions $k_i^{eff}(E, \theta_{\mathrm{CO}}, \theta_{\mathrm{OH}})$ of the reactions $i \in \{2, -2, 3\}$, and therefore shifts the relative influence of the single steps on the EIS.
This is illustrated in Fig. 3.13, where the simulated impedance spectra for $E = 0.44$ and $E = 0.37$ V are displayed in comparison to the reference impedance spectrum at $E = 0.41$ V. The differences are qualitative and quantitative: With increasing anode potential, the impedance spectra become smaller due to the higher effective reaction rate functions $k_2^{eff}(E)$ and $k_3^{eff}(E)$. Besides changes of the overall size of the spectrum, the change of the potential also shows a strong influence on the pseudo-inductive behaviour, as was to be expected. An increase of potential to $E = 0.44$ V leads to the loss of the pseudo-inductive behaviour. The explanation for this is the different dependences of the effective reaction rate functions $k_i^{eff}(E, \theta_{\mathrm{CO}}, \theta_{\mathrm{OH}})$ on the potential: While reaction 1 is potential independent, reaction 2 and reaction 3 depend on the potential. This leads to

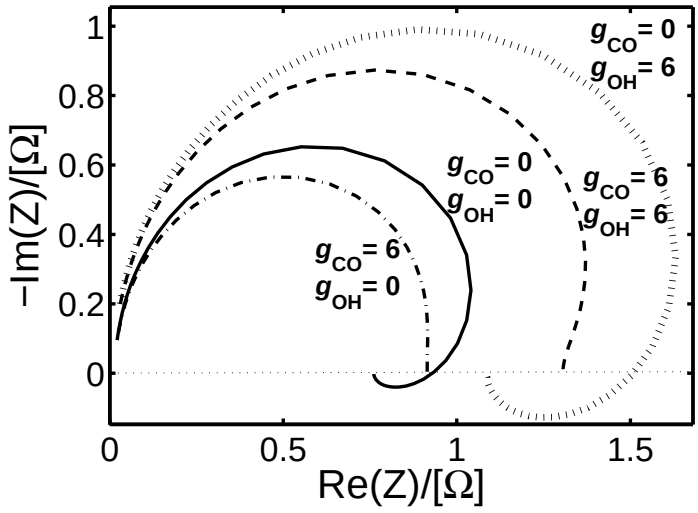

Figure 3.12: EIS of the VCS-Frumkin/Temkin model: Inhomogeneity/interaction factors g_{CO} and g_{OH} varied from the reference values of the VCS-Langmuir model ($g_{\mathrm{CO}} = 0, g_{\mathrm{OH}} = 0$).

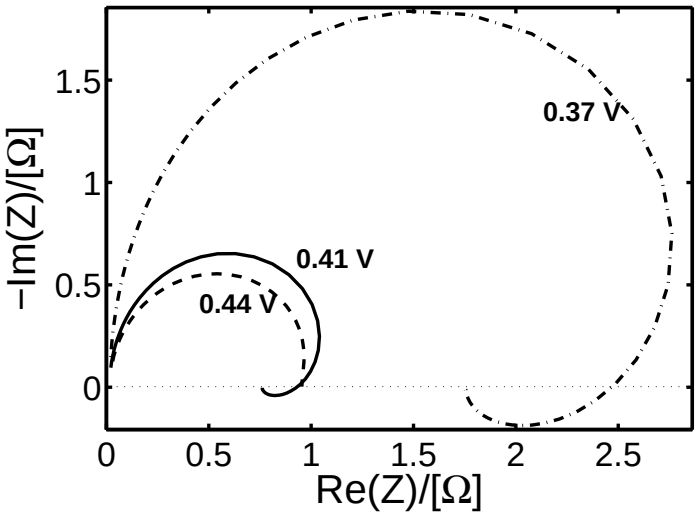

Figure 3.13: EIS of the VCS-Langmuir model: Electrochemical potential E varied from the reference potential (0.41 V).

a decrease in the relative influence of the latter steps in the EIS for increasing potentials.
Qualitatively similar findings were observed for the VCS-Frumkin/Temkin, Kauranen/Langmuir and Kauranen-Frumkin/Temkin kinetics. The latter two show an indirect potential dependence due to $\theta_{\mathrm{CO}}(E)$ and $\theta_{\mathrm{OH}}(E)$.

3.3.4 Quantitative Model Comparison

The previous section analysed the sensitivity of the simulated impedance spectra with respect to the reaction rate constants $k_{i,0}$ ($i \in \{1, 2, -2, 3\}$), to the storage parameters C^{AC}, c_{Pt} and c_{Ru}, to the quasi-steady state potential E and, in case of Frumkin/Temkin adsorption, to the inhomogeneity/interaction factors g_{CO} and g_{OH}. For each of the four models, this section presents a parameter set that yields the best agreement of the simulated to the experimental impedance data and steady state currents. A comparison of the results is used for identifying the most adequate model.
Since the EIS depends on the parameters mentioned above, all of them are optimised simultaneously. To include the potential dependence, a combined optimisation of the parameters to all three experimental EIS (i.e. at $E = 0.37$ V, $E = 0.41$ V and $E = 0.44$ V) is performed. As already shown (Fig. 3.5-3.13), the parameters are not linearily influencing the impedance spectra, and a variation in one parameter may annihilate the influence of the variation of others on the EIS. Since a local optimiser finds local minima, which in this case only yielded results with unacceptable agreement to the experiments, a global optimiser based on an evolutionary strategy was used. In the objective function, higher single weights were given to experimental points in the pseudo-inductive region, to emphasise the importance of this region in the EIS for the methanol oxidation kinetics. For a similar reason, frequency ranges where the electrode structure and the membrane properties determine the EIS shape ($f > 2$ Hz) were omitted for the parameter identification.

Table 3.1: Results of the global parameter identification for all four kinetic models

Parameter	VCS-Langm.	VCS-Frumk./T.	Kaur.-Langm.	Kaur.-Frumk./T.
$10^6\ k_{1,0}$/m s^{-1}	1.48	1.54	0.87	1.15
$10^5\ k_{2,0}$/mol m^{-2} s^{-1}	6.11	1.59	6.26	54.4
$k_{-2,0}$/mol m^{-2} s^{-1}	25.3	6.78	98200	21800
$10^6\ k_{3,0}$/mol m^{-2} s^{-1}	0.515	0.545	649000	10400
C^{AC}/F m^{-2}	8690	6350	18100	9040
$10^2\ c_{\mathrm{Pt}}$/mol m^{-2}	7.75	8.82	7.21	9.57
$10^2\ c_{\mathrm{Ru}}$/ mol m^{-2}	4.32	9.3	1.2	4.83
g_{CO}	-	0.293	-	3.72
g_{OH}	-	2.08	-	0.408

Fig. 3.2 shows the EIS optimisation result of the VCS-Langmuir model (lines) in comparison to the experimental EIS (concatenated symbols). The respective parameter values are given in Table 3.1. All simulated curves show a pseudo-inductive behaviour, but, in contrast to the experimental EIS, this behaviour is not increasing with decreasing anode potential. Furthermore, the dependence of the absolute values of the simulated impedance spectra on potential is smaller than in the experiments. This is best illustrated in the comparison of the simulated EIS at $E = 0.44$ V and $E = 0.41$ V. The simulation results are very similar and even intersect at low frequencies. Considering all points mentioned above, a quantitative representation of the experimental EIS with the VCS-Langmuir model is not possible.

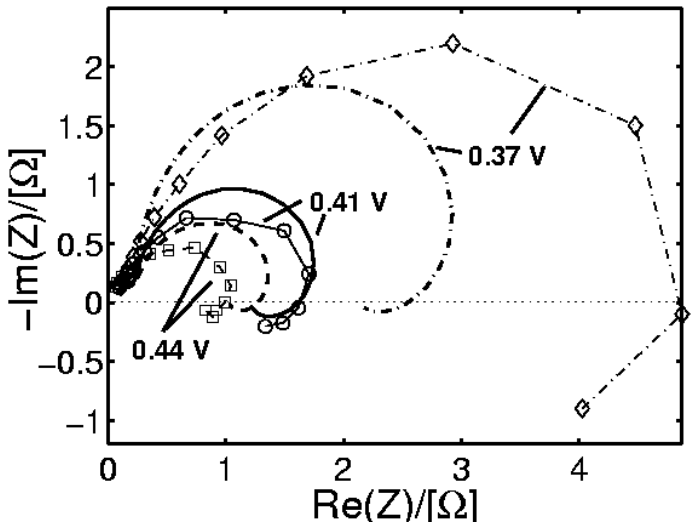

Figure 3.14: Simulated EIS (solid lines) of the VCS-Frumkin/Temkin model with optimised parameters (values see Table 3.1) vs. experimental EIS (concatenated symbols) at three potentials.

The optimisation result of the VCS-model with Frumkin/Temkin adsorption is displayed in Fig. 3.14 (parameter values see Table 3.1). For this model, similar findings and conclusions hold as for the VCS-Langmuir model: All curves show pseudo-inductive behaviour, but the dependences both of the absolute impedance values of the EIS and of the pseudo-inductive behaviour on potential diverge from that of the experiments. Nonetheless, the potential dependence of the overall impedance is slightly more realistic. This effect should be attributed to the exponential dependence of the reaction rates on the surface coverages of CO_{ads} and OH_{ads}.

In contrast to the VCS kinetic models, both Kauranen kinetic models show a better agreement of experiment and simulation with regard to potential dependence. Fig. 3.15 shows the impedance spectra of the Kauranen-Langmuir model (parameter values see Table 3.1). The EIS at 0.41 V and 0.37 V represent the experimental EIS much better than both VCS-models. Nonetheless, the EIS at 0.44 V shows no pseudo-inductance, which can be attributed to the occurance of an r.d.s.. Since a loss of the pseudo-inductive behaviour at high anode potentials was not reported in the literature for methanol oxidation experiments, this model would not give a good approximation of the real dynamic behaviour at high potentials.

Compared to the former model, the Kauranen-Frumkin/Temkin kinetic model yields pseudo-inductive behaviour at all potentials. This is seen in the spectra presented in Fig. 3.16 (parameter values see Table 3.1). Like in the experiments, the pseudo-inductance becomes more pronounced with decreasing potential. Furthermore, the model exhibits the most realistic potential dependence of the EIS. Finally, compared to the other kinetic descriptions, the Kauranen-Frumkin/Temkin kinetics shows the best accordance of simulated and experimental data. It is therefore accepted as a reaction kinetics which quantitatively predicts the experimentally observed behaviour of methanol oxidation.

A comparison of the parameters of all model variants in Table 3.1 shows a relatively stable $k_{1,0}$. $k_{3,0}$ is similarly large for the VCS models, but much larger for the Kauranen models. In the contemplated potential region, this yields similarly large $k_1^{eff}(\theta_{\mathrm{CO}}) \cdot c^{AC}_{\mathrm{CH_3OH}}$ and $k_3^{eff}(E, \theta_{\mathrm{CO}})$ for the VCS models, whereas for the Kauranen models, $k_1^{eff}(\theta_{\mathrm{CO}}) \cdot c^{AC}_{\mathrm{CH_3OH}}$ is much smaller than $k_3^{eff}(\theta_{\mathrm{CO}})$:

VCS models:	$0.65 \leq k_1^{eff}(\theta_{\mathrm{CO}}) \cdot c^{AC}_{\mathrm{CH_3OH}} \,/k_3^{eff}(E, \theta_{\mathrm{CO}}) \leq 4.28$
Kauranen models:	$k_1^{eff}(\theta_{\mathrm{CO}}) \cdot c^{AC}_{\mathrm{CH_3OH}} \,/k_3^{eff}(\theta_{\mathrm{CO}}) \leq 0.12$

This suggests that the first reaction step is rate determining in the Kauranen models and would therefore contradict the interpretation of the pseudo-inductive behaviour. Analysis disproves such interpretation: The equilibrium of the second reaction step in the Kauranen models is strongly shifted towards the reactants, causing a lower OH surface coverage (≤ 0.15). As a result, reaction step 3 is slowed down.

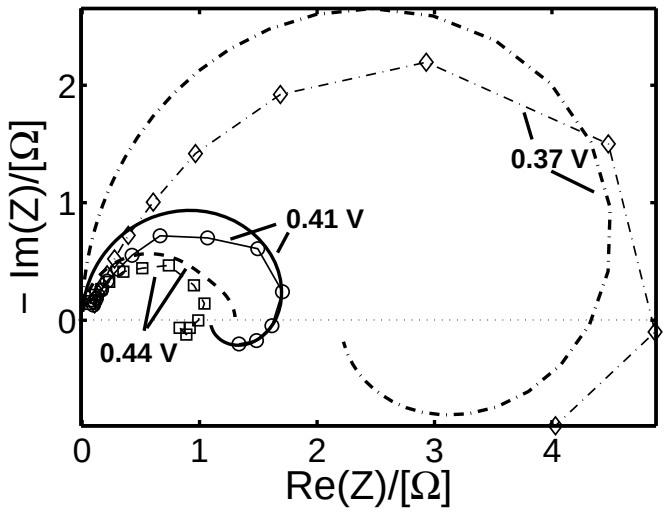

Figure 3.15: Simulated EIS (lines) of the Kauranen-Langmuir model with optimised parameters (values see Table 3.1) vs. experimental EIS (concatenated symbols) at three potentials.

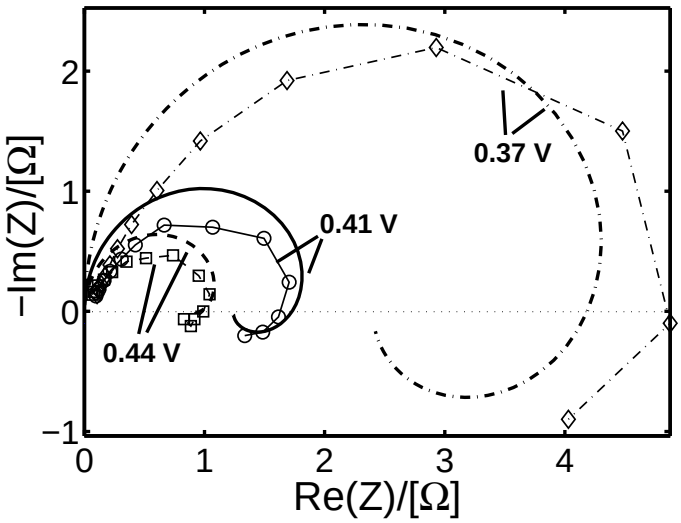

Figure 3.16: Simulated EIS (lines) of the Kauranen-Frumkin/Temkin model with optimised parameters (values see Table 3.1) vs. experimental EIS (symbols) at three potentials.

3.4 Anode Kinetics and Dynamic DMFC Behaviour

Chapter 2 has shown the dominant influence of the reaction kinetics on the overall dynamic behaviour of DMFCs. The identification of a quantitative anode kinetics which is valid for steady state as well as dynamic operating conditions therefore motivated the research being presented in this chapter. In section 3.3.4, such a kinetic description could be identified: The presented Kauranen-Frumkin/Temkin methanol oxidation reaction kinetics can quantitatively predict the steady state and dynamic methanol oxidation experiments conducted on a DMFC anode. To investigate the influence of this kinetics on the simulation results of a complete DMFC model, it is integrated into the 2x-DMFC model presented in chapter 2.

The complete set of equations of this new DMFC model is:

$$\frac{dc^{AC}_{\mathrm{CH_3OH}}}{dt} = \frac{k^{AD}A_S}{V^{AC}}(c^{A}_{\mathrm{CH_3OH}} - c^{AC}_{\mathrm{CH_3OH}}) - \frac{A_S}{V^{AC}}n^{M}_{\mathrm{CH_3OH}} - \frac{A_S}{V^{AC}}r_{A1} \tag{3.18}$$

$$\frac{d\theta_{\mathrm{CO}}}{dt} = \frac{1}{c_{\mathrm{Pt}}}(r_{A1} - r_{A3}) \tag{3.19}$$

$$\frac{d\theta_{\mathrm{OH}}}{dt} = \frac{1}{c_{\mathrm{Ru}}}(r_{A2} - r_{A3}) \tag{3.20}$$

$$\frac{d\eta_A}{dt} = 0 = \frac{1}{C^{AC}}i_{cell} + \frac{1}{C^{AC}}(-4Fr_{A1} - Fr_{A2} - Fr_{A3}) \tag{3.21}$$

$$\frac{d\eta_C}{dt} = 0 = -\frac{1}{C^{CC}}i_{cell} - \frac{1}{C^{CC}}\ 6Fr_C - \frac{1}{C^{CC}}\ 6Fn^{M}_{\mathrm{CH_3OH}} \tag{3.22}$$

$$r_{A1} = r_{A10}\cdot\exp\left[-\beta_{\mathrm{CO}}g_{\mathrm{CO}}(\theta_{\mathrm{CO}} - 0.5)\right]\cdot c^{AC}_{\mathrm{CH_3OH}}\cdot(1-\theta_{\mathrm{CO}}) \tag{3.23}$$

$$\begin{aligned} r_{A2} = {} & r_{A20}\cdot\exp\left[\frac{\alpha_A F}{RT}\eta_A\right]\cdot\exp\left[-\beta_{\mathrm{OH}}g_{\mathrm{OH}}(\theta_{\mathrm{OH}} - 0.5)\right](1-\theta_{\mathrm{OH}}) \\ & -r_{A-20}\cdot\exp\left[-\frac{(1-\alpha_A)F}{RT}\eta_A\right]\cdot\exp\left[(1-\beta_{\mathrm{OH}})g_{\mathrm{OH}}(\theta_{\mathrm{OH}} - 0.5)\right]\theta_{\mathrm{OH}} \end{aligned} \tag{3.24}$$

$$r_{A3} = r_{A30}\cdot\exp\left[(1-\beta_{\mathrm{CO}})g_{\mathrm{CO}}(\theta_{\mathrm{CO}} - 0.5)\right]\theta_{\mathrm{CO}}\cdot\theta_{\mathrm{OH}} \tag{3.25}$$

$$r_C = -r_{C0}\ exp\left[\frac{-(1-\alpha_C)F}{RT}\eta_C\right] \tag{3.26}$$

$$n^{M}_{\mathrm{CH_3OH}} = \frac{D^{M}_{\mathrm{CH_3OH}}}{d^M}\ c^{AC}_{\mathrm{CH_3OH}} \tag{3.27}$$

$$U_{cell} = U^{\theta}_0 - \eta_A + \eta_C - \frac{d^M}{\kappa^M}i_{cell} \tag{3.28}$$

To transfer the reaction rate constants from the kinetic model to the nomenclature of the DMFC model, the following parameter redefinition is done:
$r_{A10} = k_{1,0}$, $r_{A20} = k_{2,0}$, $r_{A-20} = k_{-2,0}$, and $r_{A30} = k_{3,0}$.

Values for the geometry, transport and cathode kinetic parameters, A_S, V^{AC}, d^M, k^{AD}, κ^M, α_C and U_0^θ, are taken from the 2x-model (values see Appendix B.2). In all simulations, r_{C0} is adjusted in a final step to fit the model to experimental polarisation curves.
As a first test, the anode kinetic parameter values obtained from the Kauranen-Frumkin/Temkin kinetics fit (see Table 3.1) are directly inserted into the model. These parameters show the basic influence of the refined reaction kinetics on the DMFC response, but due to different system set-ups the parameters obtained from the cyclone flow cell (CFC) are not identical to those of the DMFC. Although both systems contain a MEA of the same construction type, the following differences make a correction of the kinetic parameters necessary:

- Contact quality between anode catalyst layer and diffusion layer:
  DMFC: homogeneous pressure distribution due to ribs as pressure distributors;
  CFC: inhomogeneous pressure distribution, pressure applied to outer edges

- Ratio of active area exposed to methanol to total active area:
  DMFC: =1; CFC: = 0.17

- Additional substances transported through the membrane:
  DMFC: traces of oxygen; CFC: traces of sulfuric acid

- History of anode catalyst treatment, including possible restructuring and oxidation of catalyst (resulting e.g. in a change in Ru-oxide content).

Fig. 3.17 shows the experimental and simulated cell voltage responses to the standard cell current density step of 520 A/m^2 to 260 A/m^2 (with $r_{C0} = 2.5 \times 10^{-5}$ mol/m^2/s). Simulations were done using the set of nonlinear equations (eqs. 3.18-3.28), as well as the set of linearised equations (identical to a transfer function model). No overshoot is visible using the linearised model (dashed line), whereas the nonlinear model (dash-dotted line) produces an absolute overshoot of 43 mV, which is much closer to the experimentally observed cell voltage overshoot of $\approx$ 20 mV, than the overshoots of up to only 2 mV obtained from all other models presented in section 2.3. The Kauranen-Frumkin/Temkin kinetics therefore is a key contribution to predict correctly the dynamic behaviour of the DMFC. The difference between the response of the linearised version and the nonlinear version of the DMFC model also shows its high nonlinearity: Neglecting nonlinearity, e.g. as in transfer function models, produces an entirely different system

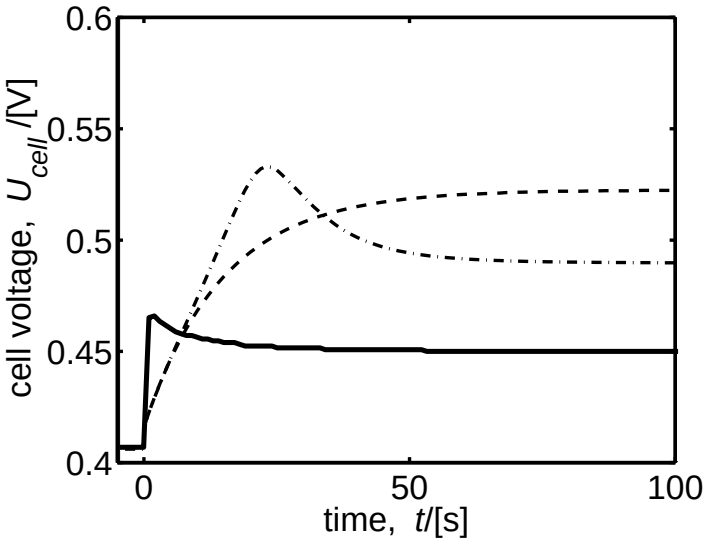

Figure 3.17: Cell voltage response to standard cell current density step from 520 A/m^2 to 260 A/m^2: Experiment (solid), response of non-linear model (dash-dotted), response of linearised model (dashed).

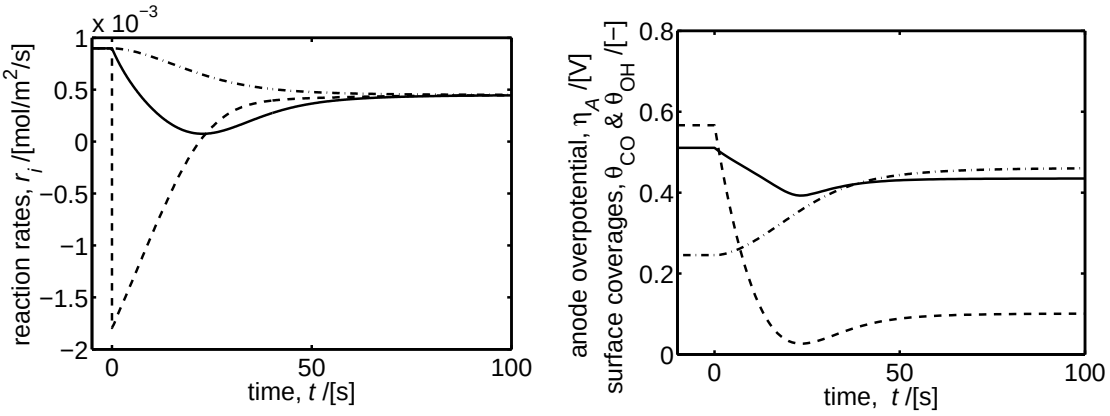

Figure 3.18: Response of the nonlinear model to the standard cell current density step from 520 A/m^2 to 260 A/m^2. Left: Reaction rate r_{A1} (dash-dotted), reaction rate r_{A2} (dashed), reaction rate r_{A3} (solid). Right: Anode overpotential (solid), OH surface coverage (dashed) and CO surface coverage (dash-dotted).

response. Due to the strong nonlinearity of the DMFC model with the Kauranen-Frumkin/Temkin kinetics, transfer function models are of no further use for analysing the DMFC dynamics with this presented model. All further simulations therefore use nonlinear models.

The observed pronounced dynamic behaviour should be attributed to the interaction of the fast chemisorption of water and the slow oxidation reactions of methanol and CO. This is also illustrated in Fig. 3.18, where the single reaction rates are displayed to the left, and the OH (dashed) and CO (dash-dotted) surface coverage response and the anode overpotential (solid) are displayed to the right. In consequence of the quasi-steady state anode charge balance (eq. 3.21), a sudden decrease in cell current at t=0 causes an instantaneous drop of the fastest reaction rate, i.e. of r_{A2}. This leads to a decrease in OH surface coverage and the reaction rate r_{A3}. The consumption of CO is reduced and the CO coverage slowly increases. This in turn decreases the reaction rate r_{A1}, and the drop of r_{A3} and the OH coverage is slowed down, showing a negative overshoot. Since the OH surface coverage is directly coupled to the anode overpotential via reaction step 2, the anode overpotential, and the cell voltage shows overshooting.

A comparison of the cell voltage response of the non-linear model to the experimental response shows that the absolute overshoot as well as the new steady state of the simulation are higher than those of the experiment. Furthermore, the experimental cell voltage responds faster than the simulated one. A major reason for these deviations is the transition from the cyclone flow cell set-up, for which the parameters were identified, to the DMFC (discussion see above).
The methanol kinetic parameters are adjusted in the following to fit the experimental cell voltage response displayed in Fig. 3.17. To guarantee that reaction steps 1 and 3 are equally fast (condition for pseudo-inductance), the original kinetic values, r_{A10} and r_{A30} are multiplied with a similar factor. Water adsorption is still regarded to be in a quasi-equilibrium with the same ratio (r_{A20}/r_{A-20}). The kinetic parameter values in Table 3.2 have been found to adequately describe the experimental cell voltage response as well as the polarisation curve, as illustrated in Fig. 3.19. The figures show a reasonable agreement of experiment and simulation.
It can be concluded that the DMFC model presented in eqs. 3.18-3.28, combining validated anode kinetics with the dynamic model introduced in chapter 2, is able to quantitatively predict the dynamic behaviour of DMFCs with constant methanol concentration in the anode compartment. Chapter 5 will provide an in-depth analysis of the underlying phenomena and dependences within the model, highlighting in addition the influence of the methanol concentration distribution inside the anode flow field on the dynamic response.

Table 3.2: Original and corrected (fitted) anode and cathode kinetics parameters of the DMFC model with Kauranen-Frumkin/Temkin kinetics.

	r_{A10} $\frac{\text{m}}{\text{s}}$	r_{A20} $\frac{\text{mol}}{\text{m}^2\text{s}}$	r_{A-20} $\frac{\text{mol}}{\text{m}^2\text{s}}$	r_{A30} $\frac{\text{mol}}{\text{m}^2\text{s}}$	g_{CO} -	g_{OH} -	c_{Pt} $\frac{\text{mol}}{\text{m}^2}$	c_{Ru} $\frac{\text{mol}}{\text{m}^2}$	r_{C10} $\frac{\text{mol}}{\text{m}^2\text{s}}$
orig.	1.15×10^{-6}	5.44×10^{-4}	2.18×10^{4}	0.01	3.72	0.41	0.096	0.048	2.5×10^{-5}
fit	5.69×10^{-6}	5.44×10^{-4}	2.18×10^{4}	0.03	5.11	0.43	0.015	0.128	5.75×10^{-6}

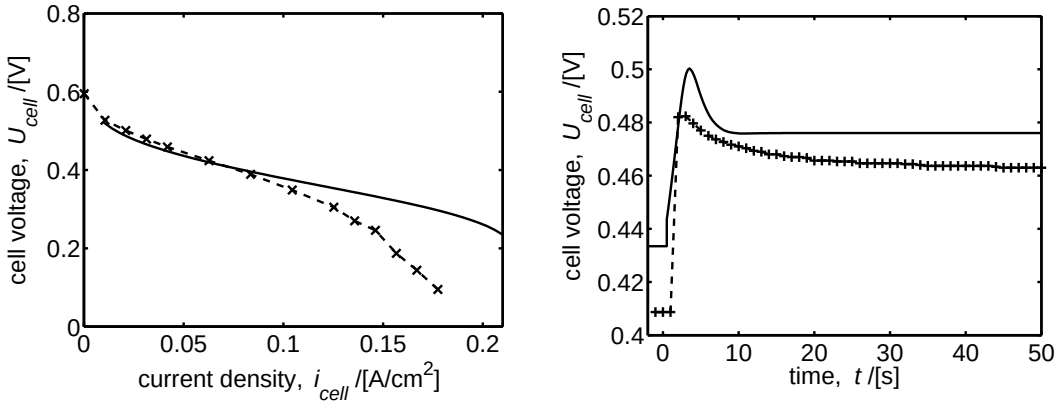

Figure 3.19: Polarisation curve (l.h.s.) and cell voltage response to standard cell current density step from 520 A/m^2 to 260 A/m^2 (r.h.s.): Experiment (concatenated symbols), response of DMFC model with parameters from Table 3.2 (solid line).

3.5 Concluding Remarks on the Methanol Oxidation Analysis

This chapter presented an analysis of the methanol oxidation kinetics at a DMFC anode. Four different kinetic descriptions for the methanol oxidation were formulated. They differed in the adsorption/desorption mechanisms, as well as in the potential dependence of the methanol adsorption step. Since all kinetic models could quantitatively describe the experimental steady state behaviour, dynamic measurements, here electrochemical impedance spectroscopy (EIS), were used to identify the most adequate model.

EIS of the four kinetic descriptions were modelled by using their balance equations and rate equations that were previously transformed into the frequency domain. Analysis of the dependence of the modelled impedance spectra on reaction kinetic parameters showed a narrow range at which pseudo-inductive behaviour, a distinctive feature of the experimental EIS, could be observed: At least two consecutive steps with similar dynamic reaction rates are necessary. In the presented

models, these steps were methanol partial oxidation and subsequent oxidation of an adsorbed methanol intermediate. Water chemisorption on Ru, as a further reaction step parallel to methanol partial oxidation, was in quasi equilibrium and influenced the EIS via the water intermediate's surface coverage. Parameter variation revealed an additional strong influence of the storage parameters and potential on the impedance spectra.
For all four kinetic descriptions, optimum model parameters were identified. Comparison of the simulated EIS to experiments showed that the Kauranen-Frumkin/Temkin kinetics is the model with the best quantitative description of the steady state and dynamic behaviour of electrochemical methanol oxidation.
Finally, the identified kinetics was inserted in the 2x-DMFC model of chapter 2. Compared to the models from chapter 2, this new combined model was in good agreement to the experimentally observed transient cell voltage response. Parameter values from EIS optimisation produced overshoot heights similar to experimental ones, and slightly modified kinetic parameters were able to describe the dynamic behaviour of the DMFC to a step-wise change of cell current density. The presented model is applicable for the activation controlled and quasi-linear regions of the current-voltage curve of DMFCs with constant methanol concentration in the anode compartment.
A further, more detailed analysis of the underlying phenomena and dependences within the model is given in chapter 5. In addition, the influence of methanol concentration distribution inside anode flow fields on the dynamic response will be characterised.

Chapter 4

Hydrodynamic Characterisation of Anode Flow Fields

4.1 Introduction

The previous two chapters investigated the basic phenomena governing the dynamic DMFC behaviour, especially the influence of the anode methanol oxidation kinetics on the dynamic response. The presented model is valid in the activation controlled and quasi-linear regions of the polarisation curve of DMFCs. It assumes a homogeneous methanol distribution over the anode flow field, i.e. over the active surface area. The latter assumption is valid for negligible methanol residence time inside the anode compartment, which is equivalent to high anode volume flow rates. High volumetric flow rates in turn leads to high energy consumption by the anode feed pump and thus to a decreased system efficiency. Therefore, e.g. for portable applications, low volumetric flow rates are preferred. Low anode volume flow rates can lead to inhomogeneous distribution of methanol within the anode compartment, i.e. to non-uniform system states within the active area. This affects the overall steady-state and dynamic behaviour of DMFCs. It is a general objective to distribute the fuel all over the active area so that methanol supply to the reaction zone is sufficient. Furthermore, in case of concentration changes in the methanol feed, this concentration should be spread over the various zones evenly in time and space. For efficient utilisation of fuel and catalyst, as well as for improved steady-state and dynamic fuel cell performance, the flow distribution inside anode compartments has to be optimised.

Several research groups investigated anode flow characteristics, e.g. by volumetric flow rate variation [63], carbon dioxide monitoring [3] or flow field characterisation. Various flow field designs for liquid DMFCs are reported in the literature, e.g. parallel channel designs [1, 3, 6, 60, 63], parallel channel designs with triangular inlet and outlet zones [3, 6, 61], spot designs [27, 60], meander designs [21] and

mesh designs [59]. Arico et al. recently investigated an optimal flow field design for vapour fed DMFCs [7]. They found that flow field design has a non-negligible influence on mass transfer characteristics, including methanol crossover. Several other studies compared different compartment designs with respect to their influence on the electrochemical cell performance, on the carbon dioxide transport and with regard to practical considerations: Amphlett et al. showed that for a parallel channel design, the channel depth directly influences the cell performance [1]. Scott and colleagues [3, 60, 61] examined various flow field designs and their effect on the carbon dioxide transport. Furthermore, in [59] a comparison of stainless steel mesh flow fields of different mesh sizes with parallel and spot designs respectively, was presented, indicating that mesh designs may be a cost-reducing alternative. The same authors discussed gains and drawbacks of the spot design [60]. Further publications from this group present a parallel channel design with triangular inlet and outlet zones, based on a heat exchanger design concept. It showed a more uniform flow than the simple parallel channel design [3, 61].
It can be summarised that the criteria for an optimal flow field are manifold. The design performance depends on operating conditions like temperature and pressure, which determine the state of the fluid and also carbon dioxide transport phenomena. Therefore, an optimal design depends on operating conditions.

To analyse and predict the influence of flow fields on the cell performance, DMFC models which also take into account the methanol distribution within the flow fields are essential. Computational fluid dynamics (CFD) techniques have shown to be a powerful tool when studying flow and transport phenomena inside fuel cells. Some research work has been done on CFD simulation of different fuel cells, for example phosphotungstic acid fuel cells (PWAFC) [44], molten carbonate fuel cells (MCFC) [30] and PEMFCs [18].
In a previous work [42], the residence time behaviour and concentration distribution in a simplified rhomboidal DMFC anode flow field was studied by 3D numerical flow simulations and by experimental measurements. Simulations with the software CFX, based on the Finite Volume Method, and the software MooNMD, based on Finite Element Method, showed similar results and the reliability of the computed residence time distributions (RTD) was proven by showing that they depended only slightly on the parameters of the numerical schemes applied. Experimentally obtained RTD results were in good agreement with the numerical simulations. The obtained results provided evidence of weaknesses of the flow field design. Nonetheless, these studies were pure flow field characterisation studies. Using such CFD approaches for complete DMFC modelling, including multi-step reaction mechanisms, leads to highly complex descriptions which are time-consuming with respect to setup and simulation and may lead to instable or intractable models. Furthermore, such models are not applicable for dynamic simulations and control.

Reduced models seem to be more promising, especially when focussing on dynamic aspects: Instead of simulating flow fields microscopically, macroscopic models, containing e.g. ideal reactor networks, can be used, as will be shown.

This chapter presents the development of reduced hydrodynamic models of anode flow fields. To study their influence on the steady state and dynamic DMFC behaviour, the hydrodynamic models are then integrated into complete DMFC models (chapter 5).
The investigated anode flow fields are presented in section 4.2. They are hydrodynamically characterised using residence time distribution and concentration distribution measurements (section 4.3). The experiments are compared to models consisting of ideal reactor networks, which prove suitable for quantitatively describing the observed hydrodynamic behaviour of the flow fields (section 4.4).

4.2 Investigated Anode Flow Fields

Of the flow field designs mentioned in the previous section, the ones most frequently used for liquid-fed DMFCs are the parallel channel design, the spot design and the rhomboidal design (parallel channel design with triangular inlet and outlet). In this chapter, DMFCs with these three flow field types are presented and their hydrodynamic behaviour is experimentally and theoretically analysed.

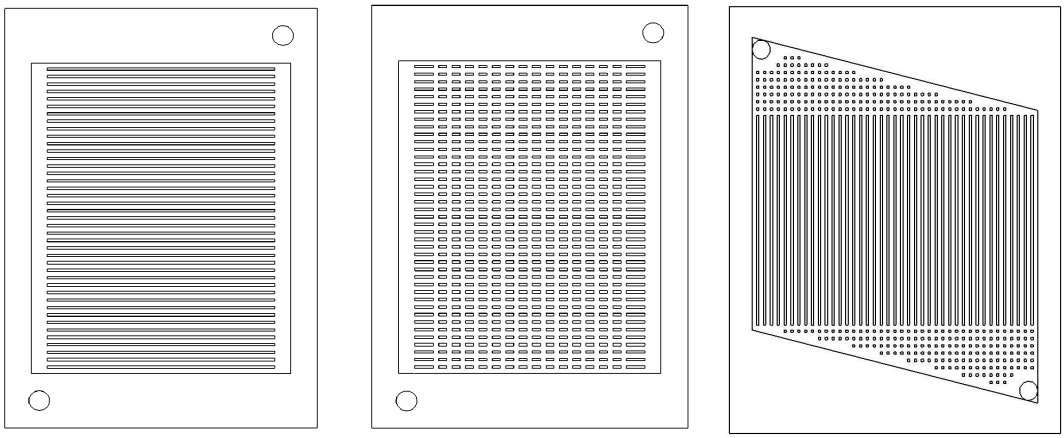

Figure 4.1: CAD drawings of the investigated flow field designs: Parallel channel design (left), spot design (middle) and rhomboidal design (right).

Fig. 4.1 shows the three flow field designs. The parallel channel design and the rhomboidal design both feature the same active area geometry: 42 channels of width 2 mm, separated by 1 mm wide ribs. For the spot design, the parallel channel design is modified by using interlaced ribs: every 3 mm a gap of 2 mm

length is machined into the ribs. As a result, the spot design enables a flow in horizontal and vertical direction, while the flow in the parallel channel design's active area geometry can only proceed horizontally. In all three designs, the active area has the outer dimensions 86 mm x 125 mm, and the flow field depth is 2 mm.
Parallel channel design and spot design both feature an inlet distributor channel and a collector channel of 6 mm width, which are used to supply the active area geometry with fuel. In the rhomboidal design, the distributor and collector area has a triangular shape with cuboids of 1 mm width and length. This should guarantee a more homogeneous flow distribution to the single channels.

4.3 Experimental

Residence time measurements of and concentration distribution monitoring in the three introduced flow fields are presented in the following. To enable optical surveillance of concentration fronts, the experiments have been conducted in transparent cells manufactured from polyacrylics. The cells consist of two elements: the flow field design and a cover plate.

4.3.1 Basic Considerations

In the studies of Scott, Sundmacher and colleagues [62, 63, 68, 78], a frequently used volumetric flow rate with the cells presented in [62] is 1.36 ml/min. This corresponds to a very low Reynolds number of $Re = 1.32$ inside the channels. A further measure to compare volumetric flow rates in anode compartments of DMFCs is the specific volumetric flow rate, i.e. volumetric flow rate per active area. Table 4.1 gives a literature survey of these parameters. A suitable range for usual applications seems to be $0.1-0.8$ ml/(cm^2 min), while volumetric flow rates between $0.1 - 0.2$ ml/(cm^2 min) are more frequently used. The volumetric flow rate approximation via the Reynolds number suggests a flow rate of 6 ml/min for the presented parallel and rhomboidal channel design, and the specific volumetric flow rate approximation a flow rate of 10 to 20 ml/min. The purely hydrodynamic investigations presented in the following were conducted at 5, 10 and 15 ml/min, which is close to both measures.

4.3.2 Setup

In order to investigate the hydrodynamic behaviour of the flow fields, a setup according to Figure 4.2 was designed. Two pressure vessels, operating pressure 0.2 MPa abs., caused the driving force which moved the fluid through the cell. By this, pulsation due to pumps was avoided. The volumetric flow rate was adjusted via rotameters and additionally monitored via a balance, collecting the efflux

Table 4.1: Literature survey: Volumetric flow rates per area for liquid fed DMFCs

source	flow rate ml/min	area cm^2	specific flow rate $ml/(cm^2 min)$
[52]	0.3	1	0.3
[60]	0.84 - 6.96	9	0.093 - 0.773
[62]	0.84, 1.36	9	0.093, 0.151
[73]	1	9	0.11
[68, 78]	1.36	9	0.151
[63]	1.36, 2	9	0.151, 0.222
[36]	4	25	0.16
[32]	5	25	0.2
[22]	10	30	0.33
[64]	15	25	0.6
[27]	20	25	0.8
[69]	640	100	6.4

from the cell. The applied technique for measuring concentrations was UV-Vis spectroscopy, Specord 50, Analytik Jena. The online testing probe was installed at the outlet of the cell. As a tracer substance, eosin (Basacid Rot 316, BASF) with maximum absorbance at a wavelength of $\lambda_{max} = 515$ nm was selected. After recording a calibration curve at this wavelength (Appendix A.1), a concentration range from 0 to $5.5 \cdot 10^{-6}$ mol/l was determined, in which the Lambert-Beer law is valid. Consequently, a tracer concentration of $5 \cdot 10^{-6}$ mol/l was used in the experiments. Ageing tests were conducted to verify that the solution is stable for at least three hours (maximum relative error = 3.68%, see Appendix A.1). A three-way cock was used to switch from deionised water to eosin solution, causing a concentration step at the inlet of the investigated cell. To minimise the influence of the pipes connecting the cock with the cells, and the pipes connecting the cells with the online probe, their volume, and hence their diameter, was minimised (see section 4.4.1). Since these pipes constitute 15.1 - 17.5 % of the whole tested equipment, their influence is not negligible in the interpretation and simulation of the obtained results.

4.3.3 Residence Time Distribution

The cumulative residence time distribution (RTD) measurements were conducted at 15 ml/min, at 10 ml/min and at 5 ml/min. The recorded curves show a stable behaviour and are highly reproducible: for every single measurement, the absolute deviation between the single RTD and the arithmetic mean is $\leq 1\%$.

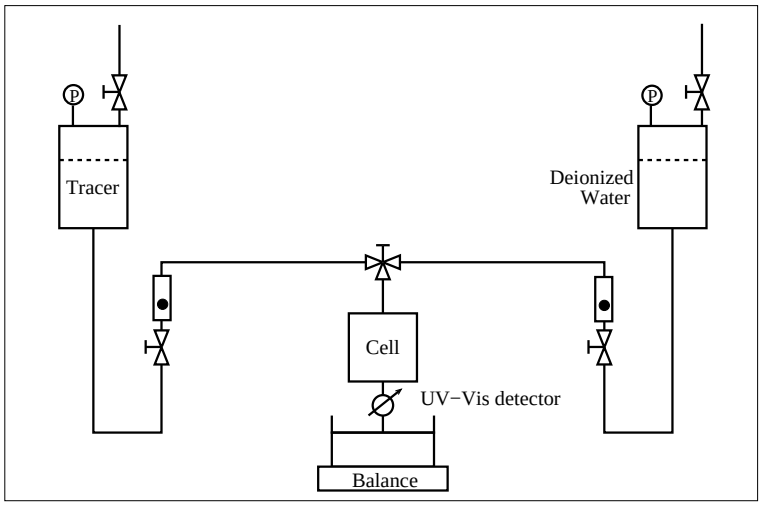

Figure 4.2: Residence time measuring device

Fig. 4.3 (l.h.s.) shows the mean RTD curves of the parallel channel design for the three volumetric flow rates. In Fig. 4.3 (r.h.s.), these curves are plotted in terms of the dimensionless time

$$\theta = t/\tau, \tag{4.1}$$

where t is the time and τ is the mean residence time

$$\tau = \frac{\text{volume of cell } + \text{ volume of connecting pipes}}{\text{volumeric flow rate}} \tag{4.2}$$

As can be seen, the dimensionless RTD curves for the three volumetric flow rates are quite similar. This indicates that the flow pattern through the parallel channel design depends only slightly on the flow rate in the contemplated volumetric flow rate region. The first tracer molecules are detected after $\theta = 0.4$, and 50% of the molecules inserted at $t = 0$ s have left the cell at θ_{50}=0.8.

In Fig. 4.4, the mean cumulative residence time curves of the spot design are given vs. time (l.h.s.) and vs. dimensionless time (r.h.s.). The dimensionless RTD curves for the three volumetric flow rates are very similar, suggesting a stable flow profile for the different volumetric flow rates. In contrast to the parallel channel design, in this design the first molecules reached the outlet later ($\theta = 0.6$), and the curves show a steeper slope: the time to reach F=0.5 is ($\theta_{50} = 0.9$) − 0.6 = 0.3, which is smaller than in the parallel channel design (=0.4). This should be interpreted as a more compact concentration front within the spot design.

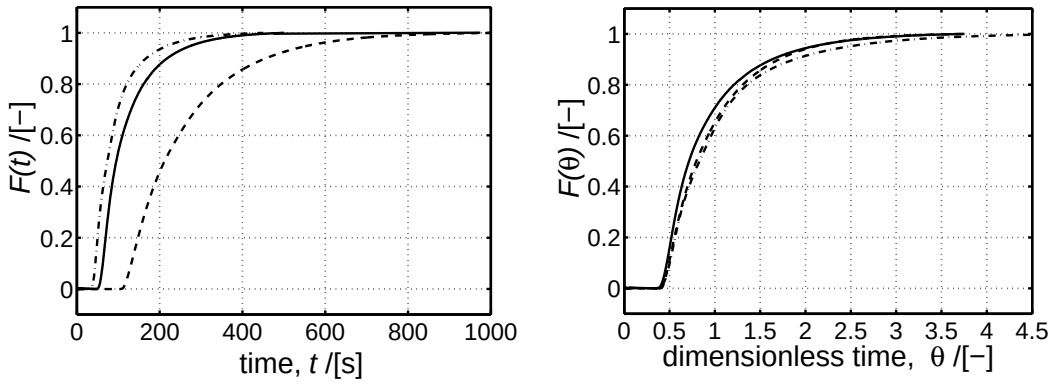

Figure 4.3: Experimental cumulative residence time distribution curves of the parallel channel design at 5 ml/min (dashed line), 10 ml/min (solid line) and 15 ml/min (dash-dotted line). Left: Plot vs. time t. Right: Plot vs. dimensionless time θ.

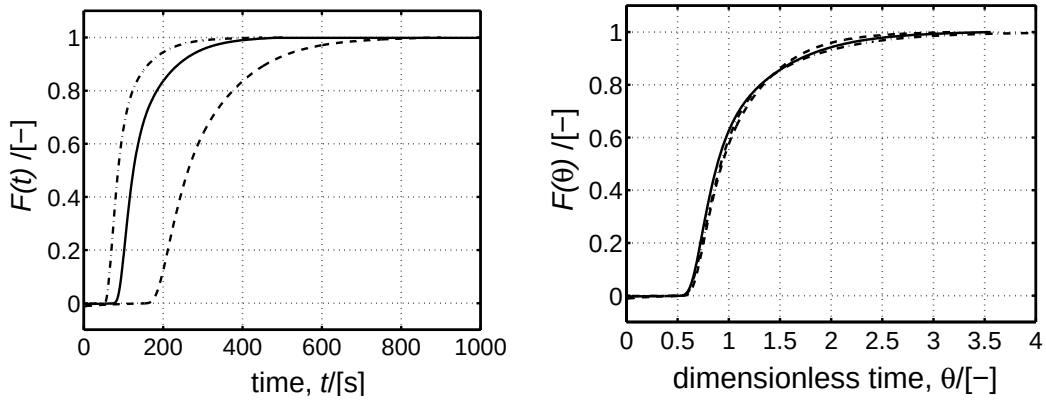

Figure 4.4: Experimental cumulative residence time distribution curves of the spot design at 5 ml/min (dashed line), 10 ml/min (solid line) and 15 ml/min (dash-dotted line). Left: Plot vs. time t. Right: Plot vs. dimensionless time θ.

Fig. 4.5, shows the recorded RTD (l.h.s.) and the dimensionless RTD (r.h.s.) of the rhomboidal design. Also for this design, the deviation of the curves plotted in terms of dimensionless time is small. Hence again, a similar flow distribution can be postulated for the given interval of volumetric flow rates. A comparison of the time of first detection ($\theta = 0.45$) and of $\theta_{50} = 0.75$ to the parallel channel design's times shows that the RTD curves of the rhomboidal design ascend faster, which suggests a more compact concentration front, equally as for the spot design.

From the fuel efficiency point of view, the spot design seems to be favourable since a steep and narrow but delayed RTD curve suggests that the methanol

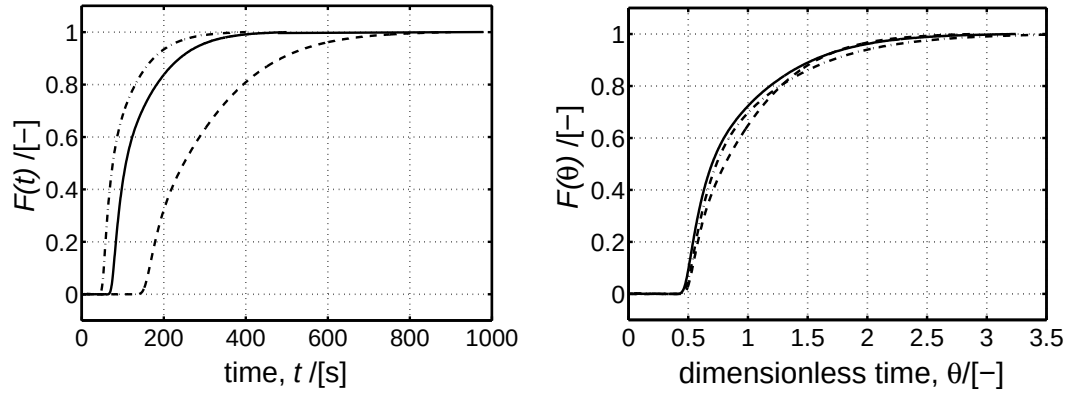

Figure 4.5: Experimental cumulative residence time distribution curves of the rhomboidal design at 5 ml/min (dashed line), 10 ml/min (solid line) and 15 ml/min (dash-dotted line). Left: Plot vs. time t. Right: Plot vs. dimensionless time θ.

molecules have similar residence times in the active area (reaction zone). This leads to a more homogeneous consumption of methanol. The rhomboidal design also shows a steep dimensionless RTD curve. This can not only be attributed to a more compact concentration front, but also to scaling: The large distributor and collector volumes constitute more than 1/3 of the cell volume, leading to a higher mean residence time τ. A direct comparison of the RTD curves vs. time at a given volumetric flow rate shows that the rhomboidal design's RTD curves commence between the ones of the two other designs, and feature slopes which also lie in-between. Interpretation of the RTD results with regard to suitability of the flow field designs for fuel cells can be done in terms of fuel efficiency, but not with regard to active area coverage. The latter is presented on the following pages, where concentration distribution measurements are analysed.

4.3.4 Concentration Distribution

During the residence time experiments, a video camera recorded the propagation of the tracer eosin through the cells. The colour intensity of the flow represents a local mean concentration of tracer over the depth of the investigated cell. The videos were digitally post-processed by assigning different colour intensities, i.e. concentrations, to different colours (procedure and algorithms explained in Appendix A.2).
With this method, concentration fronts within the anode flow fields can be visualised. In the following, the different flow field designs are characterised with respect to homogeneity of concentration distribution over the active area.

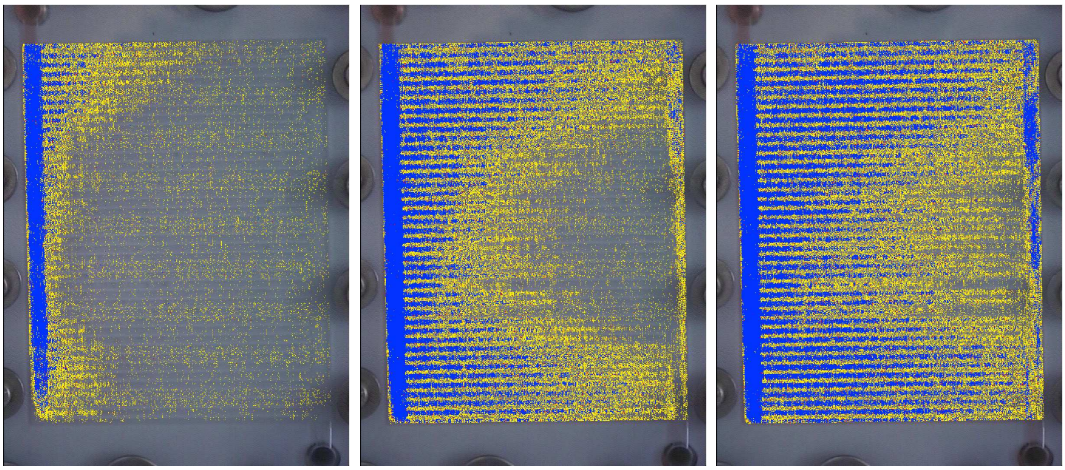

Figure 4.6: False colour snapshots of tracer flow through the parallel channel design at 15 ml/min for time t=15 s (left), t=45 s (middle) and t=75 s (right). Legend: yellow=low concentration; blue=high concentration. Inlet: top left; outlet: bottom right.

Fig. 4.6 shows the flow of the tracer through the parallel channel design at various times. The inlet is the top left corner, and the outlet the bottom right corner. While the concentration front enters the distributor channel and the channels near the inlet, there is no tracer in the other channels. Only when the concentration front reaches the end of the distributor channel, a further propagation into the channels in the active area zone starts. Nonetheless, a homogeneous distribution is not achieved. An inverse parabolic profile is established showing a high volumetric flow rate within the outer channels and a lower volumetric flow rate within the inner channels. Even when most of the active area shows a high concentration, the inverse parabolic profile remains visible, exhibiting a large area of diminished flow rate and concentration. Using such a design in a DMFC will lead to significant concentration, and possibly also current density, differences within the active area, and thus to a lower overall cell performance. A further disadvantage of the design is a higher tendency to blocking of the inner channels with gaseous carbon dioxide, which would add to the already discussed decrease in cell performance.

Computational fluid dynamics (CFD) simulations were performed in order to understand this flow pattern. The simulation yields the same inverse parabolic concentration profile, as can be seen in Fig. 4.7 (l.h.s.). It is caused by the pressure distribution also displayed in Fig. 4.7 (r.h.s.). The pressure differences between the distributor and collector channel are highest near the in- and outlet, causing the highest convective driving forces there. As a result, the flow rates are higher, and consequently also the concentration propagation in the outer channels.

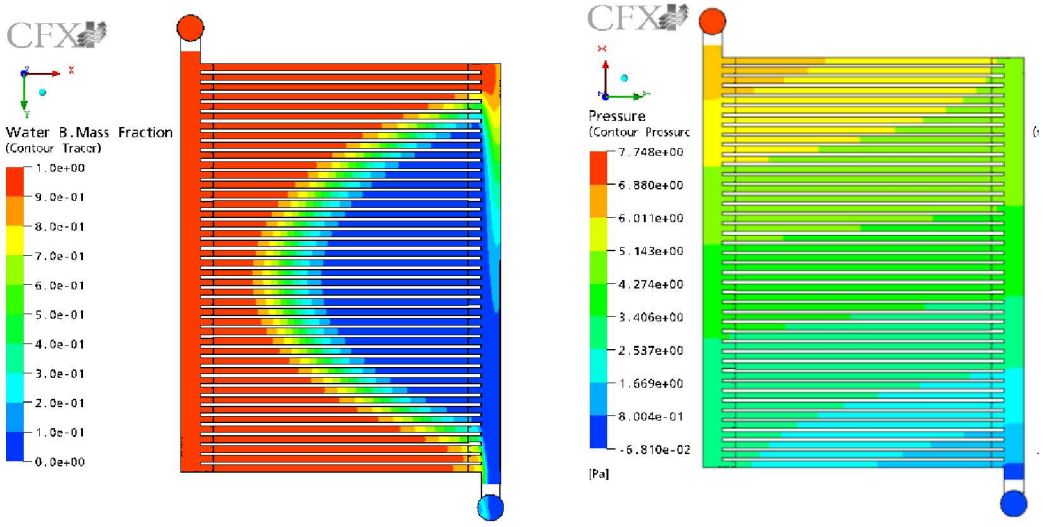

Figure 4.7: Snapshots of a CFD simulation for the parallel channel design at 15 ml/min. Left: Concentration profile at t=45 s. Right: Pressure distribution.

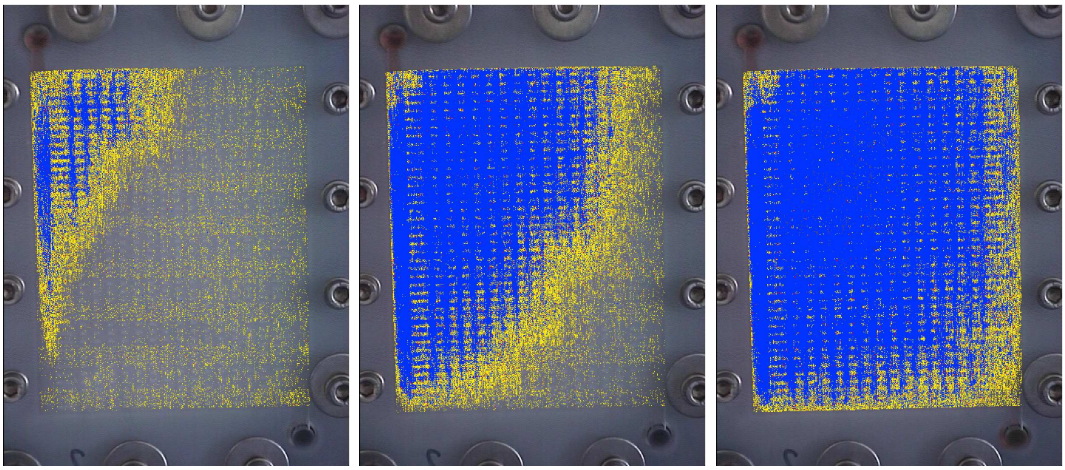

Figure 4.8: False colour snapshots of tracer flow through the spot design at 15 ml/min for time t=15 s (left), t=45 s (middle) and t=75 s (right). Legend: Yellow=low concentration; blue=high concentration. Inlet: top left; outlet: bottom right.

In contrast to the parallel channel design, the spot design shows a more homogeneous concentration propagation without dead zones or bypasses. This can be observed in Fig. 4.8, where the concentration fronts are shown at different times. Although the front in the distributor channel is faster than the one in the perpendicular direction at the inlet, a quasi-diagonal propagation front is established. After 75 s, the concentration is homogeneous over the whole active area. These

findings agree with the RTD results that suggested a narrower concentration front for the spot design than for the parallel channel design. This and the quite homogeneous concentration distribution should be attributed to the cuboids inside the geometry which enable a two-directional flow within the active area, while in the parallel channel design the channels restrict the flow direction to the channel orientation.

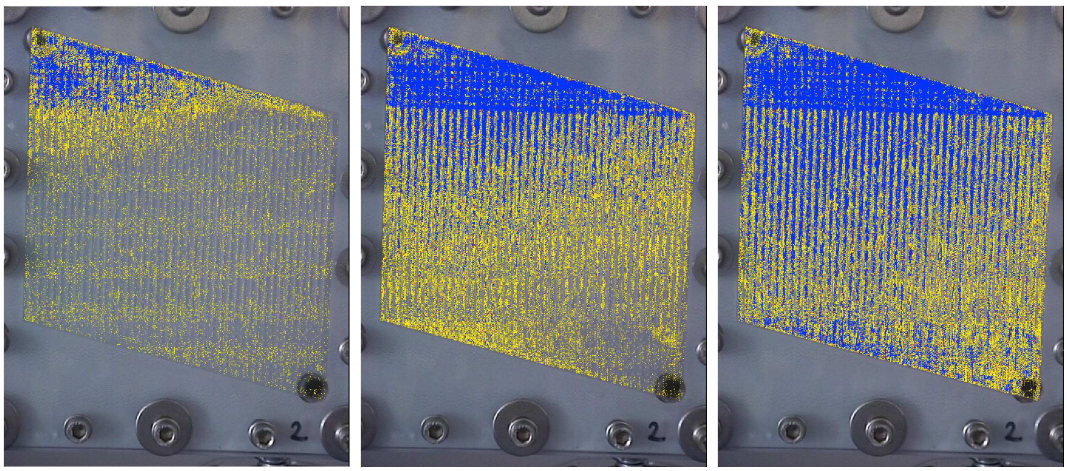

Figure 4.9: False colour snapshots of tracer flow through the rhomboidal design at 15 ml/min for time t=15 s (left), t=45 s (middle) and t=75 s (right). Legend: yellow=low concentration; blue=high concentration. Inlet: top left; outlet: bottom right.

Fig. 4.9 shows the concentration profile inside the rhomboidal design for a volumetric flow rate of 15 ml/min. Since the recorded total cell geometry is larger due to the distributor and collector area, the resolution within the single channels is lower. As a result, the video quality is worse and the concentration front is less pronounced. Nonetheless, the basic flow pattern can be identified in the snapshots: During the first 15 seconds, the tracer is spread over the distributor area and starts entering the channels closest to the inlet. Subsequently, similar as in the parallel channel design, a rightwards shifted, inverse parabolic profile is established, best seen at the propagation of the yellow front. As a result, the flow in the outer channels reaches the outlet faster than that in the inner ones. Nonetheless, the inverse parabolic profile is less pronounced than in the parallel channel design, leading to a more homogeneous concentration distribution over the active area. This is in accordance with the residence time distribution results discussed previously. Therefore, in terms of homogeneity, this design is preferable to the parallel channel design. A comparison of the rhomboidal design to the spot design yields less clear results, also due to the deficiencies in the quality of the recorded snapshots of the rhomboidal design.

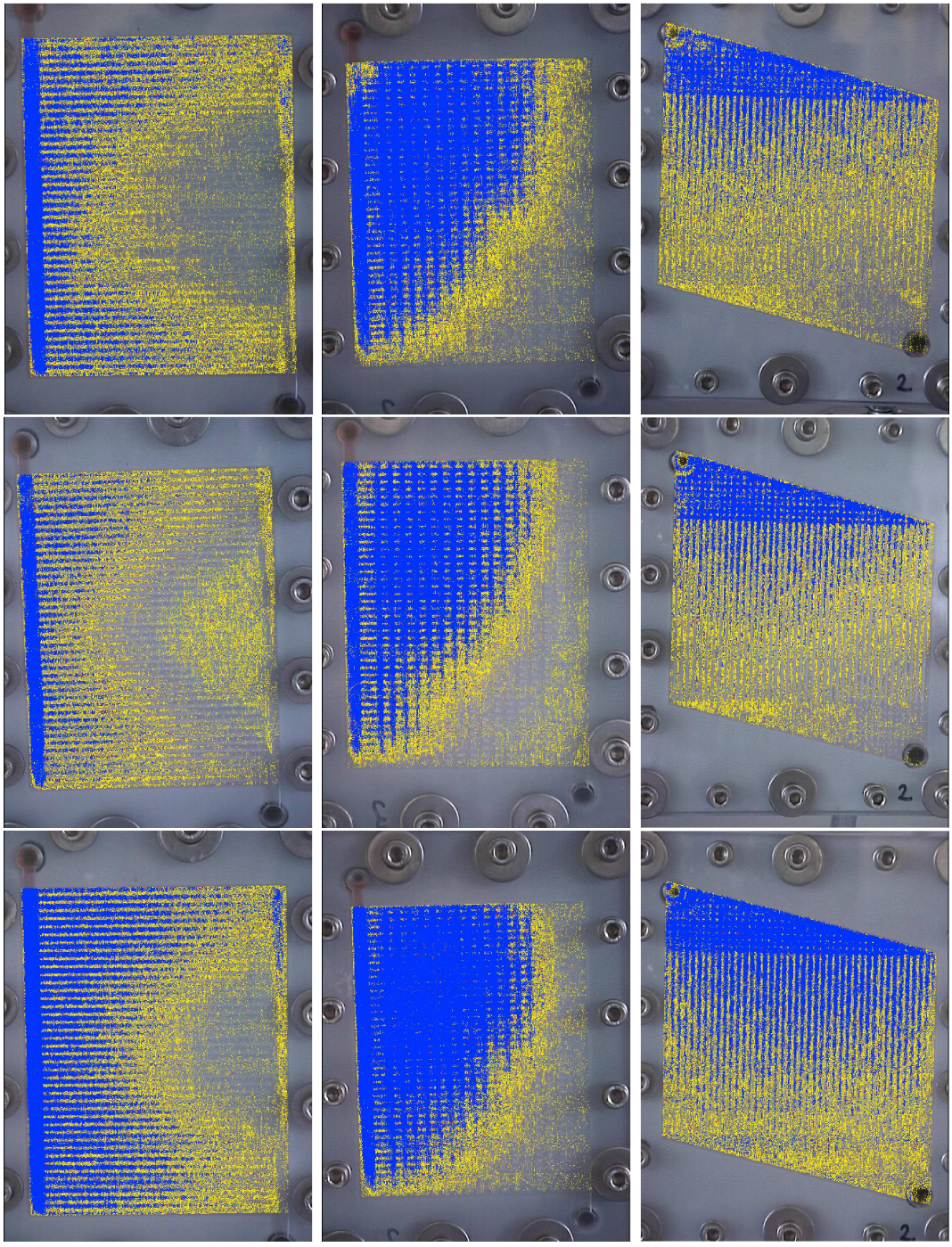

Figure 4.10: False colour snapshots of tracer flow through the three designs at 15 ml/min (top line), 10 ml/min (middle line) and 5 ml/min (bottom line) for dimensionless times corresponding to 45 s at 15 ml/min. Left: Parallel channel design, $\theta = 0.51$. Middle: Spot design, $\theta = 0.48$. Right: Rhomboidal design, $\theta = 0.43$.

Nonetheless, in the RTD curves (Fig. 4.5), as well as in the videos, the concentration front reaches the outlet earlier in the rhomboidal design, even though its inner volume is larger than the spot design's. Therefore, the spot design's flow through the cell is identified as the most homogeneous. This should make it the most suitable flow field design for application in DMFCs in terms of methanol loss at the outlet and in terms of homogeneous supply of methanol to the catalyst layer.

Analysis of the residence time measurements has suggested that the flow pattern in the flow field designs are independent of flow rate over the whole investigated volumetric flow rate region. This result is confirmed by comparing concentration distribution snapshots taken at different flow rates and dimensionless times (Fig. 4.10). The snapshot time corresponds to the dimensionless time at 45 s and 15 ml/min (see Figs. 4.6-4.9). i.e. $\theta = 0.51$ for the parallel channel design, $\theta = 0.48$ for the spot design and $\theta = 0.43$ for the rhomboidal design.

It could be shown, that the flow pattern for all three designs is independent of flow rate. This assumption is essential for the following sections, where models for methanol distribution within the flow field designs are formulated and combined with the electrochemical models from the previous chapter.

4.4 Modelling

In this section, reduced models of the three flow field designs are presented. They are able to describe the experimentally observed hydrodynamic flow through the flow fields quantitatively. For each cell design, a macroscopic model consisting of an ideal reactor network is developed. As mentioned in section 4.1, such reduced models can have advantages to computational fluid dynamic (CFD) models, e.g. when focussing on dynamic aspects. The experimental result that the flow pattern is not changing within a certain flow rate interval simplifies these models even further: The feed distribution into substreams is assumed to be constant for all volumetric flow rates.

Due to the outer dimensions of the flow fields, i.e. 125 mm length x 98 mm width x 2 mm depth for the parallel channel and spot design and 125 mm length x 112 mm width x 2 mm depth for the rhomboidal design, the concentration difference over the depth is of minor importance for the description of the concentration distribution over the whole active area. Furthermore, in the concentration distribution measurements, the snapshots just show a mean concentration over the flow field depth. Hence, this dimension is neglected, and a mean concentration over the flow field depth is used in the models.

The reactor network models shall describe the presented complex flow field structures, which feature a combination of channels and cuboids and of straight and angular outer walls. In addition, easy adaptability to other geometries is strongly favourable. These conditions make an in-depth description of the single components, e.g. single channels, less suitable for implementation. Instead, a similar approach as in CFD modelling is applied: the geometry is divided into interconnected, perfectly mixed compartments. This is equivalent to a network of continuous stirred tank reactors (CSTRs). The exact division of a flow field into compartments and the interconnections between these is done by using concentration distribution videos, or alternatively CFD simulations of the flow field designs.

Ideal reactor networks have been successfully applied by Lacerbe et al. to model the distribution of contamination within a ventilated room [43]. In [74], Wells et al. used CSTR networks to investigate the imperfect mixing effects on the low-density polyethylene process. While Laquerbe et al. validated their reactor network on residence time measurements, Wells et al. used CFD simulations for validation. Here, residence time measurements, as well as video snapshots are used for this purpose.

The CSTR network approach also offers good compatibility with the DMFC model presented at the end of the previous chapter: In both models, all state variables are balanced as lumped, not as distributed variables. Furthermore, both use CSTRs when balancing methanol concentrations. Hence, each flow field compartment can be easily connected to a single lumped DMFC model via the

methanol balance equations in the flow field and catalyst layer. Besides these connections, the single lumped DMFC models are interconnected via the charge balances.

4.4.1 Parallel Channel Design

In Fig. 4.11 (r.h.s.), the CSTR network model for the parallel channel design is presented. It consists of three parts, the distributor and collector channel area, represented by a single white CSTR each, and the geometry at the active area. In chapter 5, each of the grey CSTRs (active area) is connected to a lumped DMFC model.

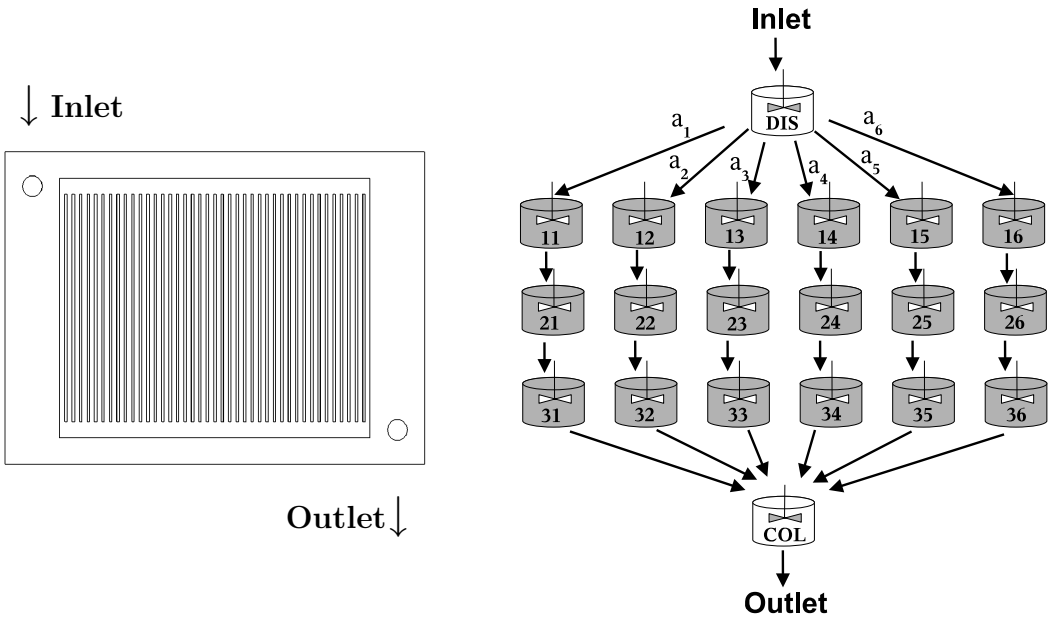

Figure 4.11: Parallel channel design geometry (l.h.s.) and CSTR network representation (r.h.s.).

The inverse parabolic profile observed in the experiments (Fig. 4.6) should be adequately reproduced by the CSTR networks. Therefore, the geometry is discretised into an optimum number of CSTRs, which is determined by a a minimum number of CSTRs required to obtain a concentration profile similar to the experimental one. This reduction enables low computation times and a better integration of the models in complete DMFC models. To reproduce the flow through the channels in the active area, the active area geometry is therefore vertically divided into six CSTRs-in-series with each featuring three CSTRs. Each distributor and collector area is represented by a single CSTR, since the experimental snapshots showed a faster propagation of flow in the distributor and collector area than in the channels. The volume flow leaving the distributor CSTR (top) is split into

six single volume flows, where each flow feeds one of the CSTRs-in-series. Attributing higher flow rates to the outer CSTRs-in-series qualitatively generates the observed inverse parabolic concentration profile. Finally, the collector CSTR is fed by the six volume flows leaving the CSTRs-in-series.
The volume of each CSTR is equivalent to the volume of the respective part of the geometry, i.e. the distributor and collector CSTR volumes are identical to the distributor and collector channel volumes ($V^{DIS} = V^{COL}$= 1.5 ml), and the volume of the geometry at the active area is divided into 6x3 volumes of equal size ($V^{A,CSTR}$= 0.8 ml). The following set of component balance equations for methanol in the CSTRs is obtained:

$$V^{DIS} \cdot \frac{dc^{A,DIS}_{CH_3OH}}{dt} = F^{A,in} \cdot c^{A,in}_{CH_3OH} - \sum_{j=1}^{6} a_j F^{A,in} \cdot c^{A,DIS}_{CH_3OH} \tag{4.3}$$

$$V^{A,CSTR} \cdot \frac{dc^{A,1j}_{CH_3OH}}{dt} = a_j F^{A,in} \cdot (c^{A,DIS}_{CH_3OH} - c^{A,1j}_{CH_3OH}) \tag{4.4}$$

$$V^{A,CSTR} \cdot \frac{dc^{A,2j}_{CH_3OH}}{dt} = a_j F^{A,in} \cdot (c^{A,1j}_{CH_3OH} - c^{A,2j}_{CH_3OH}) \tag{4.5}$$

$$V^{A,CSTR} \cdot \frac{dc^{A,3j}_{CH_3OH}}{dt} = a_j F^{A,in} \cdot (c^{A,2j}_{CH_3OH} - c^{A,3j}_{CH_3OH}) \tag{4.6}$$

$$V^{COL} \cdot \frac{dc^{A,COL}_{CH_3OH}}{dt} = \sum_{j=1}^{6} a_j F^{A,in} \cdot c^{A,3j}_{CH_3OH} - F^{A,in} \cdot c^{A,COL}_{CH_3OH} \tag{4.7}$$

$$\tag{4.8}$$

Here, $c^{A,DIS}_{CH_3OH}$ and $c^{A,COL}_{CH_3OH}$ are the methanol concentration in the distributor and collector CSTR, respectively. $F^{A,in}$ and $c^{A,in}_{CH_3OH}$ are the volumetric flow rate and concentration entering the anode flow field. $c^{A,1j}_{CH_3OH}$, $c^{A,2j}_{CH_3OH}$ and $c^{A,3j}_{CH_3OH}$ are the concentrations in the first, second and third CSTR of the jth CSTRs-in-series with $j \in \{1, 2, 3, 4, 5, 6\}$ (in Fig. 4.11: columns from left to right). The volumetric flow rate through each cascade j is $a_j \cdot F^{A,in}$, where a_j is the ratio of flow rate entering the CSTRs-in-series j to the total flow rate, $F^{A,in}$.
Since the experimentally observed profile is axially symmetric, the feed into the CSTRs-in-series 1 and 6, as well as into 2 and 5, and into 3 and 4 are assumed equal, i.e. $a_1 = a_6$, $a_2 = a_5$, and $a_3 = a_4$.

As shown in the experimental section 4.3, the inlet pipe connecting the three-way cock with the flow field inlet, and the outlet pipe connecting the flow field outlet with the UV-Vis sensor contribute up to 17.5 % of the total volume. Therefore, they have to be accounted for when modelling the experimental residence time and concentration distribution. For all flow field designs, the following mathematical description of the inlet and outlet pipes is used:

Each tube is regarded as an ideal laminar tubular reactor with a parabolic velocity profile. Axial and radial diffusion in the tubes are negligible, since the axial and radial Peclet numbers,

$$Pe_{ax} = \frac{v \cdot l_{tube}}{D_{ew}} \text{ and } Pe_{rad} = \frac{v \cdot 2r_{tube}}{D_{ew}}, \tag{4.9}$$

are very high ($> 10^4$). Here, v is the mean velocity in the respective tube, l_{tube} and r_{tube} are the length and radius of the tube, respectively (inlet pipe: l_{tube} = 0.09 m, r_{tube}=0.002 m; outlet pipe: l_{tube} = 0.055 m, r_{tube}= 0.004 m), and $D_{ew} = 5.34 \cdot 10^{-10}$ m^2/s is the binary diffusivity coefficient of eosin in water calculated acc. Siddiqui and Lucas [65]. The molar volume of eosin required for this calculation is approximated using a group contribution method [15].
Each laminar tube is modelled using equidistant radial discretisation of the pipe cross sectional area into four rings of width Δr. To obtain the parabolic velocity profile in the pipe, each of these elements $i \in \{1, 2, 3, 4\}$ is regarded as an ideal plug flow tubular reactor with volumetric flow rate

$$F^{PFTRi} = 2\pi \int_{(i-1)\cdot\Delta r}^{i\cdot\Delta r} 2 \cdot \frac{F^{A,in}}{\pi r_{tube}^2} \cdot \left[1 - \frac{r^2}{r_{tube}^2}\right] \cdot r \; dr \tag{4.10}$$

and volume

$$V^{PFTRi} = 2\pi \cdot l_{tube} \cdot \int_{(i-1)\cdot\Delta r}^{i\cdot\Delta r} r \; dr. \tag{4.11}$$

This yields the following concentration at the pipe outlet $c^{pipe,out}(t)$ as a function of the concentration entering the tube $c^{pipe,in}_{CH_3OH}(t - \Delta t)$:

$$c^{pipe,out}(t) = \sum_{i=1}^{4} \frac{F^{PFTRi}}{F^{A,in}} \cdot c^{pipe,in}\left(t - \frac{V^{PFTRi}}{F^{PFTRi}}\right) \tag{4.12}$$

For the inlet pipe, the following holds:

$$c^{pipe,in}(t) = \begin{cases} 0 & : \; t \leq 0 \\ c^{A,in}_{CH_3OH}(\infty) & : \; t > 0 \end{cases}; \quad c^{A,in}_{CH_3OH}(t) = c^{pipe,out}_{CH_3OH}(t) \; , \tag{4.13}$$

and for the outlet pipe:

$$c^{pipe,in}(t) = c^{A,COL}_{CH_3OH}(t); \quad c^{A,sensor}_{CH_3OH}(t) = c^{pipe,out}(t). \tag{4.14}$$

The residence time sum curve is the concentration at the end of the outlet pipe, i.e. at the sensor, divided by the final concentration in the network, i.e. at $t \to \infty$:

$$F(t) = c^{A,sensor}_{CH_3OH}(t) / c^{A,in}_{CH_3OH}(\infty) \tag{4.15}$$

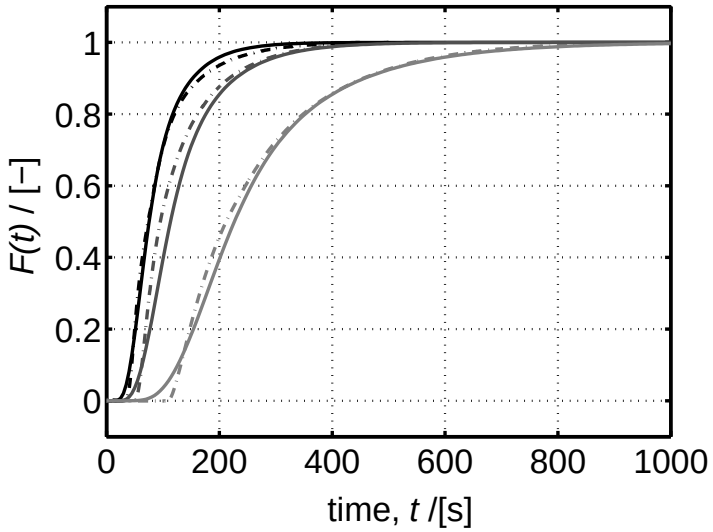

Figure 4.12: Experimental (dash-dotted lines) and simulated (solid lines) cumulative residence time distributions of the parallel channel design at the volumetric flow rates 5 ml/min (light grey), 10 ml/min (grey) and 15 ml/min (black).

For fitting the model to the experimental concentration profile and residence time distribution, only the fractions a_i characterising the distributor CSTR were optimised: The parameters were fitted to the cumulative residence time measurements, and the resulting parameters were slightly adjusted to the concentration front propagation snapshots of the experiment at various times. The parameters were changed by less than 5% (absolute) in this last step, so that the cumulative residence time as well as the experimentally observed concentration fronts can be reproduced. The optimised distribution is: 28 % flow through the outer CSTRs-in-series 1 and 6, i.e. $a_1 = a_6 = 0.28$, 14 % flow through the CSTRs-in-series 2 and 5, i.e. $a_2 = a_5 = 0.14$, and 8 % flow through the central CSTRs-in-series 3 and 4, i.e. $a_3 = a_4 = 0.08$. Fig. 4.12 shows the simulated residence time curves in comparison to the experiments for the volumetric flow rates 5 ml/min, 10 ml/min and 15 ml/min. Obviously, good agreement between experiments and simulations is achieved. The same holds for the concentration distribution within the flow field, which is illustrated in Fig. 4.13. The experimental snapshots at 15 s, 45 s and 75 s for a volumetric flow rate of 15 ml/min are shown to the left, and the respective single concentrations within the CSTRs to the right. In the simulation, blue colour denotes a concentration ≥ 0.55 mol/l, and yellow a concentration between 0.32 mol/l and 0.55 mol/l. Maximum inlet concentration is 1 mol/l. It can be seen that for all three times the model predicts a concentration profile similar to

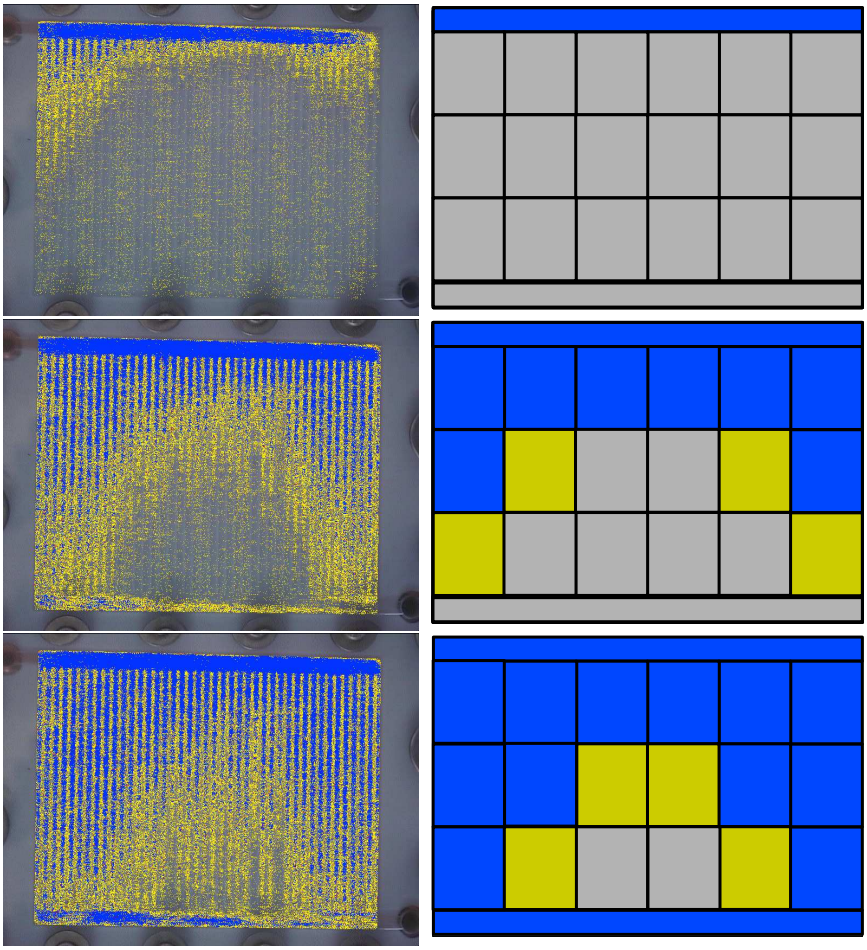

Figure 4.13: Experimental (l.h.s.) vs. simulated (r.h.s.) concentration front snapshots in the parallel channel design for 15 ml/min at various times t: t=15 s (top), t=45 s (middle) and t=75 s (bottom).

the experimental results. It can be concluded, that the presented CSTR network model is suitable to predict the hydrodynamic behaviour of the parallel channel flow field design.

4.4.2 Spot Design

A similar approach as for the parallel channel design is used for modelling the spot design. The model representation is illustrated in Fig. 4.14. The main difference between the parallel channel design flow field and the spot design flow field is the rib geometry: The spot design contains interlaced ribs, which enable a horizontal and vertical flow within the active area geometry. This allows the fluid to move diagonally through the flow field from inlet to outlet (see section 4.3). The model accounts for this flow field property by using a network of CSTRs with horizontal

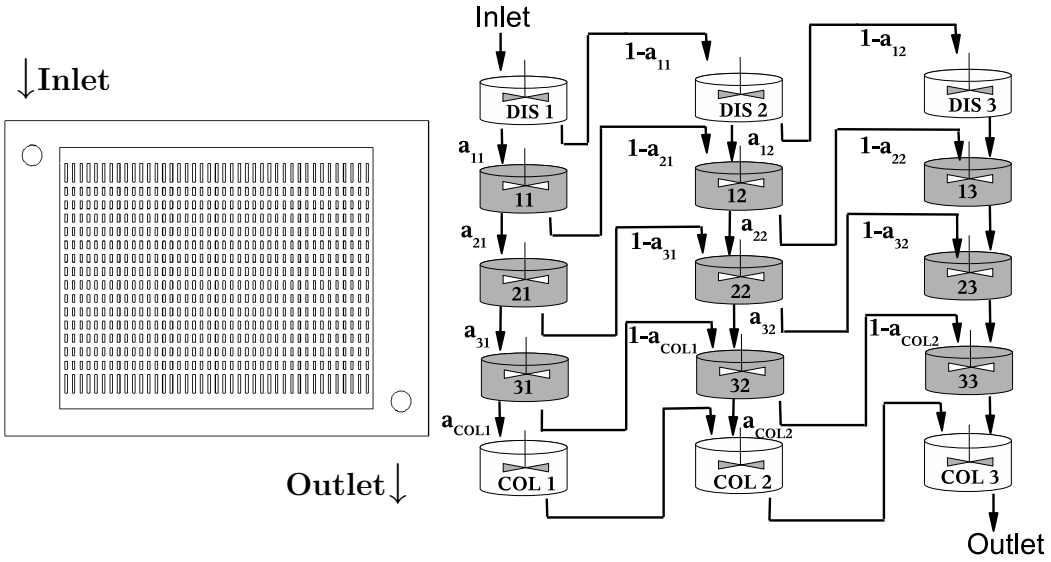

Figure 4.14: Spot design flow field (left) and respective CSTR network model (right).

and vertical connections to neighbouring CSTRs. Due to the diagonal concentration propagation, the distributor and collector channels are each represented by three CSTRs (white) in a series. These feed the active area structure (grey), consisting of 3x3 CSTRs. Each CSTR feeds the neighbouring CSTR to its right and to its bottom. Since the flow through this flow field is more homogeneous than that through the parallel channel design, the number of columns of CSTRs can be reduced from 6 to 3. The volume of each CSTR is equivalent to the volume of the respective part of the geometry, i.e. each distributor and collector CSTR volume, V^{DIS} and V^{COL} respectively, is identical to 1/3 of the distributor and collector channel volume of 1.5 ml, and the volume of the active area is divided into 3x3 volumes $V^{A,CSTR}$ of equal size (= 1.7 ml).
The following mass balance equation for methanol is obtained:

$$\begin{aligned} V^k \cdot \frac{dc^{A,ij}_{\mathrm{CH_3OH}}}{dt} &= a_{ij}F^{A,(i-1)j} \cdot c^{A,(i-1)j}_{\mathrm{CH_3OH}} + (1 - a_{(i+1)(j-1)})F^{A,i(j-1)} \cdot c^{A,i(j-1)}_{\mathrm{CH_3OH}} \\ &\quad - a_{(i+1)j}F^{A,ij} \cdot c^{A,ij}_{\mathrm{CH_3OH}} - (1 - a_{(i+1)j})F^{A,ij} \cdot c^{A,ij}_{\mathrm{CH_3OH}} \end{aligned} \tag{4.16}$$

The volumetric flow rates are calculated using the total mass balance:

$$a_{ij}F^{A,(i-1)j} + (1 - a_{(i+1)(j-1)})F^{A,i(j-1)} = a_{(i+1)j}F^{A,ij} + (1 - a_{(i+1)j})F^{A,ij} \tag{4.17}$$

Here, $i \in \{DIS, 1, 2, 3, COL\}$ denotes the row and $j \in \{1, 2, 3\}$ the column (see Fig. 4.14). $k \in \{DIS,\ A, CSTR,\ COL\}$ defines the respective CSTR volume

V^k. The following boundary conditions reduce the number of fractions a_{ij} to 8:

$$\text{if} \quad ij = DIS1 \quad \text{then} \quad a_{ij} = 1;\ (i-1)j = in \tag{4.18}$$
$$\text{if} \quad i = DIS \quad \text{then} \quad a_{ij} F^{A,(i-1)j} = 0 \tag{4.19}$$
$$\text{if} \quad i = COL \quad \text{then} \quad a_{(i+1)j} = 1;\ a_{(i+1)(j-1)} = 0 \tag{4.20}$$
$$\text{if} \quad j = 1 \quad \text{then} \quad (1 - a_{(i+1)(j-1)}) F^{A,i(j-1)} \cdot c_{\mathrm{CH_3OH}}^{A,i(j-1)} = 0 \tag{4.21}$$
$$\text{if} \quad j = 3 \quad \text{then} \quad a_{ij} = 1;\ a_{(i+1)j} = 1 \tag{4.22}$$

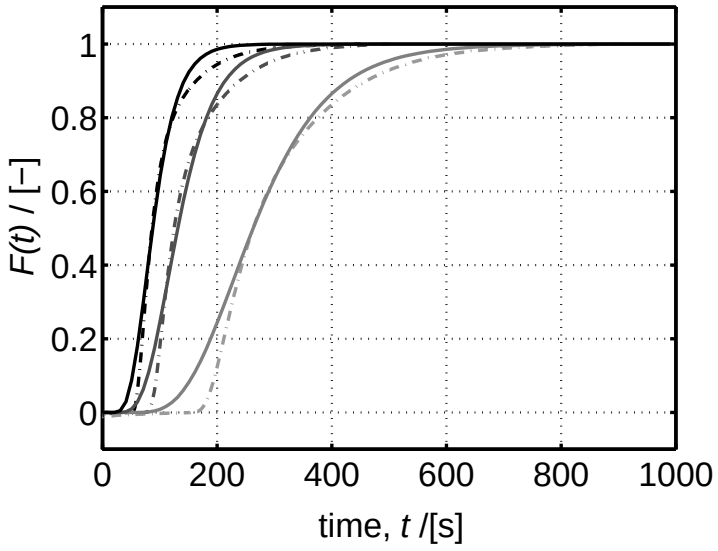

Figure 4.15: Experimental (dash-dotted lines) and simulated (solid lines) cumulative residence time distributions of the spot design at the volumetric flow rates 5 ml/min (light grey), 10 ml/min (grey) and 15 ml/min (black).

For fitting the model to the experimental concentration profile and residence time distribution, the eight parameters $a_{11}, a_{12}, a_{21}, a_{22}, a_{31}, a_{32}, a_{COL1}, a_{COL2}$ are identified. Due to the geometry and the experimental concentration front snapshots, the following parameters are regarded as identical: $a_{11} = a_{12}$, $a_{21} = a_{31}$, $a_{22} = a_{32}$, $a_{COL1} = a_{COL2}$.
The inlet and outlet pipes are included in the model as described in the parallel channel design, using $c^{pipe,in} = c_{\mathrm{CH_3OH}}^{A,COL3}$ for the outlet pipe.

The approach to identify the parameter values is identical to one of the parallel channel design. The parameter set satisfying the experimental residence time distribution measurements as well as the recorded concentration front propagation through the flow field is:
$a_{11} = a_{12} = 63\%$; $a_{21} = a_{31} = 60\%$; $a_{22} = a_{32} = 62\%$; $a_{COL1} = a_{COL2} = 44\%$.

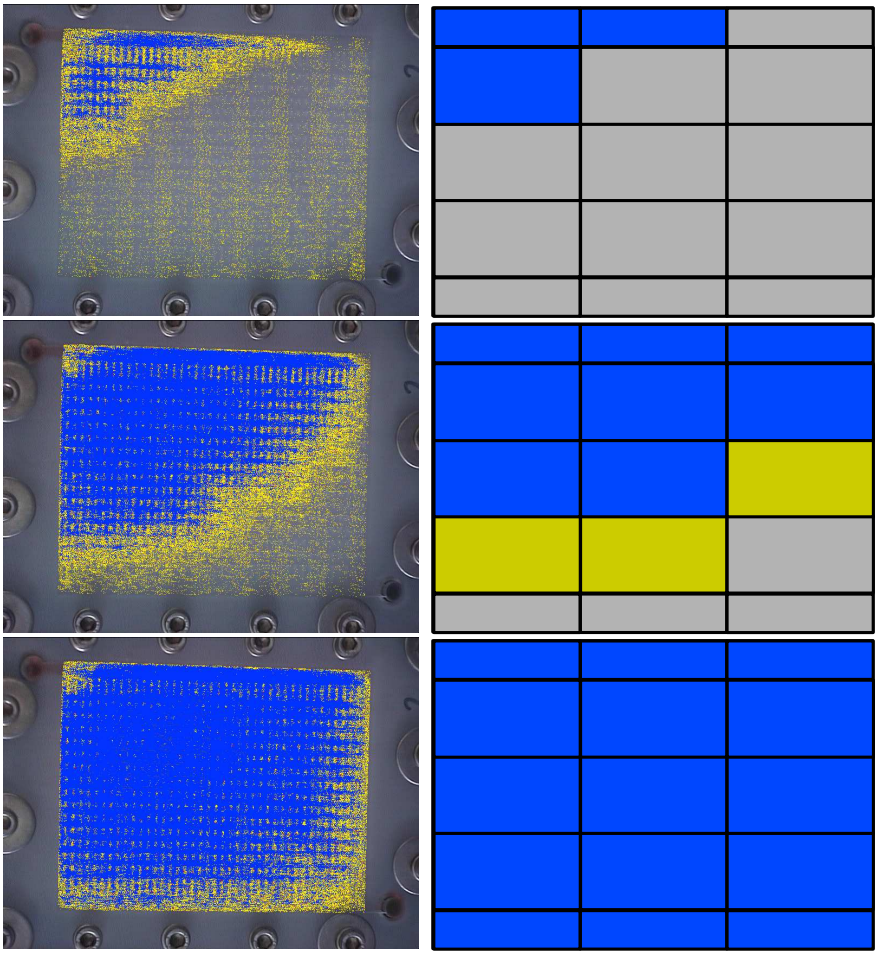

Figure 4.16: Experimental (l.h.s.) vs. simulated (r.h.s.) concentration front snapshots of the spot design for 15 ml/min and various times t: t=15 s (top), t=45 s (middle) and t=75 s (bottom).

Fig. 4.15 shows the residence time measurements for the volumetric flow rates 5 ml/min, 10 ml/min and 15 ml/min and the representative model predictions. Experiment and simulation are very similar, taking into acount that, due to the limited number of CSTRs, the steep slope of the experimental curves can not be reproduced quantitatively. The simulated and experimental concentration distributions within the spot design flow field are shown in Fig. 4.16. To the left, experimental snapshots at 15 s, 45 s and 75 s are shown for a flow rate of 15 ml/min, and to the right are the concentrations within the single CSTRs predicted by the model. In the simulation, blue colour denotes a concentration ≥ 0.4 mol/l, and yellow a concentration between 0.25 mol/l and 0.4 mol/l. The maximum concentration is 1 mol/l. As for the parallel channel design, the model generates concentration profiles similar to those obtained in the experiment. The presented

CSTR network model is therefore suitable for reproducing the hydrodynamic behaviour of the spot design.

4.4.3 Rhomboidal Design

The rhomboidal flow field and its model representation are displayed in Fig. 4.17. The model consists of three parts: The distributor and collector channel areas (white), and the active area (grey).

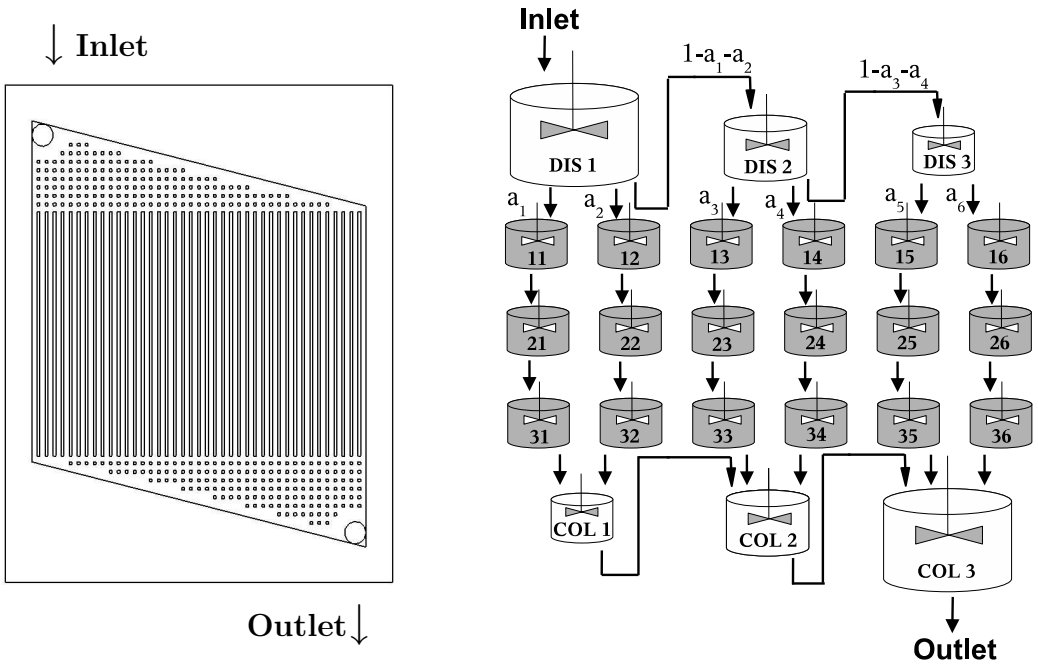

Figure 4.17: Rhomboidal design flow field (l.h.s.) and the corresponding CSTR network model (r.h.s.).

Since the geometry of the active area of the rhomboidal flow field is identical to that of the parallel channel flow field, the same active area CSTR network is used. The difference lies in the distributor and collector area, which are of triangular shape and feature cuboids. To represent the flow distribution in these triangular regions, interconnected CSTRs of varying size are used: Equivalent to the real geometry, the size of a distributor CSTR decreases with increasing distance to the inlet, and the size of a collector CSTR decreases with increasing distance to the outlet. A number of three distributor and three collector CSTRs was found to enable a flow distribution over the active area which is sufficiently accurate for the here presented studies. Each of these CSTRs is connected to two CSTRs-in-series of the active area. The volume of the single CSTRs in the distributor and collector area is: 2 ml, 1.2 ml and 0.4 ml, which corresponds to 55.4 %, 33.2 % and 11.4 % of the distributor or collector volume. The volume of the active area

CSTRs is $V^{A,CSTR} = 0.8$ ml (see parallel channel design).

The following set of mass balance equations for methanol in the CSTRs is obtained:

$$\begin{aligned} V^{DISj} \cdot \frac{dc^{A,DISj}_{CH_3OH}}{dt} &= (1 - \sum_{h=2j-3}^{2j-2} a_h) F^{A,DIS(j-1)} \cdot c^{A,DIS(j-1)}_{CH_3OH} \\ &\quad - \sum_{h=2j-1}^{2j} a_h F^{A,DISj} \cdot c^{A,DISj}_{CH_3OH} \\ &\quad - (1 - \sum_{h=2j-1}^{2j} a_h) F^{A,DISj} \cdot c^{A,DISj}_{CH_3OH} \end{aligned} \tag{4.23}$$

$$V^{A,CSTR} \cdot \frac{dc^{A,1i}_{CH_3OH}}{dt} = a_i F^{A,DISj} \cdot (c^{A,DISj}_{CH_3OH} - c^{A,1i}_{CH_3OH}) \tag{4.24}$$

$$V^{A,CSTR} \cdot \frac{dc^{A,2i}_{CH_3OH}}{dt} = a_i F^{A,DISj} \cdot (c^{A,1i}_{CH_3OH} - c^{A,2i}_{CH_3OH}) \tag{4.25}$$

$$V^{A,CSTR} \cdot \frac{dc^{A,3i}_{CH_3OH}}{dt} = a_i F^{A,DISj} \cdot (c^{A,2i}_{CH_3OH} - c^{A,3i}_{CH_3OH}) \tag{4.26}$$

$$\begin{aligned} V^{COLj} \cdot \frac{dc^{A,COLj}_{CH_3OH}}{dt} &= \sum_{h=2j-1}^{2j} a_h F^{A,DISh} \cdot c^{A,3h}_{CH_3OH} + F^{A,COL(j-1)} \cdot c^{A,COL(j-1)}_{CH_3OH} \\ &\quad - F^{A,COLj} \cdot c^{A,COLj}_{CH_3OH} \end{aligned} \tag{4.27}$$

$c^{A,1i}_{CH_3OH}$, $c^{A,2i}_{CH_3OH}$ and $c^{A,3i}_{CH_3OH}$ are the concentrations in the first, second and third CSTR in each CSTRs-in-series, with $i \in \{1,2,3,4,5,6\}$ (columns from left to right). $j \in \{1,2,3\}$ refers to the distributor or collector CSTR j (from left to right). The following boundary conditions hold:
$a_{-1} = a_0 = 0$, $DIS0 = in$, $F^{A,COL0} \cdot c^{A,COL0}_{CH_3OH} = 0$, $a_6 = 1 - a_5$ and
$j = 1$ for $i \in \{1,2\}$, $j = 2$ for $i \in \{3,4\}$, $j = 3$ for $i \in \{5,6\}$.
The inlet and outlet pipes are included in the model as described for the parallel channel design, using $c^{pipe,in} = c^{A,COL3}_{CH_3OH}$ for the outlet pipe.
Since the flow through the active area region is asymmetric, all five flow ratios a_1, a_2, a_3, a_4 and a_5 had to be identified. The optimising procedure is identical to the parallel channel design parameter optimisation. The following parameter values were identified: a_1= 15.2 %, a_2=24.8 % , a_3=35.6 % , a_4=19.3 % and a_5= 38 %. As displayed in Fig. 4.18, the simulated residence time behaviour is similar to the experimental one. But, due to the limited number of CSTRs, the steep slope of the experimental curves can not be reproduced quantitatively. Fig. 4.19 shows the experimental and simulated concentration distribution. In the simulations, blue colour denotes a concentration $\geq$ 0.5 mol/l, and yellow a

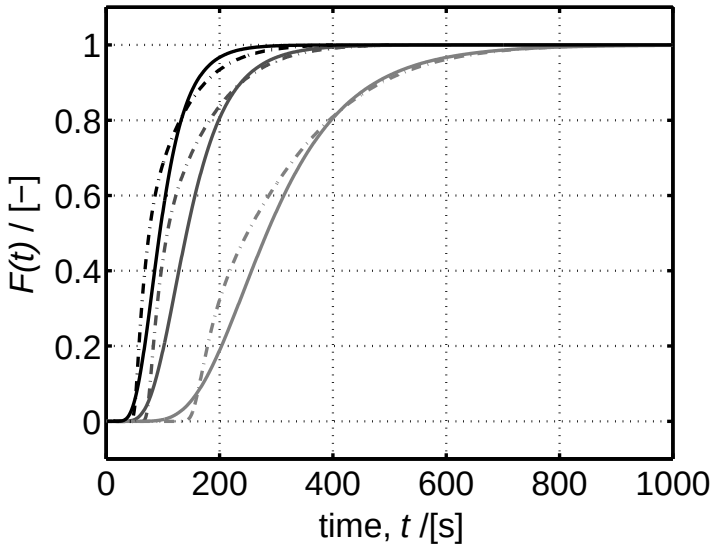

Figure 4.18: Experimental (dash-dotted line) and simulated (solid line) cumulative residence time distributions of the rhomboidal design at the volumetric flow rates 5 ml/min (light grey), 10 ml/min (grey) and 15 ml/min (black).

concentration between 0.15 mol/l and 0.5 mol/l, the maximum concentration is 1 mol/l. The model reproduces the experimental concentration front propagation vs. time quantitatively.

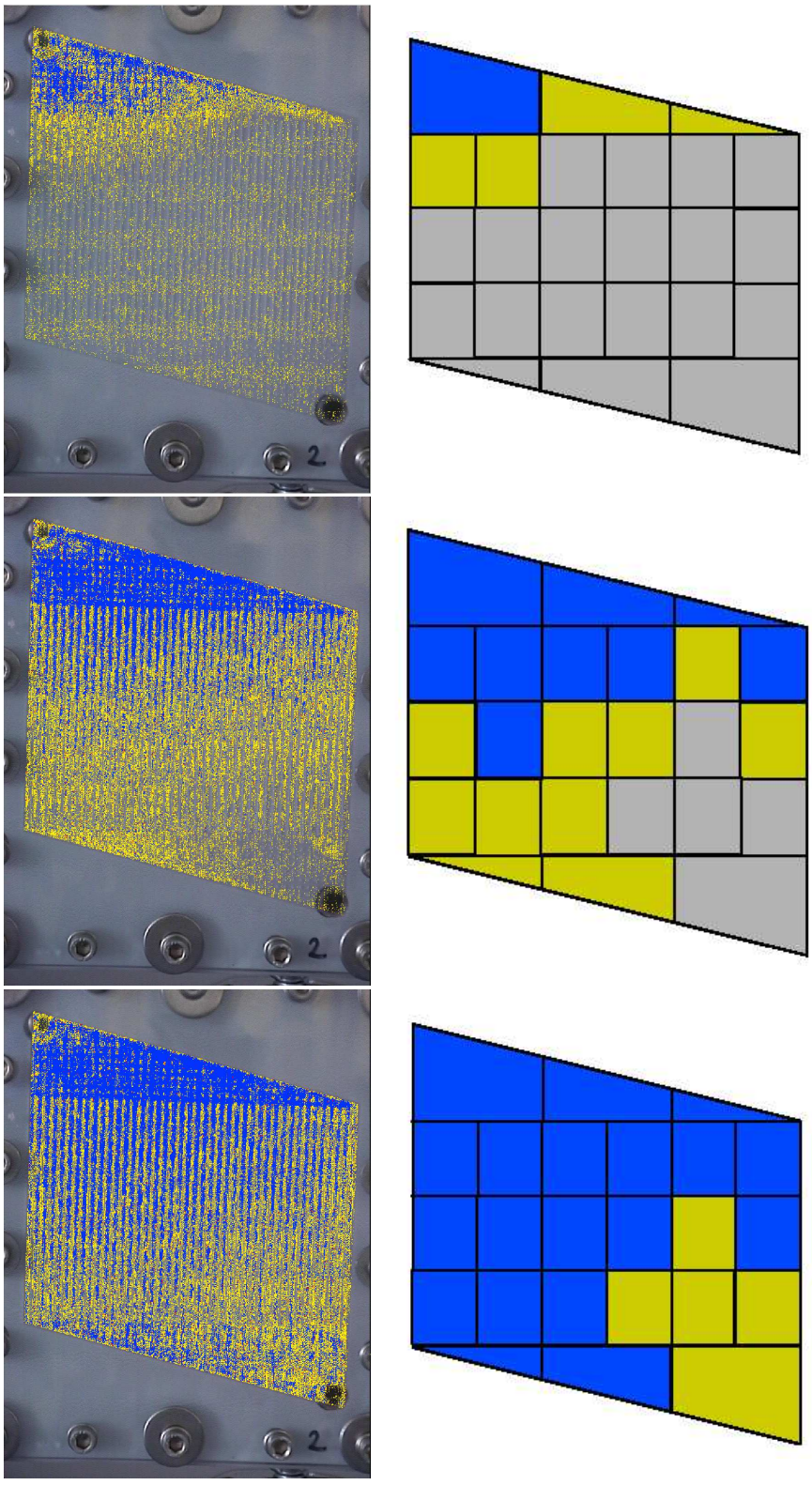

Figure 4.19: Experimental (l.h.s.) vs. simulated (r.h.s.) concentration front snapshots in the rhomboidal design for 15 ml/min and various times t: t=15 s (top), t=45 s (middle) and t=75 s (bottom).

4.5 Concluding Remarks on the Hydrodynamic Characterisation

This chapter presented the development of reduced hydrodynamic models of anode flow fields. In a first step, three anode flow fields were developed. They were hydrodynamically characterised using residence time distribution and concentration distribution measurements. The analysis identified drawbacks and advantages of the single designs with respect to hydrodynamic aspects. In some flow fields, the velocity profile was highly non-uniform. This indicates potential local mass transport limitations, i.e. of methanol transport and of carbon dioxide removal, at the zones with diminished velocity.
The hydrodynamic behaviour of the flow fields was modelled by means of ideal reactor networks. These proved suitable for quantitatively describing the experimentally observed behaviour. Therefore, they are integrated into DMFC models in the following chapter. This will help to determine the influence of flow field designs on the steady state and dynamic behaviour of DMFCs.

Chapter 5

Characterisation of the Dynamic and Steady State Behaviour of DMFCs

5.1 Introduction

This chapter combines the model formulations of the preceeding chapters and analyses the interplay of the physico-chemical phenomena governing the behaviour of the DMFC.
To obtain high system efficiencies, it is attractive to operate DMFCs at low volumetric flow rates. Under such conditions, the concentration distribution of methanol inside the anode flow field structures may have a significant influence on the dynamic and steady state DMFC performance. Therefore, besides studies of the influence of current density and methanol concentration on the dynamic behaviour of the DMFC, also studies of the influence of the distribution of methanol inside anode flow fields are presented.

In a first step, the flow field designs presented in chapter 4 are experimentally analysed with regard to their influence on the DMFC performance (section 5.2). Subsequently, model based studies show the influence of concentration and current density on the cell voltage response (section 5.3.1). DMFC models are investigated which combine the hydrodynamic models of chapter 4 with the DMFC model from section 3.4, which contains the identified anode reaction kinetics. They are shown to correctly predict the experimental behaviour (sections 5.3.2-5.3.3).
Finally, a comparison of simulated and experimental results illustrates the flow field influence on the dynamic DMFC behaviour and the validity of the presented models.

5.2 Experimental

All three flow field designs presented in chapter 4 are combined with the following elements to generate complete single-cell DMFCs:

- A MEA with an active area of 100 cm^2.
- A cathode compartment.
- PTFE-coated Toray graphite paper as anode and cathode diffusion layer. They cover the complete anode and cathode flow field areas.
- Gold plated current collector plates.
- End plates and bolts for bracing the DMFC together.

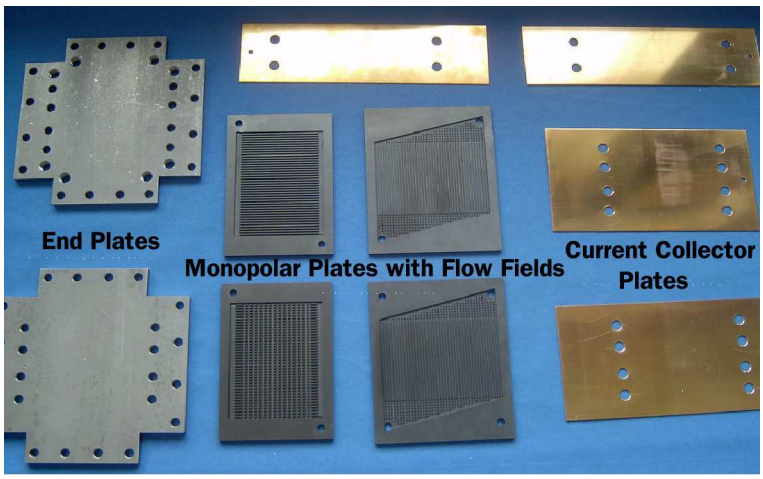

Figure 5.1: Components of the investigated 100 cm^2 DMFC with different anode flow field geometries.

The cathode flow field geometry of the DMFCs with parallel channel or spot design anode compartments is identical to the parallel channel design geometry. DMFCs with the rhomboidal anode flow field geometry use the same geometry also for the cathode compartment. In all cases, the media flow on anode and cathode side is counter current. The flow fields, collector plates and end plates are depicted in Fig. 5.1. All materials used in the DMFCs are identical to the ones of the 26 cm^2 DMFC presented in section 2.2.3.

The measurements were conducted using the DMFC miniplant presented in chapter 2. Except for the anode volume flow rate, the operating conditions were the same as in the experiments with the 26 cm^2 DMFC (section 2.2.3). The same is

true for the steady-state measurements: they were conducted galvanostatically, and the mean cell voltage recorded between 570 s and 600 s after setting the cell current density was used as steady state values for the polarisation curves. The exact time at which a steady state cell voltage is assumed is usually not mentioned in literature; it may be as low as 120 seconds after establishing a current load [57]. As shortly discussed in the following, the time span after which a steady state is assumed may have a crucial effect on the resulting polarisation curve.

5.2.1 Parallel Channel Design

Considerations on the Steady State

Fig. 5.2 shows two polarisation curves of the parallel channel design flow field DMFC (pcd-DMFC) with cell voltages taken a) between 150 and 180 seconds (mean value) and b) between 570 and 600 seconds (mean value) after establishing a cell current density. While the curves are identical for low cell current densities, they diverge at higher cell current densities. In the high cell current density region, the presented cell voltage is much higher for case a). As a result, the polarisation curve with cell voltages taken at earlier times suggests a higher steady state cell performance at high cell current densities.

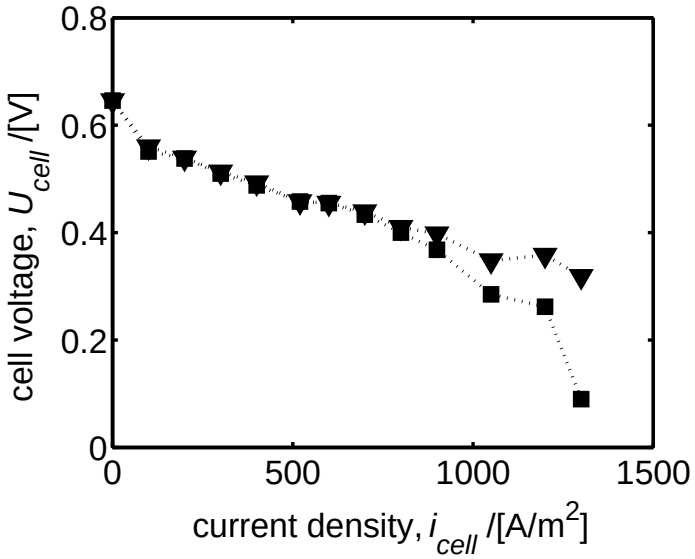

Figure 5.2: Experimental polarisation curves of the pcd-DMFC with steady states postulated after 150 seconds (triangles) and 570 seconds (squares). Anode volume flow rate: 50 ml/min.

The reason for the deviation of the curves is that the presented DMFC shows difficulties to reach a steady state at high cell current densities. Carbon dioxide

evolution is less influencing the cell voltage response at low current densities, but has a large impact at high cell current densities: Carbon dioxide bubbles most probably block the transport of methanol to and its adsorption on the catalyst. This conclusion can also be drawn from stoichiometric considerations: At the limiting cell current density, less than 3 % of the methanol fed to the anode compartment is consumed at the anode catalyst layer. Under the assumption of negligible carbon dioxide influence, a variation of current density would only marginally change the methanol concentration inside the flow field. Only at current densities much higher than the experimentally applied ones, a mass transport induced limiting current density would be expected. It therefore can be concluded that limitations of the carbon dioxide removal are the major reason for the low performance at high cell current densities: Gaseous carbon dioxide hinders the methanol transport to a large part of the active area.

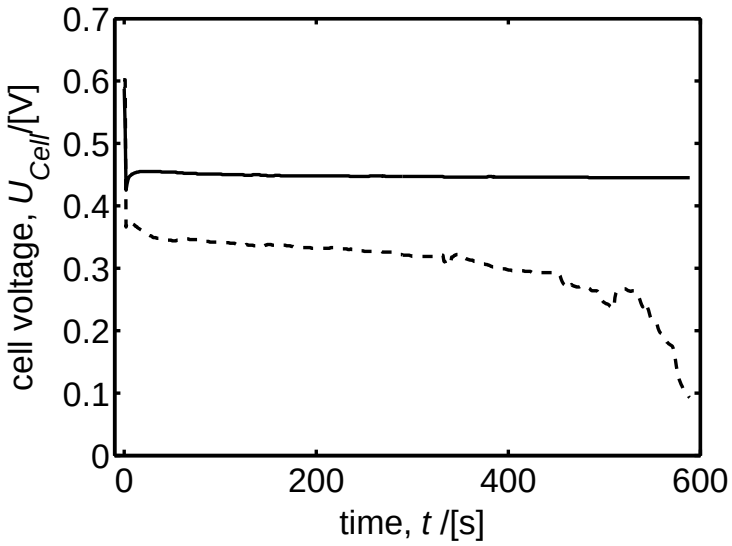

Figure 5.3: Experimental cell voltage response of the pcd-DMFC to a step from OCV to 700 A/m^2 (solid line) and to 1300 A/m^2 (dashed line). Anode volume flow rate: 50 ml/min.

Fig. 5.3 illustrates the influence of this phenomenon on the transient cell voltage at a low (solid line) and at a high (dashed line) cell current density. While at low cell current densities, the cell voltage response is smooth and shows a stable cell voltage after several seconds, at high cell current densities, the cell voltage signal decays slowly and shows increasing fluctuations after several minutes. No steady state is reached even after 600 seconds. It is questionable whether a stable steady state can be reached at all. A similar, slightly more stable behaviour was observed for the DMFC presented in section 2.2.3. There, although the anode flow rate has been ten times larger (500 ml/min), fluctuations at high cell current

densities were observed as well (see Fig. 2.5).
As will be shown later also for the spot and rhomboidal design DMFCs, the flow field geometry has an impact on the removal of carbon dioxide, i.e. on the stability of the cell voltage at medium to high current densities. The relatively low limiting cell current density of the pcd-DMFC may be attributed to the following effect: The velocity profile in the flow field is inverse parabolic (see Fig. 4.6), showing very low volume flows through the central channels. At high cell current densities, evolving carbon dioxide bubbles block these channels. Neither can newly generated carbon dioxide be removed from nor can methanol be transported into the channels (see also stoichiometric considerations in the previous paragraph). This prevents methanol transport to the catalyst sites at the channels. As a result the overall cell voltage should decrease. The presented pcd-DMFC is therefore not optimal with regard to carbon dioxide removal, and operation at high cell current densities should be avoided.

Influence of Anode Volume Flow Rates

Fig. 5.4 shows the influence of the anode flow rate on the steady state behaviour of the pcd-DMFC. The anode flow rates of 50 ml/min and 100 ml/min correspond to mean residence times τ of 22 seconds and 11 seconds in the anode compartment, respectively. The polarisation curves show identical behaviour at low current densities, but lower cell voltages (≈ 0.05 V) between 300 and 1000 A/m^2 for the lower volumetric flow rates (50 ml/min), and an earlier decline at 50 ml/min in the mass transport dominated region (> 1000 A/m^2). Obviously, the performance at an anode flow rates of 50 ml/min, where < 3 % of the methanol fed into the anode compartment is consumed at the limiting cell current density, is lower than the performance at 100 ml/min, where < 1.5 % of the methanol is consumed. Taking into account such low consumptions of methanol, a minor influence of the anode volume flow variation on the cell performance would be expected, in case that the carbon dioxide influence was negligible. The experimental differences between the polarisation curves at 50 and 100 ml/min should therefore be attributed to the carbon dioxide influence (see also previous paragraphs). An increasing anode volume flow rate seems to remove more gaseous carbon dioxide from the anode diffusion layer and catalyst layer, and from the anode compartment.
The dependence of the polarisation curve on the volumetric flow rate is in contrast to the findings of Scott and coworkers [5], where lower flow rates led to higher cell voltages at low and medium current densities. The authors ascribe this dependence to methanol crossover: A lower anode flow rate causes lower anode methanol concentration; this induces lower methanol crossover and lower absolute cathode overpotential; since the anode overpotential is insensitive to methanol concentration, the overall cell voltage is higher. The finding of an opposite effect of flow rate on the cell performance suggests that, for the here

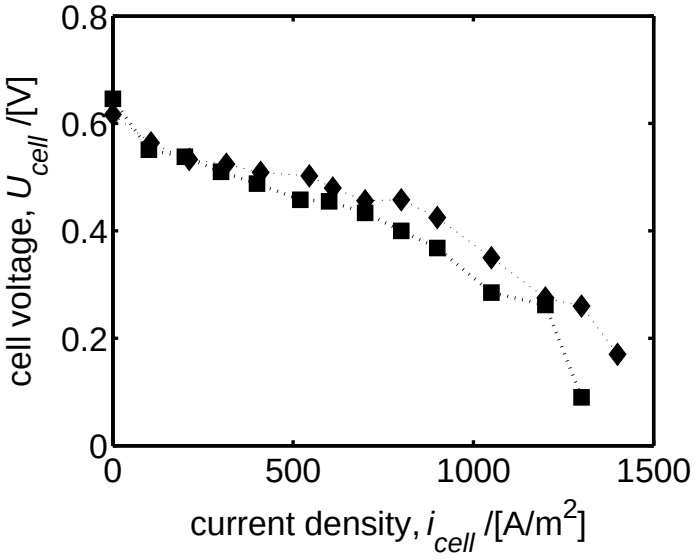

Figure 5.4: Influence of anode volume flow rate on the experimental polarisation curve of the pcd-DMFC. Anode flow rate: 50 ml/min (squares) and 100 ml/min (diamonds).

presented pcd-DMFC, the carbon dioxide effect has a stronger influence on cell performance than the methanol crossover effect. Hence, an increase of anode flow rate leads to an increase of the cell voltage.

The influence of anode volume flow rate on the dynamic behaviour of the pcd-DMFC for current steps within the pseudo-Ohmic region of the polarisation curve is discussed in the following. All presented cell voltage responses are calculated using the mean values of at least two measurements to ensure reproducibility. Between all measurements, OCV was maintained for 1 hour. Fig. 5.5 shows the cell voltage response to a current step down from 520 A/m^2 to 260 A/m^2 for 5 ml/min (dash-dotted line), 50 ml/min (solid line) and 100 ml/min (dotted line). All three responses show overshooting. The absolute overshoot, i.e. the difference between maximum cell voltage and steady state cell voltage, slightly decreases with decreasing flow rate (from 23 mV to 18 mV). In addition, the relaxation time increases with decreasing flow rate: From 20 s for anode flow rates between 50 ml/min (τ = 22 s) and 100 ml/min (τ = 11 s) to 40 s for 5 ml/min (τ = 220 s). This may be interpreted as follows: At lower flow rates, the concentration differences within the flow field are more pronounced, leading to different local anode overpotential responses and cell current densities. Exact analysis and quantitative modelling of this effect is given in the modelling section 5.3.

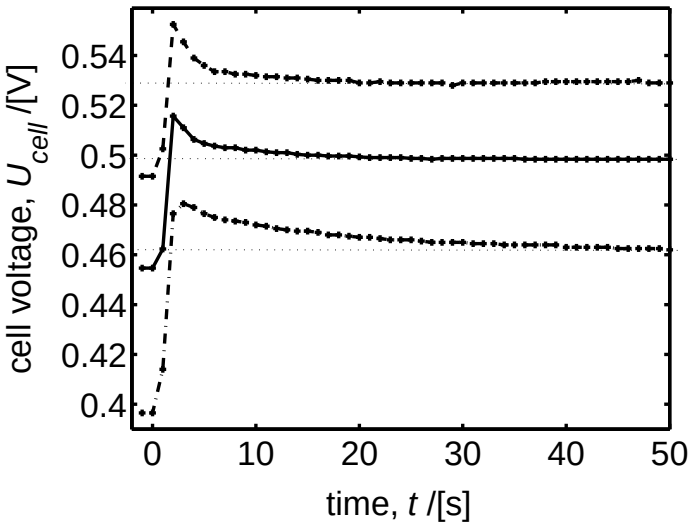

Figure 5.5: Influence of anode volume flow rate on the transient cell voltage response of the pcd-DMFC to a current density step from 520 A/m^2 to 260 A/m^2. Anode volume flow rate: 5 ml/min (dash-dotted), 50 ml/min (solid) and 100 ml/min (dashed).

Influence of Current Density Level and Step Width

The influence of a variation of the current density level and current density step width on the cell voltage response is discussed in the following. Fig. 5.6 shows the cell voltage response to smaller current density steps at the anode flow rates 50 ml/min and 100 ml/min: Step down from 520 A/m^2 to 390 A/m^2 (l.h.s.); step down from 650 A/m^2 to 520 A/m^2 (r.h.s.). As can be seen, the absolute overshoot in all cases is much lower ($\approx$ 5-10 mV) for these smaller step widths. Furthermore, the overshoots for steps from 650 A/m^2 to 520 A/m^2 are slightly lower than for steps from 520 A/m^2 to 390 A/m^2. These findings correlate with the findings for the lumped DMFC measurements (see section 2.2.3 and Fig. 2.2): Smaller current density steps cause lower overshoots, and at higher cell current density levels overshooting diminishes. An exact analysis of these phenomena is given in the modelling section (section 5.3).Finally, as for the steps from 520 A/m^2 to 260 A/m^2, no significant difference could be identified between the cell voltage responses at 50 ml/min and 100 ml/min.

It can be also observed that for both flow rates, the initial steady state cell voltage for the step down from 520 A/m^2 is higher than the cell voltage recorded 50 s after the step down to 520 A/m^2. Main reason is that the cell voltage recorded 50 s after a current density step down is still influenced by the steady state, i.e. also

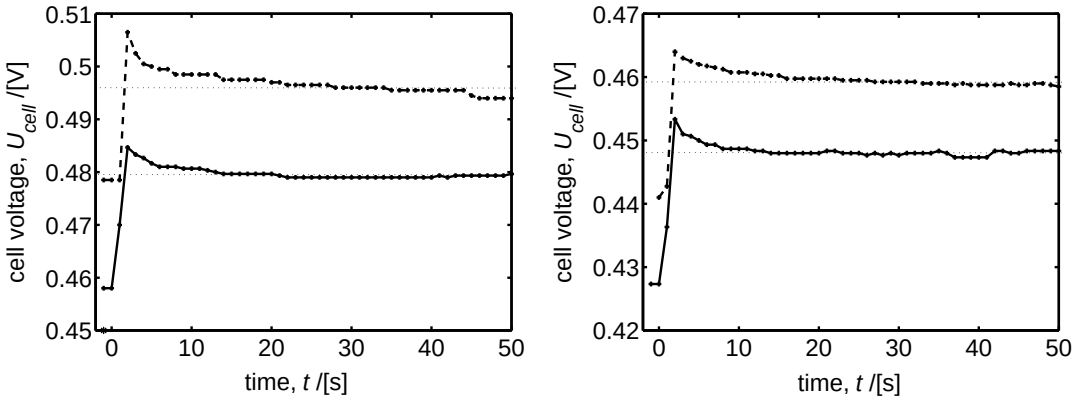

Figure 5.6: Transient cell voltage responses of the pcd-DMFC to smaller current density step downs. L.h.s.: from 520 A/m^2 to 390 A/m^2. R.h.s.: from 650 A/m^2 to 520 A/m^2. Anode Flow Rates: 50 ml/min (solid) and 100 ml/min (dashed).

by the carbon dioxide production, before the step down. The cell voltage after the step down is therefore lower than the cell voltage at initial cell current density.

5.2.2 Spot Design

Fig. 5.7 shows the polarisation curve of the DMFC with integrated spot design flow field (sd-DMFC) at an anode flow rate of 50 ml/min in comparison to the respective polarisation curve of the pcd-DMFC. Although the sd-DMFC has a more homogeneous velocity profile in the anode compartment than the pcd-DMFC, its performance is only slightly better over the whole cell current density range. While this behaviour is expected at low cell current densities due to few generation of gaseous carbon dioxide, less limitation of the polarisation curve by mass transport effects would be expected for the sd-DMFC due to its lack of zones of diminished velocity, i.e. of diminished carbon dioxide removal. The divergence between the real and the expected performance of the sd-DMFC may lie in the different properties of the actual two-phase flow and the one-phase flow investigated in the hydrodynamic measurements. As a result, carbon dioxide evolution may still lead to mass transport inhibition in some regions.

Influence of Anode Volume Flow Rate

The principle dependence of the steady state sd-DMFC performance on anode volume flow rate can be seen from Fig. 5.8, which shows cell voltage responses to the standard current density step down at 5 ml/min, 50 ml/min and 100 ml/min. The presented curves are mean values of at least two measurements, with OCV maintained for one hour between the measurements. Initial state, i.e. at 520 A/m^2, and final state, i.e. at 260 A/m^2 are evaluated. As in the pcd-DMFC, the

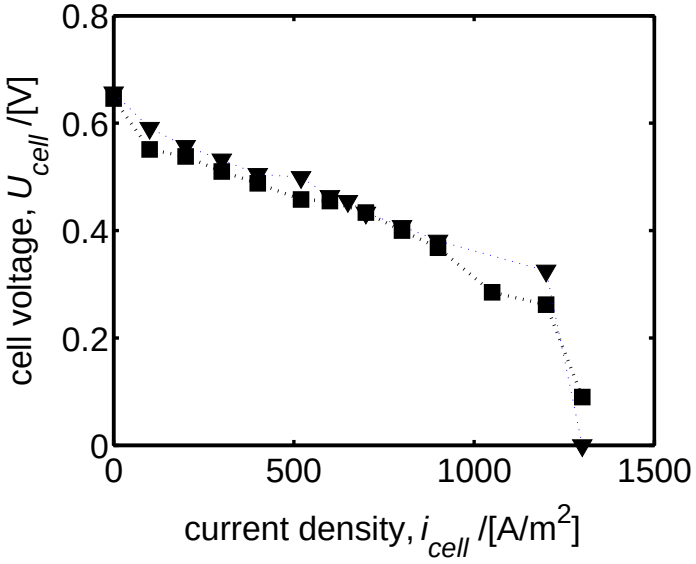

Figure 5.7: Comparison of the experimental polarisation curve of the sd-DMFC (triangles) and the pcd-DMFC (squares). Anode volume flow rate: 50 ml/min.

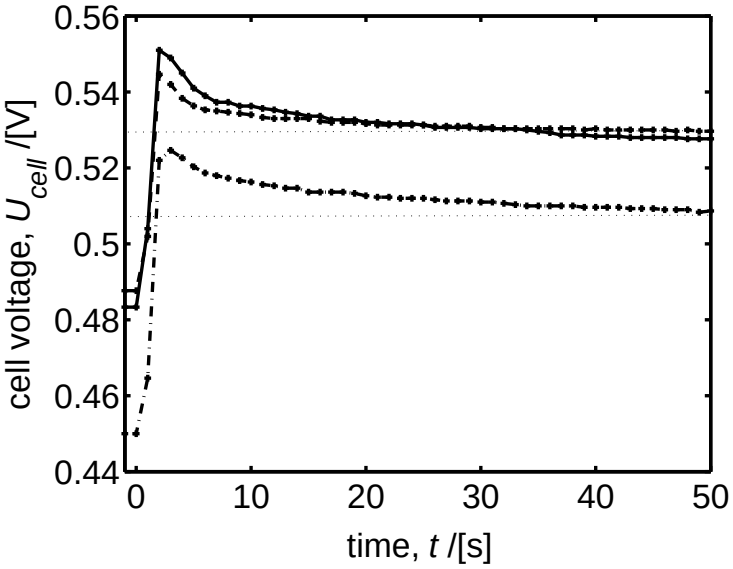

Figure 5.8: Influence of the anode volume flow rate on the transient cell voltage response of the sd-DMFC to a current density step down from 520 A/m^2 to 260 A/m^2. Anode volume flow rates: 5 ml/min (dash-dotted), 50 ml/min (solid), 100 ml/min (dashed).

steady state cell voltages at an anode volumetric flow rates of 5 ml/min (dash-dotted) are lower than at 50 ml/min (solid) and 100 ml/min (dashed). In contrast to the pcd-DMFC, the cell voltage difference between 50 ml/min and 100 ml/min is marginal. This may indicate that, at the given current densities, the influence of flow rates on gaseous carbon dioxide removal depends on flow field geometry. As discussed for the pcd-DMFC, improved carbon dioxide removal may minimise its effect on the the polarisation curve, and may eventually lead to the inverse dependence on flow rate observed in [5].

Fig. 5.8 also shows the dynamic cell voltage response to the standard current density step. The same effect as in the pcd-DMFC can be seen: The overshoot heights for all volumetric flow rates are similar, but the cell voltage is smoother and decreases slower at 5 ml/min (explanation analogue to pcd-DMFC).

Influence of Current Density Level and Step Width

Fig. 5.9 shows the mean cell voltage responses to the current density steps from 520 A/m^2 to 390 A/m^2 (dashed), and from 650 A/m^2 to 520 A/m^2 (solid). Again, the same effect is visible as in the pcd-DMFC (Fig. 5.6): Lower current density steps as well as higher cell current density levels decrease the overshoot height.

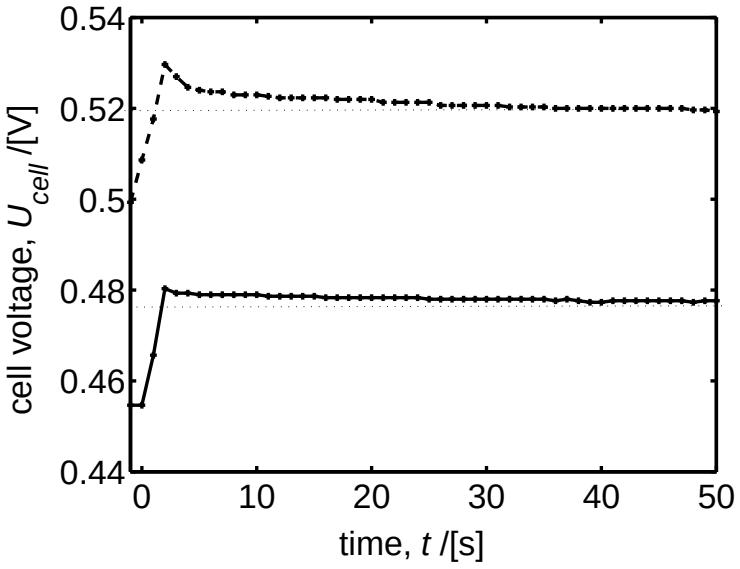

Figure 5.9: Transient cell voltage responses of the sd-DMFC to current density step downs at an anode flow rate of 50 ml/min: From 520 A/m^2 to 390 A/m^2 (dashed), from 650 A/m^2 to 520 A/m^2 (solid).

5.2.3 Rhomboidal Design

Finally, Fig. 5.10 shows the polarisation curve of the DMFC with integrated rhomboidal flow field (rd-DMFC), as well as the curves of the pcd-DMFC and the sd-DMFC. The rd-DMFC shows 50 - 70 mV lower cell voltage values, but a limiting current density similar to the pcd-DMFC and sd-DMFC. Since changes in the anode flow field geometry seem to have a negligible effect on the carbon dioxide induced limiting current, the cell break down is most probably caused by insufficient removal of carbon dioxide from the catalyst and diffusion layer.

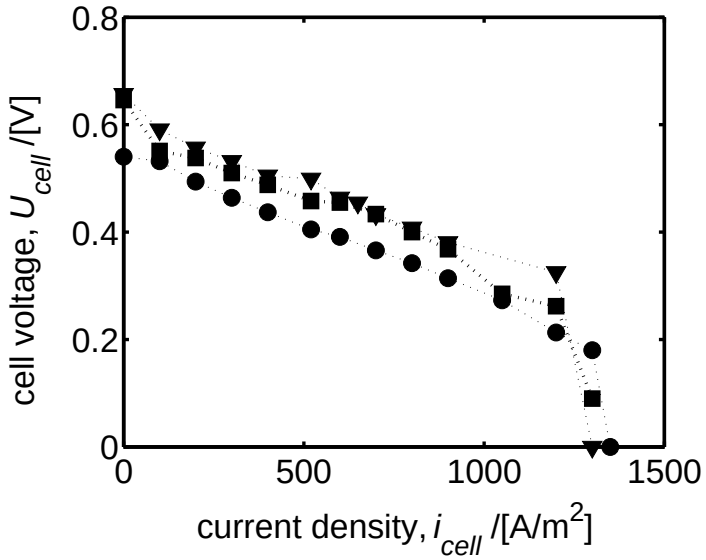

Figure 5.10: Comparison of the experimental polarisation curve of the rd-DMFC (circles) with the sd-DMFC (triangles) and pcd-DMFC (squares) curves. Anode volume flow rate: 50 ml/min.

The low cell voltages observed for the rd-DMFC, even at OCV, most probably originate from the non-optimal assembling of flow field and DMFC. The omission of a sealing in the distributor and collector areas e.g. may cause additional methanol crossover.

Influence of Anode Volume Flow Rate, Current Density Step Level and Current Density Step Width

Fig. 5.11 shows the dependence of the voltage response of the rd-DMFC on volumetric flow rate. The rd-DMFC shows a diminished cell voltage for lower anode flow rates. As in the pcd-DMFC, but in contrast to the sd-DMFC, the effect could be observed also between 50 ml/min and 100 ml/min. While the flow rate dependence of the pcd-DMFC was attributed to the influence of the inhomogeneous methanol distribution over the active area, according to the hydrodynamic

investigations, the rhomboidal design has a more homogeneous velocity profile (see 4.3). A behaviour similar to the sd-DMFC would therefore be expected. Nonetheless, pcd-DMFC and rd-DMFC have exactly the same flow field geometry at the active area, which may lead to a similarly strong influence of carbon dioxide on the flow through the flow fields.

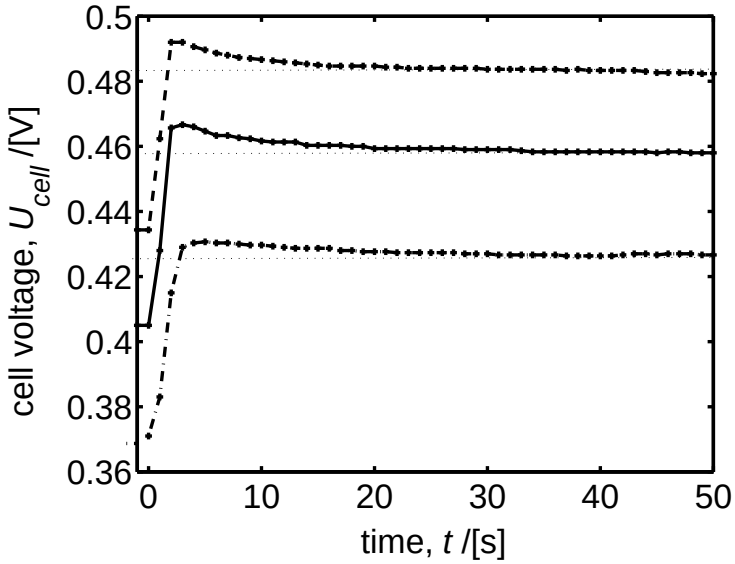

Figure 5.11: Influence of anode volume flow rate on the transient cell voltage response of the rd-DMFC to a current density step down from 520 A/m^2 to 260 A/m^2. Anode volume flow rates: 5 ml/min (dash-dotted), 50 ml/min (solid), 100 ml/min (dashed).

The dynamic responses show the same tendency as for the other designs: the cell voltage responses at 50 ml/min and 100 ml/min are similar, while the cell voltage response at 5 ml/min shows a smoother overshoot with a slower decay. In contrast to the pcd-DMFC and sd-DMFC, the overshoot heights of the rd-DMFC are smaller.

The same holds for the smaller current density steps shown in Fig. 5.12. As in the pcd-DMFC and sd-DMFC, the rd-DMFC cell voltage response for the current density step from 520 A/m^2 to 390 A/m^2 is smaller than for the standard step. Where the pcd-DMFC and sd-DMFC showed an even smaller overshoot at the higher cell current density level (650 A/m^2 to 520 A/m^2), the rd-DMFC shows no overshoot at all. A detailed analysis will be given in the following modelling section.

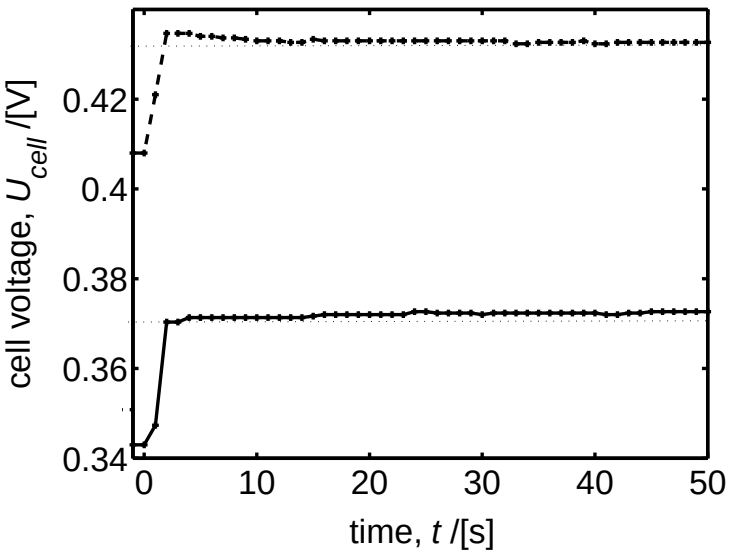

Figure 5.12: Transient cell voltage responses of the rd-DMFC to current density step downs at an anode volume flow rate of 50 ml/min: Steps from 520 A/m^2 to 390 A/m^2 (dashed), steps from 650 A/m^2 to 520 A/m^2 (solid).

5.2.4 Summary of Experimental Results

The findings of the experimental characterisation of the pcd-DMFC, sd-DMFC and rd-DMFC can be summarised as follows:

The polarisation curves of all designs were significantly influenced by limitations of the removal of gaseous carbon dioxide. Analysis indicated that these problems should be attributed to insufficient carbon dioxide removal from the anode flow field (flow rate dependence) as well as from the anode catalyst and diffusion layer (limiting current density). While there was a marginal difference between the curves of the pcd-DMFC and sd-DMFC, the rhomboidal design showed lower performance, which most probably originated from non-optimal assembling of flow field and DMFC.

For all designs, the same dependences of the dynamic behaviour on volumetric flow rate, current density level and current density step width were obtained:

- A decrease in anode volume flow rate decreases the absolute cell voltage overshoot and increases its relaxation time.

- An increase in current density level decreases the absolute cell voltage overshoot.

- A decrease in current density step width significantly decreases the absolute cell voltage overshoot.

The following section presents models that are capable of predicting the experimentally observed dynamic behaviour. Discussions of differences between experiments and simulations highlight the application area of the models.

5.3 Modelling

Section 5.2 presented the influence of three flow field designs on the experimental steady state and dynamic DMFC behaviour. Variation of the current density levels, current density step sizes and anode flow rates showed their influence on the DMFC voltage response. Furthermore, a significant influence of gaseous carbon dioxide on the DMFC behaviour was observed.
This section presents a model-based analysis of the processes involved and of the state variables governing the behaviour of the three DMFC designs (section 5.3.1). Although the DMFC models presented here do not account for any carbon dioxide evolution effects, they are able to predict the influence of the current density level and step size (section 5.3.2) as well as of anode flow rates (section 5.3.3) on the cell voltage response.

To model the steady state and dynamic behaviour of the DMFCs with different flow field designs, the hydrodynamic anode flow field models presented in section 4.4 are combined with the lumped DMFC model presented in section 3.4. To each anode flow field CSTR ij at the active area (row i and column j, grey CSTRs in Figs. 4.11, 4.14, and 4.17) a single lumped DMFC model is attributed. The combination of CSTR ij and lumped DMFC model ij is denoted as module ij. The distributor and collector CSTRs (white CSTRs in Figs. 4.11, 4.14, and 4.17) just contain the anode compartment methanol mass balances.

The following set of equations, consisting of the set of equations of the lumped DMFC model and a further balance equation describing the methanol concentration in the anode flow field CSTR ij, holds for each module ij:

$$\begin{aligned}
\frac{dc^{A,ij}_{\mathrm{CH_3OH}}}{dt} &= \frac{1}{V^{A,CSTR}} \sum_h F^{A,h} c^{A,h}_{\mathrm{CH_3OH}} - \frac{F^{A,ij}}{V^{A,CSTR}}\, c^{A,ij}_{\mathrm{CH_3OH}} \\
&\quad -\frac{k^{AD} A_S^{CSTR}}{V^{A,CSTR}} (c^{A,ij}_{\mathrm{CH_3OH}} - c^{AC,ij}_{\mathrm{CH_3OH}}) && (5.1)\\
\frac{dc^{AC,ij}_{\mathrm{CH_3OH}}}{dt} &= \frac{k^{AD} A_S^{CSTR}}{V^{AC,CSTR}} (c^{A,ij}_{\mathrm{CH_3OH}} - c^{AC,ij}_{\mathrm{CH_3OH}}) - \frac{A_S^{CSTR}}{V^{AC,CSTR}} n^{M,ij}_{\mathrm{CH_3OH}} - \frac{A_S^{CSTR}}{V^{AC,CSTR}} r^{ij}_{A1} && (5.2)\\
\frac{d\theta^{ij}_{\mathrm{CO}}}{dt} &= \frac{1}{c_{\mathrm{Pt}}} (r^{ij}_{A1} - r^{ij}_{A3}) && (5.3)\\
\frac{d\theta^{ij}_{\mathrm{OH}}}{dt} &= \frac{1}{c_{\mathrm{Ru}}} (r^{ij}_{A2} - r^{ij}_{A3}) && (5.4)\\
\frac{d\eta^{ij}_A}{dt} = 0 &= \frac{1}{C^{AC}} i^{ij}_{cell} + \frac{1}{C^{AC}} (-4F r^{ij}_{A1} - F r^{ij}_{A2} - F r^{ij}_{A3}) && (5.5)\\
\frac{d\eta^{ij}_C}{dt} = 0 &= -\frac{1}{C^{CC}} i^{ij}_{cell} - \frac{1}{C^{CC}}\, 6F r^{ij}_C - \frac{1}{C^{CC}}\, 6F n^{M,ij}_{\mathrm{CH_3OH}} && (5.6)\\
r^{ij}_{A1} &= r_{A10} \cdot \exp\left[-\beta_{\mathrm{CO}} g_{\mathrm{CO}} (\theta^{ij}_{\mathrm{CO}} - 0.5)\right] \cdot c^{AC,ij}_{\mathrm{CH_3OH}} \cdot (1 - \theta^{ij}_{\mathrm{CO}}) && (5.7)\\
r^{ij}_{A2} &= r_{A20} \cdot \exp\left[\frac{\alpha_A F}{RT} \eta^{ij}_A\right] \cdot \exp\left[-\beta_{\mathrm{OH}} g_{\mathrm{OH}} (\theta^{ij}_{\mathrm{OH}} - 0.5)\right] (1 - \theta^{ij}_{\mathrm{OH}}) \\
&\quad - r_{A-20} \cdot \exp\left[-\frac{(1-\alpha_A)F}{RT} \eta^{ij}_A\right] \cdot \exp\left[(1-\beta_{\mathrm{OH}}) g_{\mathrm{OH}} (\theta^{ij}_{\mathrm{OH}} - 0.5)\right] \theta^{ij}_{\mathrm{OH}} && (5.8)\\
r^{ij}_{A3} &= r_{A30} \cdot \exp\left[(1-\beta_{\mathrm{CO}}) g_{\mathrm{CO}} (\theta^{ij}_{\mathrm{CO}} - 0.5)\right] \theta^{ij}_{\mathrm{CO}} \cdot \theta^{ij}_{\mathrm{OH}} && (5.9)\\
r^{ij}_C &= -r_{C0} \cdot \exp\left[\frac{-(1-\alpha_C)F}{RT} \eta^{ij}_C\right] && (5.10)\\
n^{M,ij}_{\mathrm{CH_3OH}} &= \frac{D^M_{\mathrm{CH_3OH}}}{d^M}\, c^{AC,ij}_{\mathrm{CH_3OH}} && (5.11)\\
U_{cell} &= U^{\theta}_0 - \eta^{ij}_A + \eta^{ij}_C - \frac{d^M}{\kappa^M} i^{ij}_{cell} && (5.12)
\end{aligned}$$

Here, $V^{AC,CSTR}$ is the volume of the catalyst layer of module ij:

$$V^{AC,CSTR} = \frac{V^{AC}}{\text{number of active area CSTRs}}. \qquad (5.13)$$

A_S^{CSTR} is the geometric electrode area of the module's catalyst layer:

$$A_S^{CSTR} = \frac{A_S}{\text{number of active area CSTRs}}. \tag{5.14}$$

The term $\sum_h F^{A,h} c^{A,h}_{\mathrm{CH_3OH}}$ (eq. 5.1) covers all flows h entering the anode flow field CSTR ij. Its exact formulation has to be taken from the set of equations for the respective flow field design model (section 4.4). The same holds for the volumetric flow rates leaving CSTR ij. Here, only the total flow leaving CSTR ij ($F^{A,ij} \cdot c^{A,ij}_{\mathrm{CH_3OH}}$) is displayed.
The cell voltage U_{cell} for all modules is identical, and the cell currents of all modules are added to yield the total cell current $A_S\ i_{cell}$ (Kirchhoff's node law):

$$A_S\ i_{cell} = \sum_{ij} A_S^{CSTR}\ i_{cell}^{ij}. \tag{5.15}$$

In this way, all lumped DMFC model elements together constitute the membrane electrode assembly. They are electronically interconnected via eq. 5.12 and eq. 5.15.
Due to different methanol concentrations in the single modules, the local anode overpotentials η_A^{ij}, the local current densities i_{cell}^{ij} and all other state variables will be different in each module.

For all models presented in this chapter, the same set of parameters is used (Appendix B.2, pcd-DMFC): Whereas the transport and material parameters are those of the DMFC model presented in section 3.4, the original anode and cathode kinetic parameters were slightly adjusted to fit the experimental behaviour of the pcd-DMFC in the activation controlled and pseudo-Ohmic regions of the polarisation curve.

5.3.1 Basic Analysis of DMFC Behaviour

This section presents an analysis of the processes governing the behaviour of the DMFC model introduced above. The focus is on the influence of the main state variables on the DMFC's steady state and dynamic behaviour.
To give an in-depth picture of the processes inside DMFCs, instead of a complete flow field model, a model containing only two anode compartment CSTRs in series will be analysed. Both CSTRs are combined with a lumped DMFC model, respectively. The combination of the first CSTR with a DMFC model is called module 1, and the combination of the second CSTR with a DMFC model is called module 2. The model will be referred to as 2-M model. Fig. 5.13 shows its schematic structure.

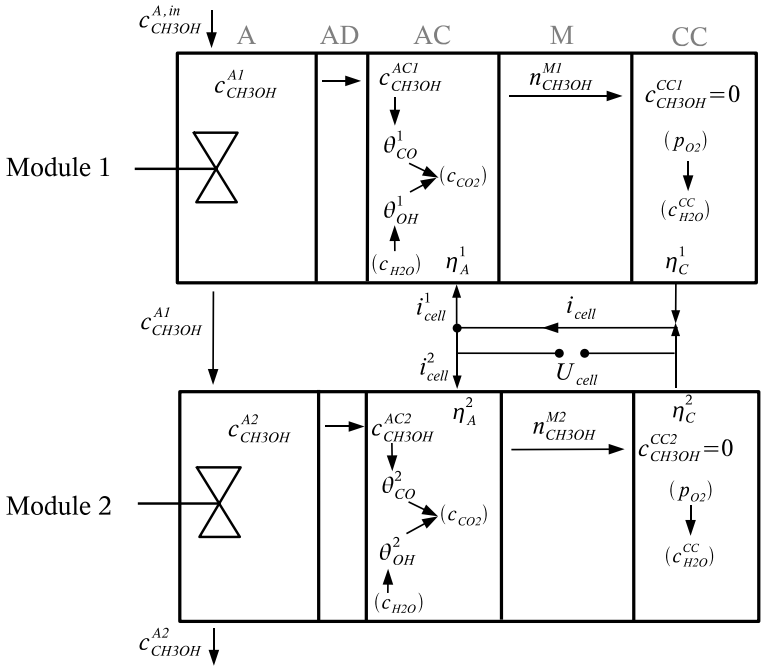

Figure 5.13: Schematic representation of the 2-M model.

The dependence of the steady state of the model variables on cell current density is illustrated in Fig. 5.14. As can be seen on the top, the cell voltage, U_{cell} (black solid) breaks down due to a steep increase of the anode overpotential η_A (black dash-dotted). This increase is caused by a kinetic limitation rather than a mass transport limitation: The methanol concentration in the anode catalyst layer $c^{AC}_{\mathrm{CH_3OH}}$ (bottom, black) is well above zero even in the limiting current density region. Nonetheless, methanol is responsible for this limitation: As can be seen in the rate equation for methanol partial oxidation (eq. 5.7), low methanol concentrations have to be compensated by lower CO surface coverage (top, grey solid and grey circles) at high cell current densities. This in turn causes the OH surface coverage (top, grey dashed and grey triangles) to increase rapidly (eq. 5.9). A rise in OH surface coverage finally leads to a direct increase in the anode overpotential (eq. 5.8) and thus to the observed cell voltage breakdown.

Fig. 5.14 also illustrates the interaction between the two modules. While the methanol concentration of the second module is always slightly lower than that of the first module, there is virtually no difference between all other state variables and local current densities of the single modules over the whole range of i_{cell}, except at high cell current densities. There, the lower methanol concentration of the second module leads to a lower local cell current density. The resulting higher i^1_{cell} in turn causes a decrease in the first module's methanol concentration, leading to similar overpotentials in both modules.

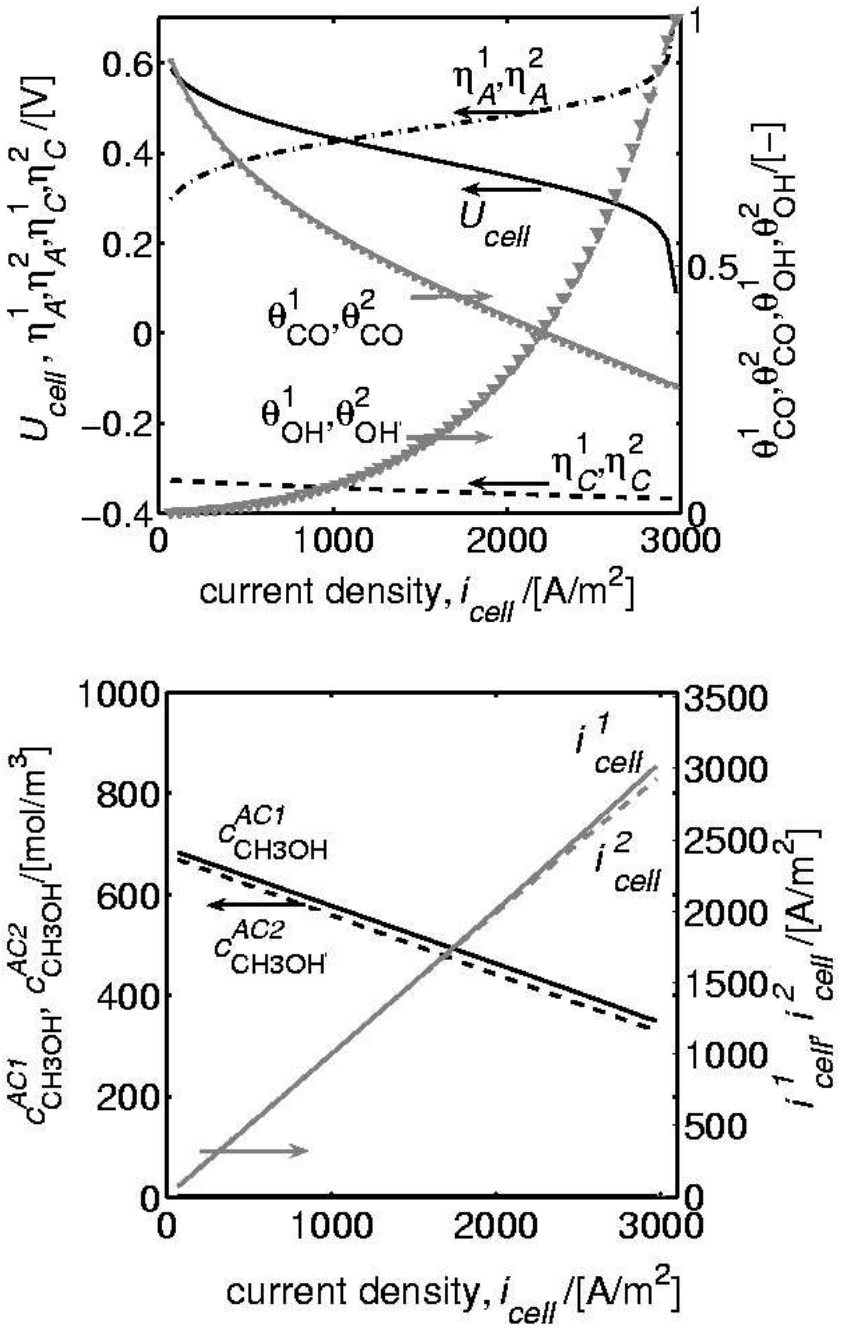

Figure 5.14: State variables of the 2-M model vs. cell current density. Top: U_{cell} (black, solid), $\eta_A^1 \approx \eta_A^2$ (black, dash-dotted), $\eta_C^1 \approx \eta_C^2$ (black, dashed), θ_{CO}^1 (grey, solid), θ_{CO}^2 (grey, circles), θ_{OH}^1 (grey, dashed), θ_{CO}^2 (grey, triangles). Bottom: $c_{\mathrm{CH_3OH}}^{AC1}$ (black, solid), $c_{\mathrm{CH_3OH}}^{AC2}$ (black, dashed), i_{cell}^1 (grey, solid) and i_{cell}^2 (grey, dashed). Anode volume flow rate: 50 ml/min.

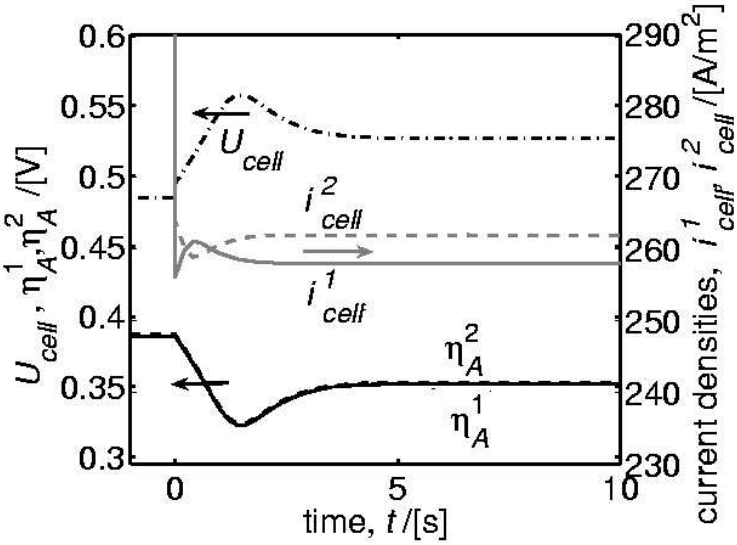

Figure 5.15: Dynamic responses of the 2-M model for the cell current density step from 520 A/m^2 to 260 A/m^2 at 50 ml/min: U_{cell} (dash-dotted), η_A^1 (solid), η_A^2 (dashed), i^1_{cell} (solid grey), i^2_{cell} (dashed grey).

Fig. 5.15 shows the dynamic behaviour of the 2-M model for the standard cell current density step from 520 A/m^2 to 260 A/m^2 at 50 ml/min. As observed also in the simulations of section 3.4, the cell voltage (dash-dotted) shows an overshoot. The cell voltage reaches its maximum two seconds after the current density step due to negative anode overpotential overshoots η_A^1 (solid) and η_A^2 (dashed). A further dynamic effect is observed: the different anode methanol concentrations and states of the two modules cause minimally different slopes for η_A^1 and η_A^2 within the first second. Since U_{cell} is identical for both modules, η_C^i as well as i^i_{cell} ($i \in \{1, 2\}$) compensate the differences between η_A^1 and η_A^2. Both i^1_{cell} (grey, solid) and i^2_{cell} (grey, dashed) show overshoots within the first second. Since the total current density of 260 A/m^2 is fixed, eq. 5.15 causes the total current densities i^1_{cell} and i^2_{cell} to be axially symmetric to each other, the axis being 260 A/m^2. They reach a steady state after two seconds, i.e. when the cell voltage reaches its maximum.

5.3.2 Influence of Current Density

The last section discussed the influence of the state variables on the steady state and dynamic behaviour of the DMFC model. In the following sections, a systematic analysis of the voltage responses of DMFCs to changes in current density

(this section) and volumetric flow rate (section 5.3.3) is presented. The role of methanol concentration on the behaviour of DMFCs will be highlighted.
While mostly, the models for the pcd-DMFC, the sd-DMFC and the rd-DMFC are used, the 2-M model is applied for basic studies.

Influence of Flow Field Design on Polarisation Curves

Fig. 5.16 shows the simulated (l.h.s.) and experimental (r.h.s.) polarisation curves of the pcd-DMFC, the sd-DMFC and the rd-DMFC at 50 ml/min. In the simulation results, no difference can be seen between the three designs, except in the limiting current region. Similar findings were obtained by the experiments of the pcd-DMFC and sd-DMFC, whereas the rd-DMFC shows a cell voltage shift attributed to assembly details (discussion see section 5.2.3). As demonstrated in this section, insensitivity of the steady state DMFC performance to methanol concentration may be the main reason for these findings. Nonetheless, analogous to section 5.2, the experimental cell performance, especially at high cell current densities, is influenced by carbon dioxide evolution: In contrast to the models, where anode kinetic limitation determines the limiting current behaviour (see section 5.3.1), the experimental limiting current densities are much lower and are most probably caused by gaseous carbon dioxide which blocks methanol transport to the catalyst area.

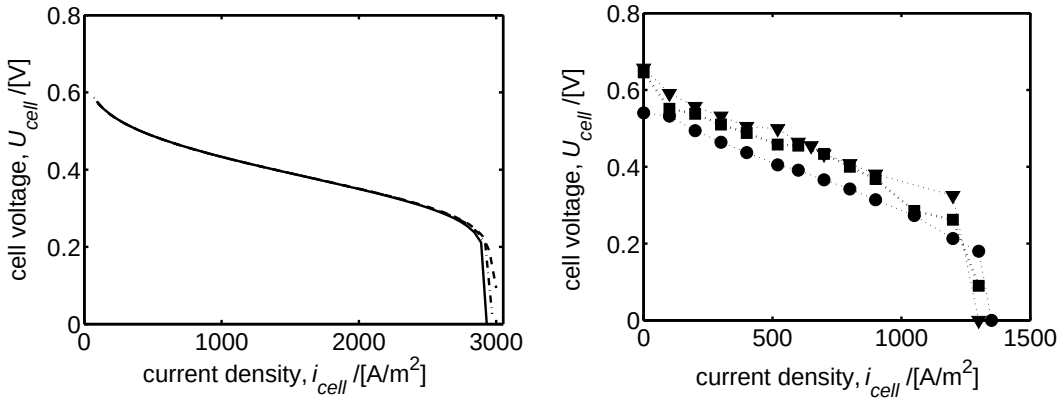

Figure 5.16: Polarisation curves of the pcd-DMFC (solid; squares), the sd-DMFC (dashed; triangles) and the rd-DMFC (dash-dotted; circles) at an anode flow rate of 50 ml/min. Simulated (l.h.s.) vs. experimental results (r.h.s.).

In the DMFC models, the limiting cell current density of the rd-DMFC is higher than that of the pcd-DMFC but lower than that of the sd-DMFC. The difference in the limiting cell current densities is attributed to a different methanol concentration distribution over the anode flow fields: While the pcd-DMFC showed

larger areas of diminished velocity, i.e. of low methanol concentration, the distribution of methanol inside the rhomboidal design was more homogeneous. The most uniform flow through the flow fields was observed in the spot design.

To show the effect of concentration distribution within the flow fields on cell current density distribution, the local methanol concentrations in the catalyst layer and the local current densities of all designs - the pcd-DMFC (top), the sd-DMFC (middle) and the rd-DMFC (bottom) - are presented in Table 5.1. The values are obtained at conditions, where methanol concentration differences over the flow field are large (i_{cell} = 520 A/m^2, $F^{A,in}$ = 2 ml/min). The sequence of the single modules is identical to the sequence of the active area CSTRs in the flow field networks in Figs. 4.11, 4.14 and 4.17.

Modules with methanol concentrations above a certain level show the following trend: lower concentrations lead to higher current densities, see e.g. modules 11 and 12 of the pcd-DMFC. This behaviour originates from methanol crossover: A lower concentration induces lower methanol crossover and a lower absolute cathode overpotential. Since the anode overpotential is insensitive to methanol concentration and since the cell voltage is the same for all modules, the cell current density rises. On the other hand, modules with low concentration levels show an inverse dependence, i.e. lower concentrations lead to lower cell current densities. This dependence should be attributed to a similar effect as the one causing cell breakdown: limitation due to anode kinetics (see section 5.3.1). The critical concentration at which the concentration influence on cell current density is inversed is similar for all three DMFC models: below 222 mol/m^3 (module 22) for the pcd-DMFC, below 230 mol/m^3 (module 32) for the sd-DMFC, and below 227 mol/m^3 (module 33) for the rd-DMFC.

Finally, an explanation for the unexpectedly small difference between the polarisation curves of the three DMFC models can be given: only at very low methanol concentrations, cell current density is significantly influenced by methanol concentration. Modules with a comparably low methanol concentration of 88 mol/m^3 (pcd-DMFC, modules 23 and 24) obtain a current density similar to that of modules with four times higher concentration (e.g. pcd-DMFC, module 11 and 16). In contrast to this, in modules with methanol concentrations of 18 mol/m^3 (pcd-DMFC, module 33 and 34), the current density has dropped to approximately half of the current density at 88 mol/m^3. This illustrates, that the influence of local methanol concentration on cell performance is negligible over a wide concentration range, whereas for very low concentrations a drastic effect on the local cell current density and on the steady state performance of a DMFC model can be observed. Hence, a significant difference in performance between the three DMFC models can only be expected in the limiting current region. There, less homogeneous flow distribution, like in the pcd-DMFC, can cause an earlier cell voltage breakdown.

Table 5.1: Local methanol concentrations in the catalyst layer and local current densities at $F^{A,in} = 2$ ml/min and $i_{cell} = 520$ A/m^2: pcd-DMFC (top), sd-DMFC (middle), rd-DMFC (bottom). Sequence of modules as in the active area CSTRs in the flow field networks in Figs. 4.11, 4.14 and 4.17.

pcd-DMFC		column j					
		1	2	3	4	5	6
$c^{AC,1j}_{CH_3OH}$	mol/m^3	512	400	284	284	400	512
i^{1j}_{cell}	A/m^2	522	549	569	569	549	522
$c^{AC,2j}_{CH_3OH}$	mol/m^3	395	222	88	88	222	395
i^{2j}_{cell}	A/m^2	550	572	515	515	572	550
$c^{AC,3j}_{CH_3OH}$	mol/m^3	296	104	18	18	104	296
i^{3j}_{cell}	A/m^2	568	532	299	299	532	568

sd-DMFC		column j		
		1	2	3
$c^{AC,1j}_{CH_3OH}$	mol/m^3	529	363	178
i^{1j}_{cell}	A/m^2	476	518	534
$c^{AC,2j}_{CH_3OH}$	mol/m^3	443	294	161
i^{2j}_{cell}	A/m^2	498	530	531
$c^{AC,3j}_{CH_3OH}$	mol/m^3	344	230	155
i^{3j}_{cell}	A/m^2	521	537	529

rd-DMFC		column j					
		1	2	3	4	5	6
$c^{AC,1j}_{CH_3OH}$	mol/m^3	426	499	479	376	352	442
i^{1j}_{cell}	A/m^2	511	493	498	523	528	507
$c^{AC,2j}_{CH_3OH}$	mol/m^3	256	370	338	188	159	280
i^{2j}_{cell}	A/m^2	543	524	531	543	537	540
$c^{AC,3j}_{CH_3OH}$	mol/m^3	137	265	227	75	53	162
i^{3j}_{cell}	A/m^2	530	542	544	479	440	538

Current Density Levels and Step Heights

Fig. 5.17 displays the principle influence of the current density level on the dynamic DMFC behaviour. Three cell voltage responses (black lines) of the 2-M model to current density step downs of 130 A/m^2 are shown: steps in the activation controlled region (dash-dotted), in the pseudo-Ohmic region (solid), and in the high current density region (dashed). The cell voltage responses differ significantly from region to region: While the cell voltage shows pronounced overshoots at low cell current densities, the overshoot is smaller in the pseudo-Ohmic region. For high cell current densities finally, no overshoot is found at all. The different responses are caused by the varying dynamics of the anode kinetics, i.e. of the anode overpotential, with current density: Low current densities induce low anode overpotentials, high methanol concentrations and overshooting OH surface coverage (grey), whereas high current densities induce low methanol concentrations, high anode potentials and no OH surface coverage overshooting (see also section 5.3.1). It can be concluded that, with increasing anode overpotential, the dynamic response of the cell voltage to cell current steps becomes less pronounced.

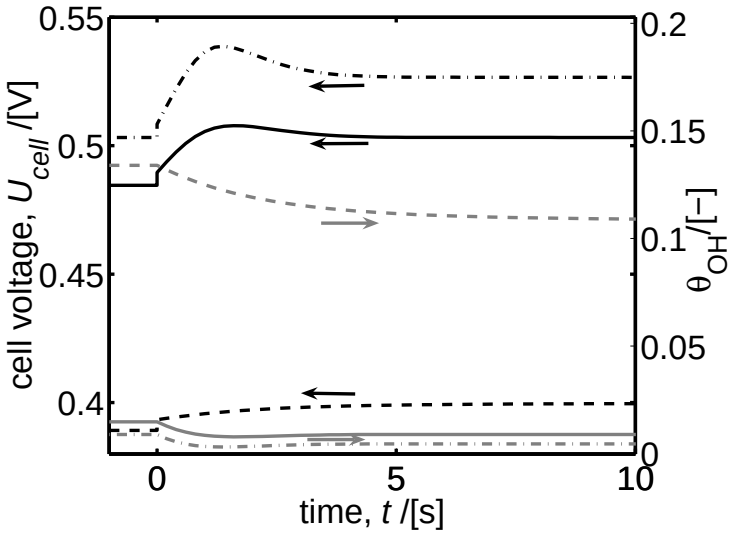

Figure 5.17: U_{cell} (black) and θ^1_{OH} (grey) response of the 2-M model at 50 ml/min and different current density levels: Step from 390 A/m^2 to 260 A/m^2 (dash-dotted), step from 520 A/m^2 to 390 A/m^2 (solid), step from 1520 A/m^2 to 1390 A/m^2 (dashed).

This behaviour has also been observed in the DMFC experiments with negligible residence time, i.e. negligible concentration differences within the anode flow field, presented in chapter 2 (see Figs. 2.3-2.5). A similar trend can be seen for the

three DMFC designs. Fig. 5.18 shows simulated (l.h.s.) and experimental (r.h.s.) cell voltage responses to current density steps of 130 A/m^2: pcd-DMFC (top), sd-DMFC (middle), rd-DMFC (bottom). All models predict a slightly smaller overshoot for current density step downs from 650 A/m^2 to 520 A/m^2 (dashed) than for steps from 520 A/m^2 to 390 A/m^2 (dash-dotted). As discussed at the beginning of section 5.3.2, the three DMFC designs do not differ significantly due to the high methanol concentration levels present at 50 ml/min. In the experiments, a less pronounced dynamics of the cell voltage response with increasing current density levels is barely visible for the pcd-DMFC, whereas it is more pronounced for the sd-DMFC and rd-DMFC. Nonetheless, the quantitative comparison of the experimental responses is error-prone, since the cell voltage measuring time step of one second is too coarse to determine the exact cell voltage response and overshoot height. It therefore can be concluded that the simulations of the pcd-DMFC and sd-DMFC predict the experimental cell voltage responses with sufficient accuracy.

In contrast to the pcd- and sd-DMFC, the experimental cell voltage responses of the rd-DMFC show only minor overshoots, if at all, within the first five seconds. These experimental results are contrary to the model predictions. The reason most probably is the non-ideality of the experimental rd-DMFC: In comparison to the experimental pcd-DMFC and sd-DMFC results, the experimental rd-DMFC results showed strongly diminished steady state cell voltages even at OCV (see also Fig. 5.16). The anode and cathode state variables most probably were in different states than the ones predicted with the rd-DMFC model, using the pcd-DMFC optimised parameter set. Furthermore, a strong dependence on volumetric flow rate for the rd-DMFC's experimental performance was observed. It was attributed to carbon dioxide influences. Both effects may cause the rd-DMFC to be in a state similar to the ones obtained e.g. at high cell current densities (Fig. 5.17), where no overshoots are obtained. This could explain the experimentally observed less dynamic cell voltage responses of the rd-DMFC.

Also presented in Fig. 5.18 is the influence of the current density step size (steps from 520 A/m^2 to 260 A/m^2 vs. steps from 520 A/m^2 to 390 A/m^2) on the dynamic DMFC response: In modelling as well as in the experiments, doubling the current density step size leads to much higher cell voltage overshoots within the first five seconds. While the experimental rd-DMFC again shows only a minor overshoot (explanation see previous paragraph) and therefore deviates from simulation, the simulations of the pcd-DMFC and sd-DMFC show accordance to the experimental results.

In-depth analysis of the shape of the cell voltage responses to steps from 520 A/m^2 to 260 A/m^2 also shows strong similarities between experiment and simulation. All simulated cell voltage responses are in a steady state after five seconds. The experimental voltages of the pcd-DMFC and the rd-DMFC also decrease rapidly

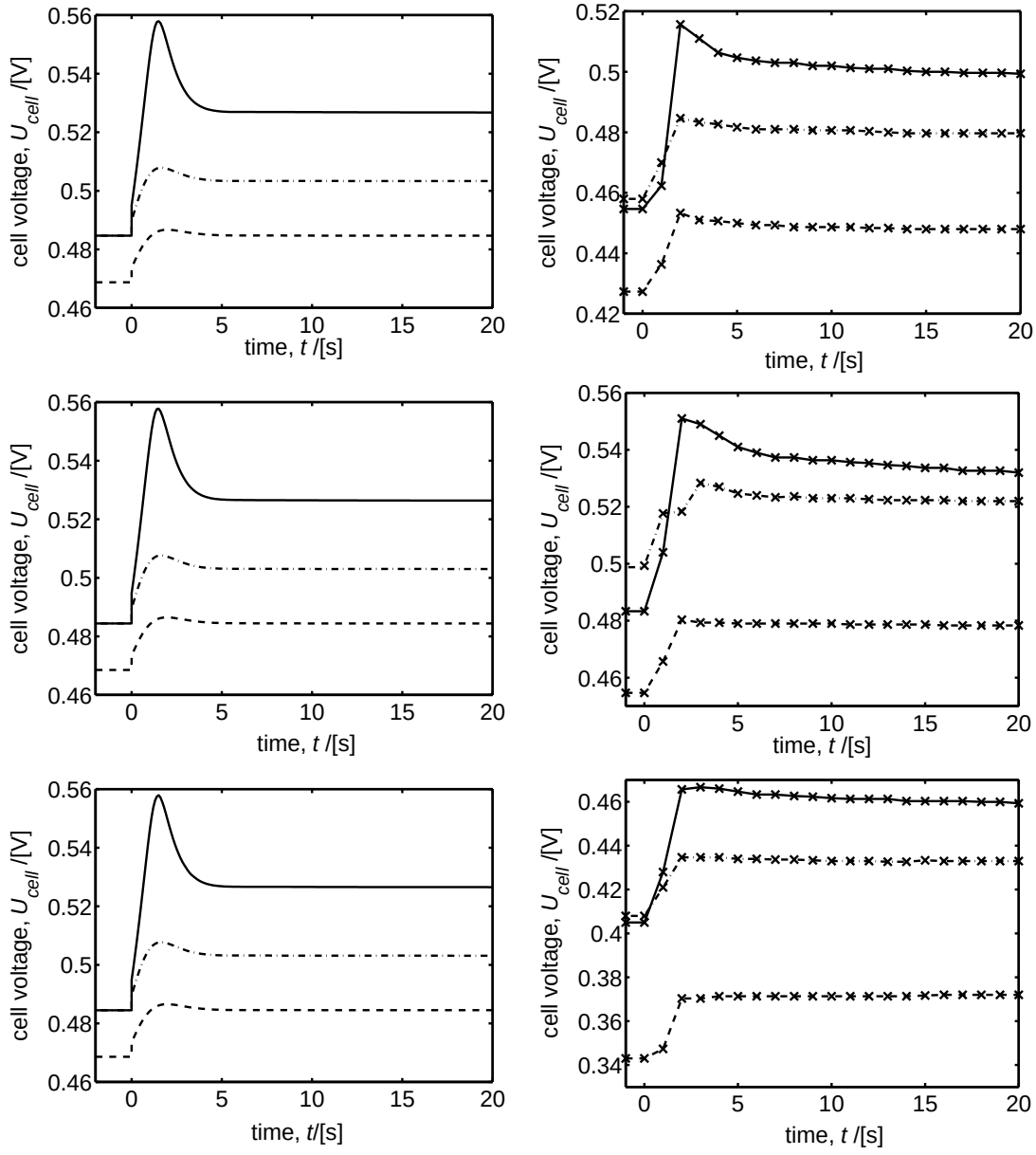

Figure 5.18: Simulated (l.h.s.) and experimental (r.h.s.) cell voltage responses to different current density steps at an anode flow rate of 50 ml/min: pcd-DMFC (top), sd-DMFC (middle), rd-DMFC (bottom). Steps from 520 A/m^2 to 260 A/m^2 (solid), from 520 A/m^2 to 390 A/m^2 (dash-dotted), and from 650 A/m^2 to 520 A/m^2 (dashed).

within the first 4-5 seconds. The only difference is, that in the experiments, this is followed by a further slow cell voltage decay due to methanol crossover effects. While the initial rapid decay is predicted correctly by the model, the dynamic

methanol crossover effect is not, due to the model assumption of a quasi-steady state methanol profile in the membrane. Inclusion of the membrane dynamics would be possible, but, as discussed in chapter 2, its effect on the cell voltage response is limited to slightly smoothing the cell voltage response. Therfore, including this phenomenon in the model would unnecessarily complicated it, as well as its analysis.

It can be concluded that the three models show the same dependence of cell voltage response on cell current density step levels and step heights as the experiments. The pcd-DMFC and rd-DMFC models can quantitatively predict overshoot height and, except for the crossover effect, also the relaxation time.

5.3.3 Influence of Anode Volume Flow Rate

Fig. 5.19 shows the simulated (l.h.s.) and experimental (r.h.s.) polarisation curves of the pcd-DMFC at different anode volume flow rates.

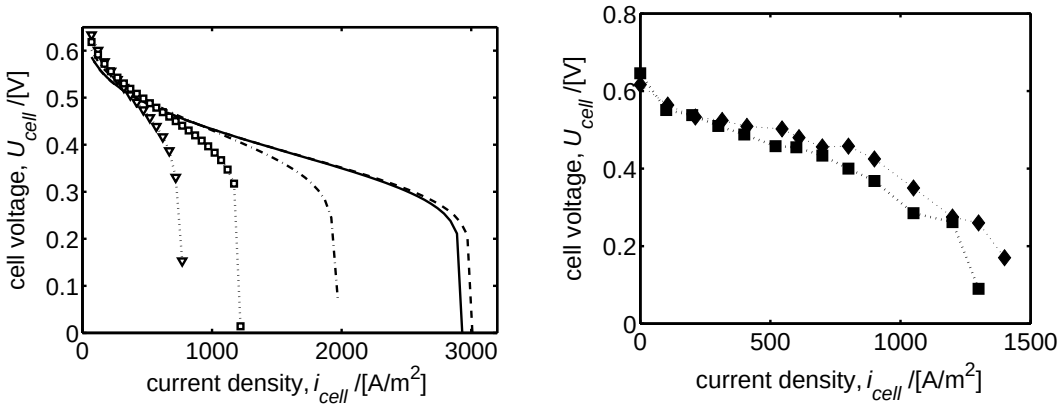

Figure 5.19: Influence of anode volume flow rate on the simulated (l.h.s.) and experimental (r.h.s.) polarisation curve of the pcd-DMFC. Anode flow rate in simulation: 1 ml/min (triangles), 2 ml/min (squares), 5 ml/min (dash-dotted), 50 ml/min (solid), 100 ml/min (dashed). Anode flow rate in experiment: 50 ml/min (squares), 100 ml/min (diamonds).

As can be seen for the simulation, the anode flow rate strongly influences the cell breakdown (limiting current behaviour) of the pcd-DMFC: The lower the anode flow rate, the lower is the limiting current. Major reason for this limitation is a decrease of methanol concentration in the flow field, i.e. in the anode catalyst layer. As discussed in section 5.3.1, a low methanol concentration leads to a limitation of the anode kinetics, and as a result to cell voltage breakdown. The same dependence of limiting current density on volumetric flow rate is observed in the experiments. But significantly lower limiting current densities are obtained

in experiments, since methanol transport towards the anode is further reduced by gaseous carbon dioxide evolution. In the experiments, carbon dioxide removal problems governs the limiting current behaviour of the cells (see also beginning of section 5.3.2).
In the activation controlled and quasi-linear region, on the other hand, all simulated curves are quite similar. Nonetheless, the simulations showed slightly higher cell voltages for the lower volume flows due to a methanol crossover effect: Lower volumetric flow rates cause lower anode methanol concentration; this induces lower methanol crossover and lower absolute cathode overpotential; since the anode overpotential is insensitive to methanol, the cell voltage rises. These model results are in accordance with the experimental results of Scott and coworkers [5]. Nonetheless, in the experimental section of the pcd-DMFC (section 5.2.1), it was presented that carbon dioxide effects, which lower the local methanol concentration, seem to cover the methanol crossover effect. As a result, the experimental polarisation curves of the pcd-DMFC (Fig. 5.19, r.h.s.) show a lower performance at lower volumetric flow rates.
The same holds for the sd-DMFC and rd-DMFC. Fig. 5.20 contains the necessary information about the principle dependence of the steady state pcd-DMFC (top), sd-DMFC (middle) and rd-DMFC (bottom) performance on anode flow rates. The figure shows the simulated (l.h.s.) and experimental (r.h.s.) cell voltage responses to the standard current density step down at various volumetric flow rates. Initial state (i_{cell}= 520 A/m^2) and final state (i_{cell} = 260 A/m^2) are evaluated. The experimental results show the (carbon dioxide induced) strong dependence of cell voltage on volumetric flow rates for the pcd-DMFC and the rd-DMFC, and the slightly lower dependence of the sd-DMFC on volumetric flow rates. A detailed discussion was already given in the experimental section 5.2. In contrast to the experiments, the simulations show an inverse influence of flow rates, which has been discussed in the previous paragraph. Since the models presented in this thesis do not cover carbon dioxide bubble evolution, they can not predict the decrease of the experimentally obtained, design specific cell voltage decrease with decreasing anode flow rate.

In contrast to the steady state investigations, the dependence of the dynamic behaviour on flow rate shows the same tendencies in experiment and simulation. At volumetric flow rates above 5 ml/min, the simulated cell voltage reaches its peak after 1-2 seconds, and a new steady state is established after 5-6 seconds. An analysis of the time constants with respect to experimental results has been presented in the discussion of Fig. 5.18. While the curves at 50 ml/min (solid) and 100 ml/min (dashed) are roughly identical, the cell voltage overshoot at 5 ml/min (dash-dotted) is slower and has a lower height. This was observed in all experiments. The models are able to predict exactly the same flow rate dependence. The difference between 5 ml/min and 50 or 100 ml/min is not caused

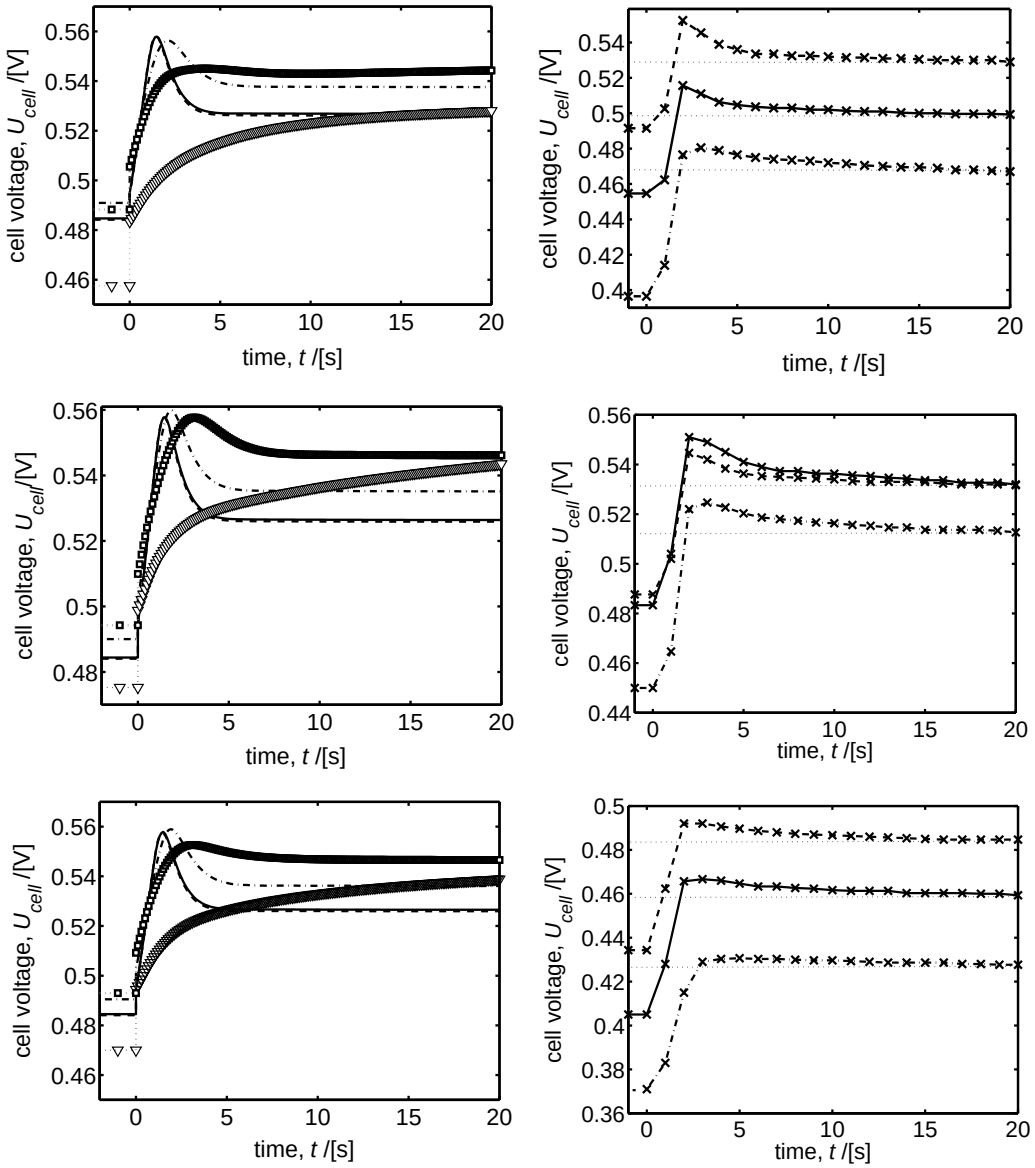

Figure 5.20: Simulated (l.h.s.) and experimental (r.h.s.) cell voltage responses to current density steps from 520 A/m^2 to 260 A/m^2: pcd-DMFC (top), sd-DMFC (middle), rd-DMFC (bottom). Anode flow rates: 1 ml/min (triangles), 2 ml/min (squares), 5 ml/min (dash-dotted), 50 ml/min (solid), 100 ml/min (dashed).

by diffusion effects, since these would have an effect only at longer time scales. Instead, it is based on the different levels of methanol concentration in the anode catalyst layer: Lower anode flow rates lower the methanol concentrations all over the flow field; the lower methanol concentrations in turn increase anode overpotentials; different anode overpotentials lead to different dynamic response of the

anode, hence of the DMFC model (detailled analysis given in next paragraph). Very low volumetric flow rates lead to further decreases of cell voltage overshooting (see simulations at 2 ml/min) and eventually to a complete disappearance of overshoots (simulations at 1 ml/min). The response to a decrease in anode flow rate is therefore comparable to that of an increase in cell current density presented in section 5.3.2.

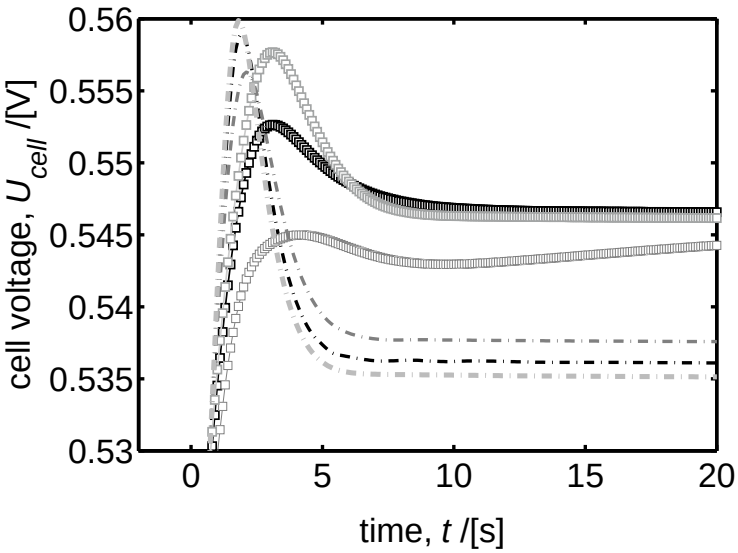

Figure 5.21: Cell voltage responses to current density steps from 520 A/m^2 to 260 A/m^2 for the three DMFC models. pcd-DMFC (grey), sd-DMFC (light grey), rd-DMFC (black). Anode flow rates: 2 ml/min (squares), 5 ml/min (dash-dotted).

Finally, Fig. 5.21 presents a comparison between the cell voltage responses of the three models for low volumetric flow rates (2 and 5 ml/min). While Fig. 5.20 illustrated the negligible differences between the designs at 50 and 100 ml/min, Fig. 5.21 highlights the differences occuring at lower volumetric flow rates. At an anode flow rate of 5 ml/min, the pcd-DMFC voltage overshoot is 7 mV smaller than the one of the sd-DMFC, while the rd-DMFC voltage overshoot is only 3 mV smaller than that of the sd-DMFC. The same trend holds for an anode flow rate of 2 ml/min. There, the deviation of the overshoot heights is even more pronounced. Obviously, the different flow field designs have a significant influence on the cell voltage response at such low volumetric flow rates.
Underlying effect is the sensitivity of the cell voltage to low local methanol concentrations: The more inhomogeneous the concentration distribution over a flow field, the higher is the probability that some of the modules have such low methanol concentrations, that the resulting high local anode overpotentials show a less pronounced dynamic behaviour. This tendency can be seen when

comparing the DMFC designs: The pcd-DMFC has the most inhomogeneous distribution of methanol and therefore shows the least dynamic behaviour, while the sd-DMFC has the most homogeneous methanol distribution and shows the strongest dynamic behaviour (distributions see Table 5.1).
The strong influence of modules with low methanol concentrations on the dynamic behaviour is also directly visible in the pcd-DMFC response at 2 ml/min: The current step down causes higher anode methanol concentrations within the whole flow field. While the concentration change barely influences most of the modules, the modules with the lowest methanol concentration (modules 33 and 34, see Table 5.1) react to the concentration increase with a decrease of local anode overpotential and an increase of local current density for more than 20 s. Since this causes a behaviour similar to the one at a volumetric flow rate of 1 ml/min (Fig. 5.20), the other local anode overpotentials are buffered. Hence, the overall cell voltage increases with time even after overshooting.

5.4 Concluding Remarks on the Characterisation of the DMFC Behaviour

This chapter presented an analysis of the influence of state variables on the dynamic and steady state behaviour of DMFCs. In addition, DMFCs with different flow field geometries were analysed.
In general, the concentration distribution of methanol inside anode flow field structures should influence the dynamic and steady-state DMFC performance. To investigate this, the flow field designs presented in chapter 4 were compared experimentally and via modelling with respect to their influence on DMFC performance. Initially, it had been suggested that designs with a more uniform velocity profile, i.e. more homogeneous concentration distribution over the active area, show better steady state performance. This suggestion could only be proven for the limiting current region in the simulations, whereas the differences between the experimental polarisation curves seemed to be more influenced by gaseous carbon dioxide, which inhibits the transport of methanol to the catalyst layer. Although the more uniform hydrodynamic velocity profiles of the spot and rhomboidal design suggested better removal of carbon dioxide, this could not be validated experimentally.
In contrast to the steady state simulations, the effect of flow field design on the dynamic behaviour of the DMFC models was more pronounced: DMFCs with regions of very low methanol concentrations showed smaller overall cell voltage overshoots. Again, in the experiments, the differences between the responses of the three designs seemed to be dominated more by carbon dioxide.
Since the steady state as well as the dynamic experimental results showed a significant influence of carbon dioxide evolution, dynamic models that are intended

to exactly predict the experimental DMFC results should consider the two-phase flow (gaseous carbon dioxide and methanol solution) inside the anode flow field and diffusion layer.
Nonetheless, the models correctly predicted the experimentally observed dependence of the dynamic behaviour of DMFCs on current density step width, current density level and anode volume flow rate. As the underlying phenomenon, a change in the dynamic behaviour of the anode was identified: The response of the anode overpotential diminishes with increasing anode overpotential levels, caused e.g. by low concentration levels or high current densities.
Finally, it can be concluded that the presented models contribute to the understanding of the dynamic behaviour of DMFCs. The results as well as the models may be useful for the development of diagnostic tools, which determine the state of DMFCs.

Chapter 6

Conclusions and Outlook

This work contributes to understanding the dynamic behaviour of direct methanol fuel cells (DMFCs). It focuses on experimental and model-based analysis of the influence of dynamic cell current changes on the cell voltage.
In a first step, cell voltage responses to cell current step changes were analysed experimentally. The voltage responses in most cases showed significant overshooting. Understanding such dynamic effects is not only essential for operation and control of DMFCs, but also for understanding the processes occurring inside the cell.
A general mathematical criterion for overshooting could be developed using linear system analysis. Models of different complexity yielded information on the relevance of the physico-chemical phenomena governing the dynamic DMFC behaviour:

- Minor influence of the dynamics of methanol storage in the membrane.
- Minor influence of cathode and anode double layer charging/discharging.
- Significant effect of the reaction kinetics of methanol oxidation.

Application of a simple, two step methanol oxidation mechanism could generate absolute overshoots of 10 % of the experimentally observed values. The underlying phenomenon was the influence of changes in the anode methanol concentration on the methanol transport to the cathode, and therefore on the cathode overpotential.
The significant dependence of DMFC models on the methanol oxidation kinetics motivated an in-depth analysis of the anode reaction kinetics. The kinetics of methanol oxidation was studied experimentally at half cells using electrochemical impedance spectroscopy. The results were compared to simulations using various reaction kinetic formulations, and a kinetics was identified that is able to adequately predict the methanol oxidation experiments, and after integration into a DMFC model, also the experimentally observed dynamic behaviour of DMFCs.

Typically, DMFCs are operated at low anode volume flow rates to increase the system efficiency. Low anode flow rates in turn lead to distinct methanol con-

centration differences within anode flow fields. To identify their influence on the DMFC performance, the hydrodynamic behaviour of three anode flow field designs was experimentally characterised and modelled using networks of ideally mixed reactors. Although the analysis identified large concentration differences over the active area for some designs, all DMFC model responses as well as the experimental cell voltage responses of two designs showed similar dynamic behaviour at medium to high anode flow rates. Model analysis attributed these results to the high insensitivity of the cell voltage to methanol concentration changes at high and moderate concentration levels. The DMFC models were also able to predict the experimentally observed dependences of the dynamic DMFC response on process parameters like current density and anode flow rate. They identified the state of the anode catalyst layer as the main governing factor.
Nonetheless, comparison of experiment and simulation also suggested a significant influence of gaseous carbon dioxide on the cell behaviour for all designs. This effect can be crucial for exact model predictions of the steady state and dynamic behaviour of DMFCs. Extending the presented DMFC models with the influence of gaseous carbon dioxide on methanol transport should therefore be the next decisive step to a complete understanding of the dynamic behaviour of the DMFC.

The models presented in this thesis are reduced models which are valid for the activation controlled and pseudo-Ohmic regions of the DMFC polarisation curve. They can be easily extended or adapted to different DMFC designs or DMFC stacks. The models as well as the results obtained can be applied in various fields, ranging from research and development to industrial application. Diagnostic tools for the state of a given DMFC, and controller design are among the possible options.
The models are a potential basis for DMFC controller design due to their short simulation times. The design of reliable controllers is essential especially if DMFCs are to be used without or with minimised additional buffers, like a battery or supercapacitor. Nevertheless, the investigations given here also show that the effect of overshooting cell voltage may not be easily eliminated or used for improving the cell performance: The cell voltage overshooting is mainly determined by the anode reaction kinetics, i.e. by the interaction between the fast water decomposition and the slow decomposition of methanol and intermediates.

Appendix A

Experimental

A.1 Calibration of Eosin

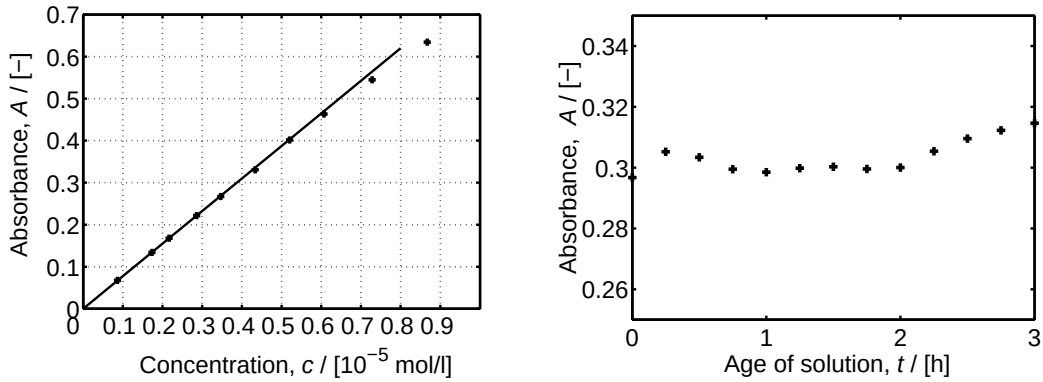

Figure A.1: UV-Vis calibration curve of eosin (l.h.s.) and time stability of eosin at approx. $5 \cdot 10^{-6}$ mol/l (r.h.s.). Wavelength $\lambda = 515$ nm.

Fig. A.1 shows the eosin UV-Vis calibration curve and the time stability curve of eosin at 515 nm. Probe length was 1 cm. Linearity between absorbance and concentration of eosin (Lambert-Beer law) is valid up to a concentration of $5.5 \cdot 10^{-6}$ mol/l. Therefore, all measurements presented in section 4.3 were conducted at a lower concentration ($\approx 5 \cdot 10^{-6}$ mol/l). The time stability curve on the right hand side shows that the absorbance is sufficiently stable 0.5 - 2.0 hours after preparation of an eosin solution. The measurements were conducted within this time span.

A.2 Procedure of Video Processing

For characterising the hydrodynamic behaviour of the anode flow fields presented in chapter 4, the concentration distribution of eosin inside the anode flow fields was recorded with a camera during residence time measurements. Due to the low eosin concentration (see Appendix A.1), the contrast between the reddish tracer flow and water was barely visible. To produce false colour videos that show amplified contrasts (snapshots presented in section 4.3), a video processing algorithm was developed.
Pictures considered for the algorithm are:

- All single pictures (snapshots) of a recorded video.
- A reference picture: Snapshot recorded at time t $\approx$ 0 s, i.e. when the flow field contains no tracer.
- A mask picture: Snapshot where the inner flow field geometry, i.e. the region to be investigated, is filled with black colour pixels.

The single pictures were processed one by one. In a first step, a picture, its two neighbouring pictures, a mask picture and a reference picture are read. For every pixel of a picture, the following procedure is applied:

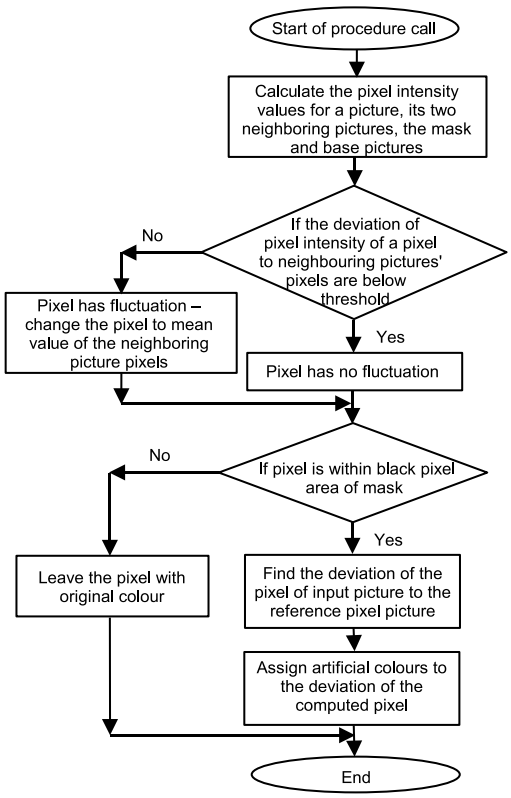

Since a higher eosin concentration leads to a higher red value of a pixel, the red intensity of each pixel in the evaluated picture is computed. The same holds for the two neighboring pictures, the mask picture and the base picture.
Each red intensity R_i of a pixel i is computed using its rgb values (r=red, g=green, b=blue):

$$R_i = r_i - g_i - b_i \tag{A.1}$$

The recorded pictures partly showed fluctuating pixel intensities R_i when comparing to the neighbouring pictures's pixels (previous picture's pixel: R_i^-, subsequent picture's pixel: R_i^+). To avoid such disturbances, a smoothing procedure is applied to pixels with fluctuating intensities:
Pixel i is fluctuating if $|R_i - R_i^+| \geq 10$ or $|R_i - R_i^-| \geq 10$. In this case, an arithmetic mean of the neighbouring pictures' intensities is taken as the pixel's intensity:

$$R_i = \frac{R_i^- + R_i^+}{2} \tag{A.2}$$

In a further step, each pixel in the evaluated area (black area in mask picture) is corrected for the intensity of the respective pixel of the reference picture R_i^{ref}. This yields the change in colour of pixel i, R_i^{corr}, and hence poses a measure for the local tracer concentration:

$$R_i^{corr} = R_i - R_i^{ref} \tag{A.3}$$

Finally, depending on a pixel's corrected intensity value, an artificial colour C_i is attributed to the evaluated pixel i:

$$C_i = \begin{cases} \text{original} & : & R_i^{corr} \leq 17 \\ \text{yellow} & : & 17 < R_i^{corr} \leq 30 \\ \text{red} & : & 30 < R_i^{corr} \leq 32 \\ \text{blue} & : & R_i^{corr} > 32 \end{cases} \tag{A.4}$$

The pixels outside the evaluated area retain their original colour.
The presented procedure is repeated for every pixel in all recorded snapshots.

Appendix B

Modelling

B.1 Transfer Functions and Further Functions of Section 2.3

B.1.1 1x-model

The following transfer functions hold for the 1x-model presented in section 2.3.3. In- and outputs are in the same order, from top to bottom, as in the block diagram in Fig. 2.9 (l.h.s.):

$$G_{AC}(s) = \begin{pmatrix} \frac{-A_s/V^{AC}}{s+k^{AD}A_s/V^{AC}+A_s/V^{AC}r_{A10}\exp\left(\frac{\alpha_{A1}F}{RT}\eta_{A,ss}\right)/c^{ref}_{\mathrm{CH_3OH}}} \\ \frac{-A_s/V^{AC}r_{A10}\alpha_{A1}F/R/T\exp\left(\frac{\alpha_{A1}F}{RT}\eta_{A,ss}\right)c^{AC}_{\mathrm{CH_3OH},ss}/c^{ref}_{\mathrm{CH_3OH}}}{s+k^{AD}A_s/V^{AC}+A_s/V^{AC}r_{A10}\exp\left(\frac{\alpha_{A1}F}{RT}\eta_{A,ss}\right)/c^{ref}_{\mathrm{CH_3OH}}} \end{pmatrix}^T \tag{B.1}$$

$$G_{AE}(s) = \begin{pmatrix} -\frac{RT}{\alpha_{A1}Fc^{AC}_{\mathrm{CH_3OH},ss}}, & \frac{RT}{\alpha_{A1}Fi_{cell,ss}} \end{pmatrix} \tag{B.2}$$

$$G_M = \begin{pmatrix} 0, & D^M_{\mathrm{CH_3OH}}/d^M \\ d^M/\kappa^M, & 0 \\ 0, & D^M_{\mathrm{CH_3OH}}/d^M \end{pmatrix} \tag{B.3}$$

$$G_C = \begin{pmatrix} \frac{RT}{F(i_{cell,ss}+6Fn^{MC}_{\mathrm{CH_3OH},ss})(\alpha_C-1)}, & \frac{6RT}{(i_{cell,ss}+6Fn^{MC}_{\mathrm{CH_3OH},ss})(\alpha_C-1)} \end{pmatrix} \tag{B.4}$$

B.1.2 2x-model

The following transfer functions hold for the 2x-model presented in section 2.3.4. G_C and G_M are identical to the ones in the 1x-model (section B.1.1). Due to the new state variable $\theta_{\mathrm{CO}x}$, the transfer functions for the anode (in- and outputs are in the same order as in Fig. 2.9) change as follows:

$G_{AC}(s) =$

$$\begin{pmatrix} \frac{-A_s/V^{AC}}{s+k^{AD}A_s/V^{AC}+A_s/V^{AC}r_{A10}\exp\left(\frac{\alpha_A F}{RT}\eta_{A,ss}\right)\frac{(1-\theta_{\mathrm{CO}x,ss})}{(1-\theta^{ref}_{\mathrm{CO}x})c^{ref}_{\mathrm{CH_3OH}}}} \\ \frac{A_s/V^{AC}r_{A10}\exp\left(\frac{\alpha_A F}{RT}\eta_{A,ss}\right)\frac{c^{AC}_{\mathrm{CH_3OH},ss}}{c^{ref}_{\mathrm{CH_3OH}}(1-\theta^{ref}_{\mathrm{CO}x})}}{s+k^{AD}A_s/V^{AC}+A_s/V^{AC}r_{A10}\exp\left(\frac{\alpha_A F}{RT}\eta_{A,ss}\right)\frac{(1-\theta_{\mathrm{CO}x,ss})}{(1-\theta^{ref}_{\mathrm{CO}x})c^{ref}_{\mathrm{CH_3OH}}}} \\ \frac{-A_s/V^{AC}r_{A10}\frac{\alpha_A F}{RT}\exp\left(\frac{\alpha_A F}{RT}\eta_{A,ss}\right)\frac{c^{AC}_{\mathrm{CH_3OH},ss}(1-\theta_{\mathrm{CO}x,ss})}{c^{ref}_{\mathrm{CH_3OH}}(1-\theta^{ref}_{\mathrm{CO}x})}}{s+k^{AD}A_s/V^{AC}+A_s/V^{AC}r_{A10}\exp\left(\frac{\alpha_A F}{RT}\eta_{A,ss}\right)\frac{(1-\theta_{\mathrm{CO}x,ss})}{(1-\theta^{ref}_{\mathrm{CO}x})c^{ref}_{\mathrm{CH_3OH}}}} \end{pmatrix}^T \tag{B.5}$$

$G_{AT}(s) =$

$$\begin{pmatrix} \frac{\frac{\alpha_A F}{RT}\exp\left(\frac{\alpha_A F}{RT}\eta_{A,ss}\right)/c_{max,Pt}\left(r_{A10}\frac{c^{AC}_{\mathrm{CH_3OH},ss}(1-\theta_{\mathrm{CO}x,ss})}{c^{ref}_{\mathrm{CH_3OH}}(1-\theta^{ref}_{\mathrm{CO}x})}-r_{A20}\frac{\theta_{\mathrm{CO}x,ss}}{\theta^{ref}_{\mathrm{CO}x}}\right)}{s-1/c_{max,Pt}\left(-r_{A10}\exp\left(\frac{\alpha_A F}{RT}\eta_{A,ss}\right)\frac{c^{AC}_{\mathrm{CH_3OH},ss}}{c^{ref}_{\mathrm{CH_3OH}}(1-\theta^{ref}_{\mathrm{CO}x,ss})}-r_{A20}\exp\left(\frac{\alpha_A F}{RT}\eta_{A,ss}\right)/\theta^{ref}_{\mathrm{CO}x}\right)} \\ \frac{r_{A10}\exp\left(\frac{\alpha_A F}{RT}\eta_{A,ss}\right)\frac{(1-\theta_{\mathrm{CO}x,ss})}{c^{ref}_{\mathrm{CH_3OH}}(1-\theta^{ref}_{\mathrm{CO}x})}/c_{max,Pt}}{s-1/c_{max,Pt}\left(-r_{A10}\exp\left(\frac{\alpha_A F}{RT}\eta_{A,ss}\right)\frac{c^{AC}_{\mathrm{CH_3OH},ss}}{c^{ref}_{\mathrm{CH_3OH}}(1-\theta^{ref}_{\mathrm{CO}x,ss})}-r_{A20}\exp\left(\frac{\alpha_A F}{RT}\eta_{A,ss}\right)/\theta^{ref}_{\mathrm{CO}x}\right)} \end{pmatrix}^T \tag{B.6}$$

$G_{AE} =$

$$\begin{pmatrix} \frac{2RTr_{A10}\theta^{ref}_{\mathrm{CO}x}(1-\theta_{\mathrm{CO}x,ss})}{(2r_{A10}c^{AC}_{\mathrm{CH_3OH},ss}\theta^{ref}_{\mathrm{CO}x}(\theta_{\mathrm{CO}x,ss}-1)+r_{A20}\theta_{\mathrm{CO}x,ss}c^{ref}_{\mathrm{CH_3OH}}(\theta^{ref}_{\mathrm{CO}x,ss}-1))\alpha_A F} \\ \frac{-RT(2r_{A10}c^{AC}_{\mathrm{CH_3OH},ss}\theta^{ref}_{\mathrm{CO}x}+r_{A20}c^{ref}_{\mathrm{CH_3OH}}(\theta^{ref}_{\mathrm{CO}x}-1)}{(2r_{A10}c^{AC}_{\mathrm{CH_3OH},ss}\theta^{ref}_{\mathrm{CO}x}(\theta_{\mathrm{CO}x,ss}-1)+r_{A20}\theta_{\mathrm{CO}x,ss}c^{ref}_{\mathrm{CH_3OH}}(\theta^{ref}_{\mathrm{CO}x}-1))\alpha_A F} \\ \frac{RT}{\alpha_A F i_{cell,ss}} \end{pmatrix}^T, \tag{B.7}$$

The anode charge transfer coefficients are assumed to be identical ($\alpha_A = \alpha_{A1} = \alpha_{A2}$).

B.1.3 2x+m-model

The functions $b_1(s,z)$ and $b_2(s,z)$ of the Laplace transformed methanol mass flow (eq. 2.44) are:

$$\begin{aligned} b_1(s,z) &= \frac{\exp(Pe_{ss}z/2d^M)}{\sinh(a(s))} \cdot \left[\frac{2a(s)D^M_{\mathrm{CH_3OH}} \cosh(a(s)(1-z/d^M))}{2d^M} + \right. \\ & \left. \frac{(-D^M_{\mathrm{CH_3OH}} Pe_{ss} + 2d^M k_{\phi 2} i_{cell,ss}) \sinh(a(s)(1-z/d^M))}{2d^M} \right] \end{aligned} \tag{B.8}$$

and

$$\begin{aligned} b_2(s,z) &= \frac{k_{\phi 2} \cdot c^{AC}_{\mathrm{CH_3OH}}(1-\exp(-Pe_{ss}(1-z/d^M)))}{1-\exp(-Pe_{ss})} + \frac{k^2_{\phi 2} \cdot c^{AC}_{\mathrm{CH_3OH}} \exp(-Pe_{ss}) i_{cell,ss}}{(1-\exp(-Pe_{ss}))D^M_{\mathrm{CH_3OH}} s} \cdot \\ & \cdot \left(-\exp(Pe_{ss}z/d^M)\frac{Pe_{ss}}{d^M} - \frac{\exp((-a(s)+Pe_{ss}/2)\cdot z/d^M)}{-\exp(-a(s)+Pe_{ss}/2)+\exp(a(s)+Pe_{ss}/2)} \cdot \right. \\ & \quad \cdot(-a(s)+Pe_{ss}/2)\cdot(-\exp(a(s)+Pe_{ss}/2)+\exp(Pe_{ss})) \\ & \quad - \frac{\exp((a(s)+Pe_{ss}/2)\cdot z/d^M)\cdot(\exp(-a(s)+Pe_{ss}/2)-\exp(Pe_{ss}))}{-\exp(-a(s)+Pe_{ss}/2)+\exp(a(s)+Pe_{ss}/2)} \cdot \\ & \left. \cdot\frac{(a(s)+Pe_{ss}/2)}{1} \right) + \frac{k^3_{\phi 2} \cdot c^{AC}_{\mathrm{CH_3OH}} \exp(-Pe_{ss}) i^2_{cell,ss}}{(1-\exp(-Pe_{ss}))D \cdot s} \cdot \\ & \cdot \left(\exp(Pe_{ss}z/d^M) + \frac{\exp((a(s)+Pe_{ss}/2)\cdot z/d^M)}{-\exp(-a(s)+Pe_{ss}/2)+\exp(a(s)+Pe_{ss}/2)} \cdot \right. \\ & \quad \cdot(\exp(-a(s)+Pe_{ss}/2)-\exp(Pe_{ss})) \\ & \quad \left. + \frac{\exp((-a(s)+Pe_{ss}/2)\cdot z/d^M)\cdot(-\exp(a(s)+Pe_{ss}/2)+\exp(Pe_{ss}))}{-\exp(-a(s)+Pe_{ss}/2)+\exp(a(s)+Pe_{ss}/2)} \right) \end{aligned} \tag{B.9}$$

with

$$a(s) = \sqrt{(\frac{Pe_{ss}}{2})^2 + \frac{(d^M)^2}{D^M_{\mathrm{CH_3OH}}} s} \tag{B.10}$$

B.1.4 4x-model

The following transfer functions hold for the 4x-model presented in (section 2.3.7). In- and outputs are in the same order, from top to bottom, as in the block diagram in Fig. 2.9 (l.h.s.). $G_{AC}(s)$, $G_{AT}(s)$ and G_M are identical to the ones of the 2x-model (see section B.1.2). The transfer function elements for anode and cathode charge, $G_{AE}(s)$ and $G_C(s)$ have changed to:

$G_{AE}(s) =$

$$\begin{pmatrix} -\dfrac{4Fr_{A10}\exp\left(\frac{\alpha_A F}{RT}\eta_{A,ss}\right)\frac{(1-\theta_{\mathrm{CO}x,ss})}{c^{ref}_{\mathrm{CH_3OH}}(1-\theta^{ref}_{\mathrm{CO}x})}/C^{AC}}{s-\frac{\alpha_A}{RT}\exp\left(\frac{\alpha_A F}{RT}\eta_{A,ss}\right)\left(-4F^2r_{A10}\frac{c^{AC}_{\mathrm{CH_3OH},ss}(1-\theta_{\mathrm{CO}x,ss})}{c^{ref}_{\mathrm{CH_3OH}}\left(1-\theta^{ref}_{\mathrm{CO}x}\right)}-2F^2r_{A20}\frac{\theta_{\mathrm{CO}x,ss}}{\theta^{ref}_{\mathrm{CO}x}}\right)/C^{AC}} \\ \dfrac{\left(4Fr_{A10}\exp\left(\frac{\alpha_A F}{RT}\eta_{A,ss}\right)\frac{c^{AC}_{\mathrm{CH_3OH},ss}}{c^{ref}_{\mathrm{CH_3OH}}(1-\theta^{ref}_{\mathrm{CO}x})}-2Fr_{A20}\exp\left(\frac{\alpha_A F}{RT}\eta_{A,ss}\right)/\theta^{ref}_{\mathrm{CO}x}\right)/C^{AC}}{s-\frac{\alpha_A}{RT}\exp\left(\frac{\alpha_A F}{RT}\eta_{A,ss}\right)\left(-4F^2r_{A10}\frac{c^{AC}_{\mathrm{CH_3OH},ss}(1-\theta_{\mathrm{CO}x,ss})}{c^{ref}_{\mathrm{CH_3OH}}\left(1-\theta^{ref}_{\mathrm{CO}x}\right)}-2F^2r_{A20}\frac{\theta_{\mathrm{CO}x,ss}}{\theta^{ref}_{\mathrm{CO}x}}\right)/C^{AC}} \\ \dfrac{1/C^{AC}}{s-\frac{\alpha_A}{RT}\exp\left(\frac{\alpha_A F}{RT}\eta_{A,ss}\right)\left(-4F^2r_{A10}\frac{c^{AC}_{\mathrm{CH_3OH},ss}(1-\theta_{\mathrm{CO}x,ss})}{c^{ref}_{\mathrm{CH_3OH}}\left(1-\theta^{ref}_{\mathrm{CO}x}\right)}-2F^2r_{A20}\frac{\theta_{\mathrm{CO}x,ss}}{\theta^{ref}_{\mathrm{CO}x}}\right)/C^{AC}} \end{pmatrix}^T \tag{B.11}$$

$$G_C(s) = \begin{pmatrix} -\dfrac{1/C^{CC}}{s+6/C^{CC}F^2r_{C0}\frac{(1-\alpha_C)}{RT}\exp\left(-\frac{(1-\alpha_C)F}{RT}\eta_{C,ss}\right)} \\ -\dfrac{6F/C^{CC}}{s+6/C^{CC}F^2r_{C0}\frac{(1-\alpha_C)}{RT}\exp\left(-\frac{(1-\alpha_C)F}{RT}\eta_{C,ss}\right)} \end{pmatrix}^T \tag{B.12}$$

B.2 Tables of Model Parameters

Table B.1: Parameter sets of the DMFC models of chapters 2 and 5.

Parameter	1x-model	2x-model	2x+m-model	4x-model	pcd-DMFC
A_S, 10^4 m^2	26	26	26	26	100
d^{AC}, 10^6 m	35	35	35	35	35
d^{AD}, 10^6 m	170	170	170	170	170
d^{M}, 10^6 m	100	100	100	100	100
V^{AC}, 10^9 m^3	9.1	9.1	9.1	9.1	35
c_{Pt}, mol/m^2	-	-	-	-	0.011
c_{Ru}, mol/m^2	-	-	-	-	0.121
$c_{\mathrm{max,Pt}}$, mol/m^2	-	0.11	0.11	0.11	-
C^{AC}, C/m^2	-	-	-	1827	-
C^{CC}, C/m^2	-	-	-	907	-
$c^{A}_{\mathrm{CH_3OH}}$, mol/m^3	1000	1000	1000	1000	1000
$c^{ref}_{\mathrm{CH_3OH}}$, mol/m^3	1000	1000	1000	1000	-
$D_{\mathrm{CH_3OH}}$, 10^9 m^2/s	3.187	3.187	3.187	3.187	3.187
$D^{M}_{\mathrm{CH_3OH}}$, 10^9 m^2/s	0.47	0.47	0.47	0.47	0.47
$D^{M}_{H^+}$, 10^9 m^2/s	4.5	4.5	4.5	4.5	4.5
k_{AD}, 10^5 m/s	1.12	1.12	1.12	1.12	1.12
$k_{\phi 2}$, 10^3 m^3/C	-	-	1.33	-	-
κ^{M}, 1/Ω/m	0.0873	0.0873	0.0873	0.0873	0.0873
r_{A10}, mol/m^2/s	1.4 (1) $\cdot 10^{-7}$	10^{-6}	10^{-6}	10^{-6}	-
, m/s	-	-	-	-	$8.75 \cdot 10^{-6}$
r_{A20}, mol/m^2/s	-	$5 \cdot 10^{-8}$	$5 \cdot 10^{-8}$	$5 \cdot 10^{-8}$	$5.44 \cdot 10^{-4}$
r_{A-20}, mol/m^2/s	-	-	-	-	$3.11 \cdot 10^{4}$
r_{A30}, mol/m^2/s	-	-	-	-	0.046
r_{C0}, mol/m^2/s	$5 \cdot 10^{-5}$	$5 \cdot 10^{-5}$	$5 \cdot 10^{-5}$	$5 \cdot 10^{-5}$	$1.1 \cdot 10^{-5}$
α_{A1}	0.5 (0.6)	0.5	0.5	0.5	0.5
α_{C}	0.5 (0.6)	0.5	0.5	0.5	0.5
g_{CO}	-	-	-	-	6.82
g_{OH}	-	-	-	-	0.43
β_{CO}	-	-	-	-	0.5
β_{OH}	-	-	-	-	0.5
$\theta^{ref}_{\mathrm{CO}x}$	-	0.5	0.5	0.5	-

Bibliography

[1] J.C. Amphlett, B.A. Peppley, E. Halliop, and A. Sadiq. The effect of anode flow characteristics and temperature on the performance of a direct methanol fuel cell. *J. Power Sources*, 96:204 – 213, 2001.

[2] P. Argyropoulos and K. Scott. A one dimensional model of a methanol fuel cell anode. *J. Power Sources*, 137(2):228–238, 2004.

[3] P. Argyropoulos, K. Scott, and W.M. Taama. Carbon dioxide evolution patterns in direct methanol fuel cells. *Electrochim. Acta*, 44:3575 – 3584, 1999.

[4] P. Argyropoulos, K. Scott, and W.M. Taama. Dynamic response of the direct methanol fuel cell under variable load conditions. *J. Power Sources*, 87:153–161, 2000.

[5] P. Argyropoulos, K. Scott, and W.M. Taama. The effect of operating conditions on the dynamic response of the direct methanol fuel cell. *Electrochim. Acta*, 45:1983–1998, 2000.

[6] P. Argyropoulos, W.M. Taama, and K. Scott. *Engineering & Modelling of Large Scale Liquid Fed Direct Methanol Fuel Cells Stacks*, volume No. 145 of *Symposium Series*. IChemE, 1999.

[7] A.S. Arico, P. Creti, V. Baglio, E. Modica, and V. Antonucci. Influence of flow design on the performance of a direct methanol fuel cell. *J. Power Sources*, 91:202–209, 2000.

[8] A.S. Arico, S. Srinivasan, and V. Antonucci. DMFCs: From fundamental aspects to technology development. *Fuel Cells*, 1(2):133 – 161, 2001.

[9] V.S. Bagotzky, Y.B. Vassiliev, and O. A. Khazova. Generalized scheme of chemisorption, electrooxidation and electroreduction of simple organic compounds on platinum group metals. *J. Electroanal. Chem.*, 81:229–238, 1977.

[10] M. Baldauf and W. Preidel. Experimental results on the direct electrochemical oxidation of methanol in PEM fuel cells. *J. Appl. Electrochem.*, 31:781–786, 2001.

[11] B.W. Bequette. *Process Dynamics: Process Modelling, Analysis, and Simulation.* Prentice Hall PTR, New Jersey, 1998.

[12] D.M. Bernardi and M.W. Verbrugge. Mathematical model of a gas-diffusion electrode bonded to a polymer electrolyte. *AIChE J.*, 37(8):1151–1163, 1991.

[13] M. Ceraolo, C. Miulli, and A. Pozio. Modelling static and dynamic behaviour of proton exchange membrane fuel cells on the basis of electro-chemical description. *J. Power Sources*, 113:131–144, 2003.

[14] M.V. Christov and S.N. Raicheva. Open-circuit reduction of oxygen coverage on Pt by organic substances. I. Mechanism and kinetics. *J. Electroanal. Chem.*, 73:43–54, 1976.

[15] L. Constantinou, R. Gani, and J.P. O'Connell. Estimation of the acentric factor and the liquid molar volume at 298 K using a new group contribution method. *Fluid Phase Equilibria*, 103:11 – 22, 1995.

[16] H.N. Dinh, X. Ren, F.H. Garzon, P. Zelenay, and S. Gottesfeld. Electrocatalysis in direct methanol fuel cells: In-situ probing of PtRu anode catalyst surfaces. *J. Electroanal. Chem.*, 491:222–233, 2000.

[17] J. Divisek, J. Fuhrmann, K. Gartner, and R. Jung. Performance modeling of a direct methanol fuel cell. *J. Electrochem. Soc.*, 150(6):A811–A825, 2003.

[18] S. Dutta, S. Shimpalee, and J.W. Van Zee. Three-dimensional numerical simulation of straight channel PEM fuel cells. *J. App. Electrochem.*, 30:135 – 146, 2000.

[19] K.A. Friedrich, K.P. Geyzers, U. Linke, U. Stimming, and J. Stumper. CO adsorption and oxidation on a Pt(111) electrode modified by ruthenium deposition: An IR spectroscopic study. *J. Electroanal. Chem.*, 402:123–128, 1996.

[20] H.A. Gasteiger, N. Markovic, P.N. Ross, and E.J. Cairns. Temperature-dependent methanol electro-oxidation on well-characterized Pt-Ru alloys. *J. Electrochem. Soc.*, 141(7):1795–1803, 1994.

[21] A.B. Geiger, E. Lehmann, P. Vontobel, and G.G. Scherer. Direct methanol fuel cell - in situ investigation of carbon dioxide patterns in anode flow fields by neutron radiography. PSI scientific report, V, 84-85, General Energy, Paul Scherrer Institut, Villigen, Switzerland, 1999.

[22] A.B. Geiger, T. Rager, G.G. Scherer, and A. Wokaun. Novel membranes for application in direct methanol fuel cells. PSI scientific report, 99-100, General Energy, Paul Scherrer Institut, Villigen, Switzerland, 2001.

[23] E. Gileadi. *Kinetics for Chemists, Chemical Engineers and Material Scientists*. Wiley VCH, New York, 1993.

[24] V. Gogel, T. Frey, Z. Yongsheng, K.A. Friedrich, L. Joerissen, and J. Garche. Performance and methanol permeation of direct methanol fuel cells: Dependence on operating conditions and on electrode structure. *J. Power Sources*, 127:172–180, 2004.

[25] S. Lj. Gojkovic, T. R. Vidakovic, and D. R. Djurovic. Kinetic study of methanol oxidation on carbon-supported PtRu electrocatalyst. *Electrochim. Acta*, 48:3607–3614, 2003.

[26] M. Gotz and H. Wendt. Binary and ternary anode catalyst formulations including the elements W, Sn and Mo for PEMFCs operated on methanol or reformate gas. *Electrochim. Acta*, 43(24):3637–3644, 1998.

[27] E. Gulzow, T. Kaz, R. Reissner, H. Sander, L. Schilling, and M.v. Bradke. Study of membrane electrode assemblies for direct methanol fuel cells. *J. Power Sources*, 105:261 – 266, 2002.

[28] B. Gurau, R. Viswanathan, R. Liu, T.J. Lafrenz, K.L. Ley, and E. S. Smotkin. Structural and electrochemical characterization of binary, ternary and quaternary platinum alloy catalysts for methanol electro-oxidation. *J. Phys. Chem. B*, 102:9997–10003, 1998.

[29] A. Hamnett. Mechanism of methanol electrooxidation. In A. Wieckowski, editor, *Interfacial electrochemistry, theory, experiment, and applications*, chapter 47. Marcel Decker Inc., New York, 1999.

[30] W. He and Q. Chen. Three-dimensional simulation of a molten carbonate fuel cell stack under transient conditions. *J. Power Sources*, 73:182 – 192, 1998.

[31] P. Heidebrecht and K. Sundmacher. Dynamic modeling and simulation of a countercurrent molten carbonate fuel cell (MCFC) with internal reforming. *Fuel Cells*, 2(3-4):166–180, 2002.

[32] S. Hikata, K. Yamane, and Y. Nakajima. Influence of cell pressure and amount of electrode catalyst in MEA on methanol crossover of direct methanol fuel cell. *JSAE Review*, 23:133 – 135, 2002.

[33] H. Hoster, T. Iwasita, H. Baumgartner, and W. Vielstich. Current time behaviour of smooth and porous PtRu surfaces for methanol oxidation. *J. Electrochem. Soc.*, 148:A496 – A501, 2001.

[34] T.H.M. Housmans and M.T.M. Koper. Methanol oxidation on stepped Pt [n(111) x (110)] electrodes: A chronoamperometric study. *J. Phys. Chem. B*, 107:8557–8567, 2003.

[35] T. Jarvi and E. Stuve. Fundamental aspects of vacuum and electrocatalytic reactions of methanol and formic acid on platinum surfaces. In J. Lipkowski and P. Ross, editors, *Electrocatalysis*, chapter 3. Wiley VCH, New York, 1998.

[36] L. Jorissen, V. Gogel, J. Kerres, and J. Garche. New membranes for direct methanol fuel cells. *J. Power Sources*, 105:267 – 273, 2002.

[37] Z. Jusys, J. Kaiser, and R.J. Behm. Composition and the activity of high surface area PtRu catalysts towards adsorbed CO and methanol electrooxidation. a DEMS study. *Electrochim. Acta*, 47:3693–3706, 2002.

[38] A. Kabbabi, R. Faure, R. Durand, B. Beden, F. Hahn, J.M. Leger, and C. Lamy. In situ FTIRS study of the electrocatalytic oxidation of carbon monoxide and methanol at Pt-Ru bulk alloy electrodes. *J. Electroanal. Chem.*, 444:41–53, 1998.

[39] J. Kallo, J. Kamara, W. Lehnert, and R. von Helmolt. Cell voltage transients of a gas-fed direct methanol fuel cell. *J. Power Sources*, 127:181–186, 2004.

[40] D. Kardash, C. Korzeniewski, and N. Markovic. Effects of thermal activation on the oxidation pathways of methanol at Pt-Ru alloy electrodes. *J. Electroanal. Chem.*, 500:518–523, 2001.

[41] P.S. Kauranen, E. Skou, and J. Munk. Kinetics of methanol oxidation on carbon supported Pt and Pt-Ru catalysts. *J. Electroanal. Chem.*, 404:1–13, 1996.

[42] U. Krewer, Y. Song, V. John, R. Luebke, G. Matthies, K. Sundmacher, and L. Tobiska. Direct methanol fuel cell (DMFC): Analysis of residence time behaviour of anodic flow bed. *Chem. Eng. Sci.*, 59:119–130, 2004.

[43] C. Laquerbe, J.C. Laborde, P. Floquet, L. Pibouleau, and S. Domenech. Identification of parametric models based on RTD theory. application to safety studies in ventilated nuclear enclosures. *Computers chem. Engng.*, 22:5347–5353, 1998. Suppl.

[44] I. Lavric, P. Staiti, P. Novak, and S. Hocevar. Computational fluid dynamics study of phosphotungstic acid electrolyte-based fuel cell (PWAFC). *J. Power Sources*, 96:303 – 320, 2001.

[45] J.M. Leger. Mechanistic aspects of methanol oxidation on Pt-based electrocatalysts. *J. Appl. Electrochem.*, 31:767–771, 2001.

[46] A. Lima, C. Coutanceau, J.M. Leger, and C. Lamy. Investigation of ternary catalysts for methanol electrooxidation. *J. Appl. Electrochem.*, 31:379–386, 2001.

[47] W.F. Lin, M.S. Zei, M. Eiswirth, G. Ertl, T. Iwasita, and W. Vielstich. Electrocatalytic activity of Ru-modified Pt(111) electrodes toward CO oxidation. *J. Phys. Chem. B*, 103:6968–6977, 1999.

[48] J.P. Meyers and J. Newman. Simulation of the direct methanol fuel cell - II. Modeling and data analysis of transport and kinetic phenomena. *J. Electrochem. Soc.*, 149(6):A718–A728, 2002.

[49] A. Mitterdorfer and L.J. Gauckler. Identification of the reaction mechanism of the Pt, O-2(g)vertical bar yttria-stabilized zirconia system - Part I: General framework, modelling, and structural investigation. *Solid State Ionics*, 117(3-4):187–202, 1999.

[50] A.G.O. Mutambara. *Design and Analysis of Control Systems*. CRC Press, Boca Raton, 1999.

[51] J. Nordlund and G. Lindbergh. A model for the porous direct methanol fuel cells anode. *J. Electrochem. Soc.*, 149(9):A1107–A1113, 2002.

[52] J. Nordlund, A. Roessler, and G. Lindbergh. The influence of electrode morphology on the performance of a DMFC anode. *J. Appl. Electrochem.*, 32:259 – 265, 2002.

[53] V. Panic, T. Vidakovic, S. Gojkovic, A. Dekanski, S. Milonjic, and B. Nikolic. The properties of carbon-supported hydrous ruthenium oxide obtained from RuO_xH_y sol. *Electrochim. Acta*, 48:3805–3813, 2003.

[54] R.C. Reid, J.M. Prausnitz, and B.E. Polling. *The Properties of Gases and Liquids*. McGraw-Hill, New York, 4 th edition, 1987.

[55] R. Schloegl. Membrane permeation in systems far from equilibrium. *Berichte der Bunsengesellschaft fuer Physikalische Chemie*, 70:400–414, 1966.

[56] T. Schultz. Experimental and model-based analysis of the dynamic operating behaviour of the direct methanol fuel cell (DMFC). In *Proceedings of the 7th European Symposium on Electrochemical Engineering*, Toulouse, France, Oct. 2005.

[57] T. Schultz. *Experimental and model-based analysis of the steady-state and dynamic operating behaviour of the direct methanol fuel cell (DMFC).* PhD thesis, University of Magdeburg, Germany, 2005.

[58] T. Schultz and K.Sundmacher. Rigorous dynamic model of a direct methanol fuel cell based on Maxwell-Stefan mass transport equations and a Flory-Huggins activity model: Formulation and experimental validation. *J. Power Sources*, 2005. , in press.

[59] K. Scott, P. Argyropoulos, P. Yiannopoulos, and W.M. Taama. Electrochemical and gas evolution characteristics of direct methanol fuel cells with stainless steel mesh flow beds. *J. Appl. Electrochem.*, 31:823 – 832, 2001.

[60] K. Scott, W.M. Taama, and P. Argyropoulos. Material aspects of the liquid feed direct methanol fuel cell. *J. Appl. Electrochem.*, 28:1389 – 1397, 1998.

[61] K. Scott, W.M. Taama, and P. Argyropoulos. Engineering aspects of the direct methanol fuel cell system. *J. Power Sources*, 79:43 – 59, 1999.

[62] K. Scott, W.M. Taama, P. Argyropoulos, and K. Sundmacher. The impact of mass transport and methanol crossover on the direct methanol fuel cell. *J. Power Sources*, 83:204 – 216, 1999.

[63] K. Scott, W.M. Taama, S. Kramer, P. Argyropoulos, and K. Sundmacher. Limiting current behaviour of the direct methanol fuel cell. *Electrochim. Acta*, 45:945 – 957, 1999.

[64] A.K. Shukla, C.L. Jackson, K. Scott, and R.K. Raman. An improved-performance liquid-feed solid-polymer-electrolyte direct methanol fuel cell operating at near-ambient conditions. *Electrochim. Acta*, 47:3401 – 3407, 2002.

[65] M.A. Siddiqi and K. Lucas. Correlations for prediction of diffusion in liquids. *Can. J. Chem. Eng.*, 64(5):839 – 843, 1986.

[66] A. Siebke, W. Schnurnberger, F. Meier, and G. Eigenberger. Investigation of the limiting processes of a DMFC by mathematical modeling. *Fuel Cells*, 3(1-2):37–47, 2003.

[67] A. Simoglou, P. Argyropoulos, E.B. Martin, K. Scott, A.J. Morris, and W.M. Taama. Dynamic modelling of the voltage response of direct methanol fuel cells and stacks. Part I: Model development and validation. *Chem. Eng. Sci.*, 56:6761–6772, 2001.

[68] K. Sundmacher, T. Schultz, S. Zhou, K. Scott, M. Ginkel, and E.D. Gilles. Dynamics of the direct methanol fuel cell (DMFC): Experiments and model-based analysis. *Chem. Eng. Sci.*, 56:333 – 341, 2001.

[69] K. Sundmacher and K. Scott. Direct methanol polymer electrolyte fuel cell: Analysis of charge and mass transfer in the vapour-liquid-solid system. *Chem. Eng. Sci.*, 54:2927 – 2936, 1999.

[70] T. Vidakovic. *Kinetics of Methanol Electrooxidation on PtRu Catalysts in a Membrane Electrode Assembly.* PhD thesis, University of Magdeburg, Germany, 2005.

[71] T. Vidakovic, M. Christov, and K. Sundmacher. Rate expression for electrochemical oxidation of methanol on a direct methanol fuel cell anode. *J. Electroanal. Chem.*, 580:105–121, 2005.

[72] H. Wang, C. Wingender, H. Baltruschat, M. Lopez, and M. T. Reetz. Methanol oxidation on Pt, PtRu, and colloidal Pt electrocatalysts: A DEMS study of product formation. *J. Electroanal. Chem.*, 509:163–169, 2001.

[73] Z. Wei, S. Wang, B. Yi, J. Liu, L. Chen, W. Zhou, W. Li, and Q. Xin. Influence of electrode structure on the performance of a direct methanol fuel cell. *J. Power Sources*, 106:364 – 369, 2002.

[74] G.J. Wells and W.H. Ray. Investigation of imperfect mixing effects in the LDPE autoclave reactor using CFD and compartment models. In *Proceedings of the 7th DECHEMA Workshop on Polymer Reaction Engineering. DECHEMA Monographs*, volume 137, pages 49–59. Wiley VCH, 2001.

[75] T. Wik. *On modelling the dynamics of fixed biofilm reactors.* PhD thesis, Chalmers University of Technology, Goeteborg, Sweden, 1999.

[76] X.H. Xia, T. Iwasita, F. Ge, and W. Vielstich. Structural effects and reactivity in methanol oxidation on polycrystalline and single crystal Pt. *Electrochim. Acta*, 41(5):711–718, 1996.

[77] S. Yerramalla, A. Davari, A. Feliachi, and T. Biswas. Modeling and simulation of the dynamic behavior of a polymer electrolyte fuel cell. *J. Power Sources*, 124:104–113, 2003.

[78] S. Zhou, T. Schultz, M. Peglow, and K. Sundmacher. Analysis of the nonlinear dynamics of a direct methanol fuel cell. *Phys. Chem. Chem. Phys.*, 3:347 – 355, 2001.